A phase field crystal study of grain growth in one and two dimensions

by

Øydis Larsen

Thesis

for the degree of

Master of Science

Faculty of Mathematics and Natural Sciences
University of Oslo

June 2014

Acknowledgements

I would like to thank my fellow students at Computational Physics for their friendship, helpful conversations and excellent working environment. I would especially like to thank Mathilde, Emilie and Jonas at room 309 for the community we have shared, especially over the past year, both at university and outside. I would like to thank my family for the support they have given me all my life. And I would especially like to thank my supervisor, Luiza Angheluta. Your helpful guidance and moral support over the past year is greatly appreciated.

Contents

Chapter 1

Introduction

Our purpose in this thesis is to study the evolution of nonequilibrium crystalline materials. An out-of-equilibrium system is a system that is, to some degree, disordered. Typically, the disordered state will try to reach an equilibrium state, in order to minimize the free energy of the system. The equilibrium state of a crystal is a perfectly ordered state. An example of a perfect hexagonal crystal in two dimensions can be seen in Figure 1.1. The evolution from a disordered state towards the ordered state of the equilibrium crystal is called the coarsening process [1].

During the coarsening process, a network of domains with different crystal symmetries is formed. This is referred to as a polycrystalline material, and the domains can also be referred to as grains. Between the domains grain boundaries appear, consisting of crystal dislocations. Examples of polycrystalline materials can be seen in Figure 3.2. The final state of the coarsening process is the equilibrium crystal. However, a system can often reach a metastable state before this happens. This is called grain growth stagnation [2, 3, 4].

In this thesis grain growth in one and two dimensions have been studied by using the phase field crystal (PFC) model [5, 6, 7]. The 1D case is useful to study because it is simpler to study theoretically. However, the solutions have little physical meaning, beyond extrapolating them to higher dimensions. In 2D the dynamics are more complicated than in the 1D case. Crystal dislocations appear, and their evolution can be tracked. The equilibrium crystal is a hexagonal structure, as seen in Figure 1.1. In 2D the results can be compared to crystal growth in thin films.

In Chapter 2, where we study grain growth dynamics in 1D, we briefly examine phase transformations and the solid-liquid coexistence state in the PFC model. However, the main part of the chapter is the marginal stability analysis [8, 9] on the PFC equation in 1D. The marginal stability analysis is performed on a solidification process, where a solid front is propagating into a homogeneous liquid. We test the predictions made for the front velocity and the wavenumber of the solid forming behind the front. We study two different versions of the

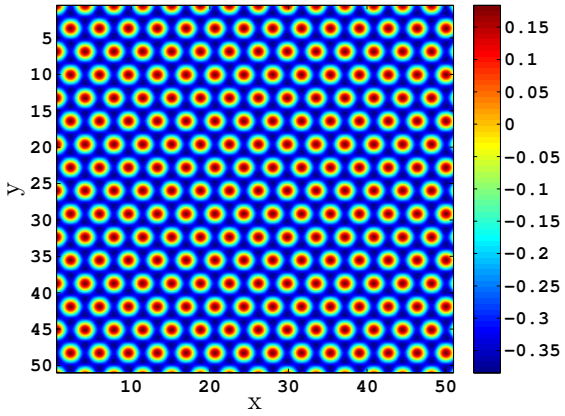

Figure 1.1: A perfect crystal in 2D with a hexagonal structure, obtained from the PFC model. The color shows the value of the order parameter ψ and the peaks represent atoms. In this case the undercooling parameter is $\epsilon = 0.1$ and the mean order parameter is $\psi_0 = -0.195$. The system size is 1000×1000 with grid size $\Delta x = 0.1$. This crystal is not obtained through simulations, but the theoretical approximation detailed in Chapter 3.

PFC equation, the standard equation and the hyperbolic equation [9]. Our results are in agreement with the predictions for the front velocity but not for the wavenumber, at least not for the hyperbolic equation. We discuss possible causes of this.

In the rest of the thesis we study grain growth dynamics in 2D. The system we study is a two-grain system. We perform simulations for different temperatures and misorientation angles between the grains, and compare the results to the theory derived by Cahn and Taylor [10]. We find what appears to be grain growth stagnation for the colder systems. However, there are strong indications that this could be an effect of the PFC model itself, and not the system. We have been unable to test this assumption.

1.1 The phase field crystal model

The phase field crystal (PFC) model that has been described by Elder et al. [5, 6, 7] is very useful in studying the evolution of polycrystalline materials because it operates on atomic length scales and diffusive time scales. This makes it possible to simulate the long-term behavior of a nanocrystalline system. The model can also be used to simulate systems subjected to elastic tension and stress. We can use the PFC model in order to study the properties of a crystalline system. We can learn how crystals grow, and how they react to stress, temperature etc.

The PFC model simulates a system that is suddenly quenched below the

melting point, resulting in crystallization. The model is formulated as a partial differential equation that can not be solved analytically, only numerically. The partial differential equation is defined as follows,

$$\frac{\partial \psi}{\partial t} = \nabla^2 \frac{\delta \mathcal{F}}{\delta \psi} \tag{1.1}$$

with the free energy functional $\mathcal{F}$ defined as,

$$\mathcal{F} = \int dr \left\{ \psi \left[-\epsilon + (1 + \nabla^2)^2 \right] \frac{\psi}{2} + \frac{\psi^4}{4} \right\} \tag{1.2}$$

In the above equation $\epsilon \sim (T_c - T)/T_c$ is the dimensionless undercooling parameter that determines how deep below the melting point the system is quenched. T is the temperature of the system and T_c is the melting temperature. The order parameter ψ is a dimensionless unit that can be interpreted as the atomic density or the probability of finding an atom in a given position, even though it can take negative values. Atoms are found at either the highest or lowest values of ψ, depending on the sign of the mean order parameter ψ_0 the system was initialized with. Because of this definition of atoms, the number of atoms are not conserved.

The PFC model is a phenomenological model, so the free energy functional above has been chosen because it is at a minimum when the order parameter ψ forms a periodic structure. However, a derivation of the PFC equation from the density functional theory has also been performed [7, 11]. We will summarize this derivation in Section 1.4.

1.2 Different versions of the PFC model

The PFC model described in Section 1.1 is the standard PFC equation. However, the PFC model can be modified in order to better capture the behavior of a given system. One method of modifying the PFC equation is to choose a different free energy functional $\mathcal{F}$. It might be possible to derive a more accurate formulation of the free energy. Changing $\mathcal{F}$ might also allow for different crystal structures, which could be useful as not all crystals have a hexagonal structure. And most crystals do not consist of only one type of atom, but the crystal simulated by the standard PFC equation does. Elder et al. [7] derive a PFC model for a binary alloy, which makes it possible to simulate more complicated systems.

Another modified version of the PFC equation is called the hyperbolic PFC equation [9]. It includes a second order time derivative $\partial^2\psi/\partial t^2$ in the standard PFC equation in eq. 1.1. The standard PFC equation can also be called the parabolic PFC equation. The hyperbolic PFC equation is intended to capture dynamics on smaller time scales than the parabolic PFC equation.

The PFC model can also be formulated as an amplitude equation [12], and this allows for larger time scales and a length scale closer to the continuum

scale. The complex amplitudes describing the system contain information about deformations and crystal orientations in the system, and what state the system is in.

An attempt at modeling the elastic dynamics of the system more correctly was recently made by Heinonen et al. [12]. The authors argue that the standard PFC model does not give a correct result of the elastic excitations in the system, because the diffusive dynamics of the ψ-field are on a much slower time scale than the elastic dynamics. Therefore, the elastic excitations are often equilibrated too slowly to be physically correct, and they show that this can also affect the evolution of the ψ-field. They propose to separate the time scales by including a second step in the calculations. After every new timestep has been calculated, the elastic excitations are equilibrated, ensuring mechanical equilibrium at all times. This paper is further examined in Section 3.3.

In this thesis we perform simulations using both the parabolic and the hyperbolic PFC equation. The method ensuring mechanical equilibrium has not been implemented in the thesis, but possible ramifications of the suggested shortcomings in the standard PFC model will be further discussed.

1.3 Comparison to molecular dynamics

Molecular dynamics (MD) simulations use the interatomic forces to model the atoms in a system. For every timestep the velocity and position of every single atom is known. As mentioned in Section 1.1, PFC simulations do not model individual atoms. Instead they model the field of an order parameter ψ. The peaks of the order parameter can be interpreted as atoms, but the number of atoms is not conserved. This makes it difficult to model structures on an atomic level quantitatively. The main advantage of the PFC model over the MD model is that it can be used on larger time scales. In addition to this, the accuracy of the MD simulations depends on the accuracy of the definition of the interatomic forces that are used in the simulations.

Chan et al. [13] suggest a mechanism to study MD dynamics with the PFC equation. The order parameter ψ becomes a physical density ρ by setting the constraint that ρ can not have negative values. The authors want to permit vacancies where the atomic density is $\rho = 0$. By including a penalty term in the free energy functional, ρ is forbidden from having negative values. By using a one-mode approximation to the solution of ρ, the parameter values that give stable solutions are found. These solutions also allow vacancies. The value of the mean density ρ_0 when the system is initialized determines the number of atoms in the system.

This method has not been implemented in this thesis, but it illustrates some of the similarities and differences between the PFC model and MD simulations.

1.4 The PFC model derived from density functional theory

The phase field crystal model was developed as a phenomenological model, but it has been shown [7, 11] that it can be connected to the classical density functional theory (DFT). DFT is, like the PFC model, based on a free energy functional $\mathcal{F}[\rho(\mathbf{r},t)]$, but in this theory $\mathcal{F}$ can be derived from microscopic equations of motion. Where the free energy of the PFC model is a functional of the dimensionless order parameter ψ, the free energy in DFT is a functional of the atomic density ρ. The dynamical DFT equation (DDFT) includes a time derivative in the equation, and is formulated as follows for colloidal spheres placed in a solvent [11],

$$\frac{\partial \rho(\mathbf{r},t)}{\partial t} = \gamma^{-1}\nabla\cdot\left[\rho(\mathbf{r},t)\nabla\frac{\delta\mathcal{F}[\rho(\mathbf{r},t)]}{\delta\rho(\mathbf{r},t)}\right] \tag{1.3}$$

The parameter $\gamma = 3\pi\eta_0 d$ is the friction coefficient of a colloidal sphere, d is the diameter of the sphere and η_0 is the viscosity of the fluid the colloidal sphere is placed in.

Teeffelen et al. [11] derive the DDFT equation from a set of spherical, colloidal particles in a solvent, which can be described by the Langevin equations of motion,

$$\frac{\partial \mathbf{r}_i}{\partial t} = \gamma^{-1}(\mathbf{F}_i + \mathbf{f}_i), \qquad i = 1,\ldots,N \tag{1.4}$$

where $\mathbf{F}_i$ is the deterministic force acting on particle i, and $\mathbf{f}_i$ are the Gaussian random forces acting on the particle from the solvent. This equation is valid when one assumes that there are no hydrodynamic forces acting on the particles. The dynamics of the colloidal particles can be described as overdamped Brownian motion.

In order to determine the probability of finding a particle at a given position $\mathbf{r}$ and a given time t, instead of determining the position of every particle, the one-particle density $\rho(\mathbf{r},t)$ and two-particle density $\rho^{(2)}(\mathbf{r},\mathbf{r}',t)$ are introduced,

$$\rho(\mathbf{r},t) = \sum_i \langle\delta[\mathbf{r}-\mathbf{r}_i(t)]\rangle \tag{1.5}$$

$$\rho^{(2)}(\mathbf{r},\mathbf{r}',t) = \sum_{i,j;i\neq j} \langle\delta[\mathbf{r}-\mathbf{r}_i(t)]\delta[\mathbf{r}-\mathbf{r}_j(t)]\rangle \tag{1.6}$$

These expressions are used in the following equation, which can be derived from the Langevin equations,

$$\begin{aligned}\frac{\partial \rho(\mathbf{r},t)}{\partial t} = \gamma^{-1}\nabla\Big[&k_B T\nabla\rho(\mathbf{r},t) + \rho(\mathbf{r},t)\nabla V(\mathbf{r},t) \\ &+ \int d\mathbf{r}'\rho^{(2)}(\mathbf{r},\mathbf{r}',t)\nabla u(|\mathbf{r}-\mathbf{r}'|)\Big]\end{aligned} \tag{1.7}$$

where $u(|\mathbf{r}-\mathbf{r}'|)$ are pairwise additive potentials and k_BT is the thermal energy. In the following, the two-particle density $\rho^{(2)}(\mathbf{r},\mathbf{r}',t)$ is approximated by an equilibrium correlation function. This approximation of a time-dependent nonequilibrium function with an equilibium function is called an adiabatic approximation.

The above equation receives contributions from different sources. The functional $\mathcal{F}[\rho(\mathbf{r})]$ is made up of the ideal-gas free energy functional $\mathcal{F}_{\mathrm{id}}[\rho(\mathbf{r})]$, the external free energy functional $\mathcal{F}_{\mathrm{ext}}[\rho(\mathbf{r})]$ and the excess free energy functional $\mathcal{F}_{\mathrm{ex}}[\rho(\mathbf{r})]$. The free energy functional is minimized by the equilibrium density $\rho_0(\mathbf{r})$ if $\mathcal{F}$ is known exactly. It then becomes the Helmholtz free energy $\mathcal{F} \equiv \mathcal{F}[\rho_0(\mathbf{r})]$. The ideal free energy functional can be expressed as follows,

$$\mathcal{F}_{\mathrm{id}}[\rho(\mathbf{r})] = k_BT \int d\mathbf{r}\rho(\mathbf{r})\{\ln[\rho(\mathbf{r})\Lambda^d] - 1\} \tag{1.8}$$

where Λ is the de Broglie wavelength and d is the spatial dimension. The ideal free energy corresponds to the diffusion term $k_BT\nabla\rho(\mathbf{r},t)$ in eq. 1.7. The external free energy functional is,

$$\mathcal{F}_{\mathrm{ext}}[\rho(\mathbf{r})] = \int d\mathbf{r}\rho(\mathbf{r})V(\mathbf{r},t) \tag{1.9}$$

The functional derivative of the excess free energy with respect to density can be approximated by the expression,

$$\frac{\delta\mathcal{F}_{\mathrm{ex}}[\rho_0(\mathbf{r})]}{\delta\rho(\mathbf{r})} = -k_BTc_0^{(1)}(\mathbf{r}) \tag{1.10}$$

where $k_BTc_0^{(1)}(\mathbf{r})$ is the effective one-body potential. Together, these expressions make up the free energy functional in the DDFT model.

A further approximation of the excess free energy can be made by making an expansion of the density difference $\Delta\rho = \rho(\mathbf{r}) - \rho$ around a reference fluid, where ρ is the average density,

$$\mathcal{F}_{\mathrm{ex}}[\rho(\mathbf{r})] \approx \mathcal{F}_{\mathrm{ex}}(\rho) - \frac{k_BT}{2}\iint d\mathbf{r}d\mathbf{r}'\Delta\rho(\mathbf{r})\Delta\rho(\mathbf{r}') \times c_0^{(2)}(\mathbf{r}-\mathbf{r}';\rho) \tag{1.11}$$

where $\mathcal{F}_{\mathrm{ex}}(\rho)$ is the excess free energy of the reference fluid and $c_0^{(2)}(\mathbf{r}-\mathbf{r}';\rho)$ is the two-point direct correlation function of the reference fluid.

In order to derive the PFC model three further approximations must be made. The expression for the excess free energy $\mathcal{F}_{\mathrm{ex}}[\rho(\mathbf{r})]$ is approximated by a local gradient expansion of the correlation function. The gradient expansion $c_0^{(2)}(\mathbf{r}-\mathbf{r}';\rho) = \hat{C}_0 - \hat{C}_2\nabla^2 + \hat{C}_4\nabla^4 + \cdots$, can also be seen as a Taylor expansion of the Fourier transform of the correlation function $\hat{c}_0^{(2)}(\mathbf{k};\rho)$. The mobility in the DDFT equation in eq. 1.3 is approximated by a constant $\gamma^{-1}\rho(\mathbf{r}) \approx \gamma^{-1}\rho$, where

ρ is the average density. And the logarithm in the ideal free energy $\mathcal{F}_{\text{id}}[\rho(\mathbf{r})]$ is approximated by a Taylor series. The order parameter ψ in the PFC equation has to be understood as the dimensionless density difference $\psi(\mathbf{r},t) = (\rho(\mathbf{r},t) - \rho)/\rho$. The approximation to the ideal free energy functional is,

$$\mathcal{F}_{\text{id}}[\rho(\mathbf{r})] \approx k_B T \rho \int d\mathbf{r} \left\{ \frac{1}{2}\psi(\mathbf{r},t)^2 - \frac{1}{6}\psi(\mathbf{r},t)^3 + \frac{1}{12}\psi(\mathbf{r},t)^4 - \text{const.} \right\} \tag{1.12}$$

All of these approximations result in the PFC equation

$$\begin{aligned} \frac{\partial \psi(\mathbf{r},t)}{\partial t} =& D\rho\nabla^2 \Bigg[\psi(\mathbf{r},t) - \frac{1}{2}\psi(\mathbf{r},t)^2 + \frac{1}{3}\psi(\mathbf{r},t)^3 + \frac{1}{k_B T} V(\mathbf{r},t) \\ & - \rho(\hat{C}_0 - \hat{C}_2\nabla^2 + \hat{C}_4\nabla^4)\psi(\mathbf{r},t) \Bigg] \end{aligned} \tag{1.13}$$

where the diffusion constant is $D = k_B T/\gamma$. The constants $\hat{C}_0$, $\hat{C}_2$ and $\hat{C}_4$ need to be parametrized. This can be done with the one-mode approximation introduced by Elder et al. [6].

Equation 1.13 looks slightly different from the standard PFC equation in eq. 1.1 and 1.2. The constants are different, but there are also some additional terms in eq. 1.13. There is no external potential V in the standard PFC equation, so the term $(k_B T)^{-1} V(\mathbf{r},t)$ is not included in eq. 1.2. The term $\frac{1}{2}\psi(\mathbf{r},t)^2$ has also disappeared in our version of the PFC equation, though the term is sometimes included [4]. The quenching rate ϵ is not included in the above equation, but it is incorporated in the choice of constants $\hat{C}_0$, $\hat{C}_2$ and $\hat{C}_4$.

Teeffelen et al. [11] also compare results from simulations of the DDFT equation and the PFC equation. They find that the solutions can only be compared by rescaling the free energy of the PFC equation. With this rescaling, the velocity of a propagating front is found to be approximately the same with the two methods. However, the crystalline peaks of the density field $\rho(\mathbf{r},t)$ and the order parameter field $\psi(\mathbf{r},t)$ look very different. They therefore conclude that PFC models can give good qualitative, but not quantitative results.

In summary, there are several approximations that have to be made in order to obtain the DDFT and PFC equations. The initial assumption about the modeled system is that there are no hydrodynamic interactions between the particles. In order to get the DDFT equation, first the adiabatic approximation has to be made, where the two-particle density is approximated by an equilibrium correlation function. This affects the excess free energy contribution. Then a further approximation of the excess free energy functional is made when the density is expanded around a reference fluid density. In order to obtain the PFC equation, three new approximations are made: a gradient expansion is performed on the correlation function in the excess free energy functional, the mobility is assumed to be constant, and the logarithm in the ideal free energy functional is approximated by a Taylor expansion.

Chapter 2

The PFC equation in 1D

In one spatial dimension, the crystal structure is interpreted as a periodic function, or a wave. The only dislocation that can appear in one dimension is the interface between a liquid and a solid phase. In Section 2.1 we will take a closer look at this interface, and the growing and melting of a crystal.

2.1 The parabolic phase field crystal model in one dimension

The phase field crystal model [5, 6, 7] can, in its simplest form, be expressed by the dimensionless differential equation

$$\frac{\partial \psi}{\partial t} = \nabla^2 \frac{\delta \mathcal{F}}{\delta \psi} \tag{2.1}$$

where ψ is the order parameter, which can be interpreted as the atomic density, or the probability of finding an atom in a particular position. $\mathcal{F}$ is the free energy functional, and it can be written like this:

$$\mathcal{F} = \int dr \left\{ \psi \left[-\epsilon + (1 + \nabla^2)^2 \right] \frac{\psi}{2} + \frac{\psi^4}{4} \right\} \tag{2.2}$$

This is the parabolic PFC equation, which will be the focus of this section. The parabolic equation is the one which is most widely used. In Section 2.2 the hyperbolic PFC equation [9] will be further examined. The hyperbolic equation includes a second order time derivative, and can therefore give better results for fast dynamics.

When the free energy is defined like this, the equilibrium wavenumber k has been set equal to 1 in one dimension. The constant $\epsilon \sim (T_c - T)/T_c$ tells us how deep the quench is. T_c is the temperature for which phase transition occurs (the melting temperature), and T is the temperature of the system. When the free

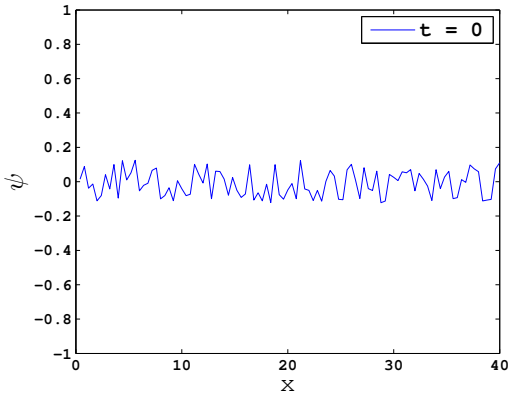

Figure 2.1: Initial configuration of the order parameter ψ, with random values around $\psi_0 = 0$. The units are dimensionless.

energy is defined like this, and T is below the melting temperature, ϵ is a positive value.

The free energy wants to be minimized, which happens when the atoms have a periodic structure. This makes it possible to model the solid phase as a crystal structure. Taking the functional derivative of the free energy gives us the PFC model as this differential equation:

$$\frac{\partial \psi}{\partial t} = \nabla^2 \left[-\epsilon\psi + (1 + \nabla^2)^2 \psi + \psi^3 \right] \tag{2.3}$$

In order to solve the above differential equation in one dimension, the explicit forward Euler scheme detailed in the Appendix was implemented. Because the simple Euler method is so straightforward, the timestep had to be very small in order to get good results. With $\Delta x = 0.4$, Δt had to be set to $\Delta t = 1 \cdot 10^{-4}$. These were the settings that were used in most of the following simulations in this section. In the figures the x-axis is Δx multiplied by the number of grid cells in the x-direction. The t in the figure legends is Δt multiplied by the number of timesteps. Both x and t are dimensionless. In all the simulations the boundary conditions were chosen to be periodic.

In the first simulations, the order parameter ψ was initialized with small random fluctuations around zero, as in a homogeneously ordered liquid. In other words, the mean value of the order parameter was $\psi_0 = 0$. In Figure 2.1 this initial configuration can be seen. When the PFC simulation begins, the homogeneous liquid experiences a sudden drop in temperature, or a quench. This system is called an undercooled liquid. The undercooling ϵ was at first set to 0.4, and the system evolved to an ordered, periodic phase, as can be seen in Figure 2.2. The figure shows the system at two different timesteps in the evolution towards a periodic phase.

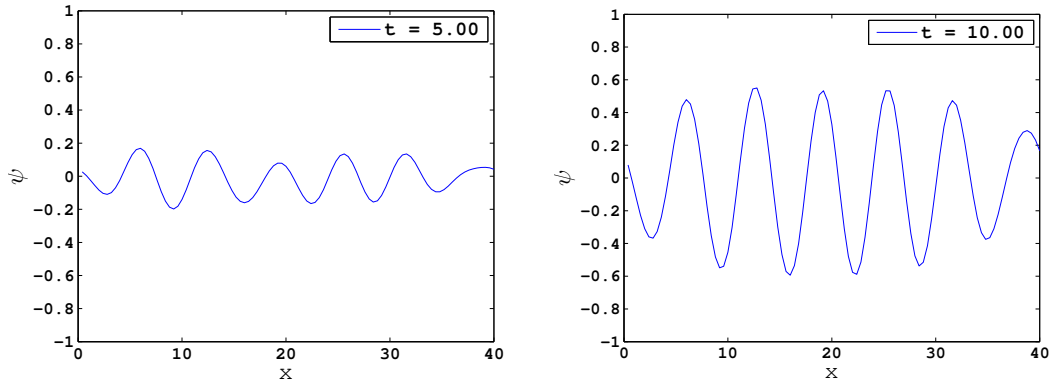

Figure 2.2: A periodic phase is developing from the initial configuration in Figure 2.1. The images are from two different timesteps. In this simulation $\epsilon = 0.4$ and $\psi_0 = 0$. The units are dimensionless.

In Figure 2.3, the ordered phase for different values of ϵ have been attempted fitted with solutions on the form $\psi = A\sin(kx) + \psi_0$. This is the one-mode approximation of ψ for the 1D case, suggested by Elder and Grant [6]. In order to increase the resolution of the results, $\Delta x = 0.3$ for these particular simulations. The timestep then had to be changed to $\Delta t = 2 \cdot 10^{-5}$ in order to get a stable result. In all three simulations $\psi_0 = 0$. In these experiments, with $\Delta x = 0.3$, there were approximately 20 grid cells per wavelength. One wavelength in the crystal can be interpreted as one atom. In most of the other experiments, with $\Delta x = 0.4$, there were about 15 grid cells per atom.

In Figure 2.4 the sine functions from Figure 2.3 have been plotted together. The wavenumber was found to be $k \approx 1.05$ in all three simulations. We expected the wavenumber to be around 1, as that is how the PFC equation in eq. 2.3 is defined. The amplitude A, however, does change with ϵ. A can be seen to increase as ϵ increases.

Elder and Grant [6] found an expression for the amplitude in the 1D case:

$$A^2 = -4\left(\frac{\hat{\omega}_{k^*}}{3} + \psi_0^2\right) \tag{2.4}$$

where $\hat{\omega}_k = -\epsilon + (1 - k^2)^2$. Because the equilibrium wavenumber was set to $k^* = 1$, the expression for $\hat{\omega}_{k^*}$ simplifies to $\hat{\omega}_{k^*} = -\epsilon$. If we also take the square root on both sides of the equation we get the amplitude,

$$A = 2\sqrt{\frac{\epsilon}{3} - \psi_0^2} \tag{2.5}$$

In Figure 2.4b the results of simulations with different values of ϵ can be seen with the analytical curve. We performed some more simulations than the ones that

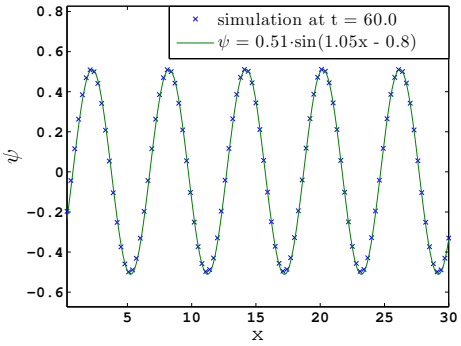

(a) Results for $\epsilon = 0.2$.

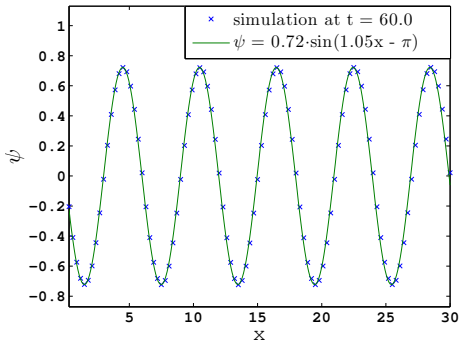

(b) Results for $\epsilon = 0.4$.

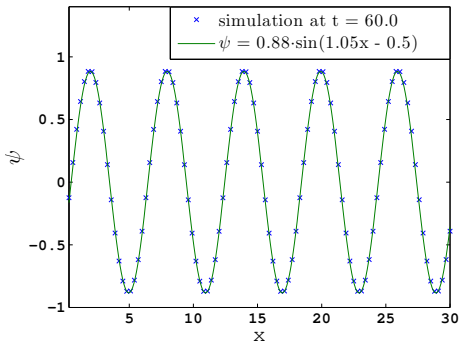

(c) Results for $\epsilon = 0.6$.

Figure 2.3: The periodic results of ψ for different values of ϵ with fitted sine functions. $\psi_0 = 0$ in all three examples. The different phases in the sine functions were only introduced for a better visualization of the comparison. The units are dimensionless.

are plotted in Figure 2.4a, and included them in this plot. In all the simulations $\psi_0 = 0$.

Using the one-mode approximation, a phase diagram was calculated by Elder and Grant [6]. The phase diagram can be seen in Figure 2.5. The diagram shows what values of the parameters ψ_0 and ϵ result in the different phases. In other words, the mean order parameter of the system and the depth of the quench determine the phase. Depending on what values these parameters are given, the simulation can result in a constant, periodic or coexistence phase. The constant phase is a homogeneous liquid phase, and the periodic phase is the crystal structure of the solid phase. In the coexistence phase, a periodic phase should be able to be placed next to a constant phase without either "absorbing" the other.

All the simulations performed above were in the solid phase. In the phase diagram in Figure 2.5 we see that $\psi_0 = 0$ places the simulation in the solid phase as long as $\epsilon > 0$. This is the case for all the simulations above.

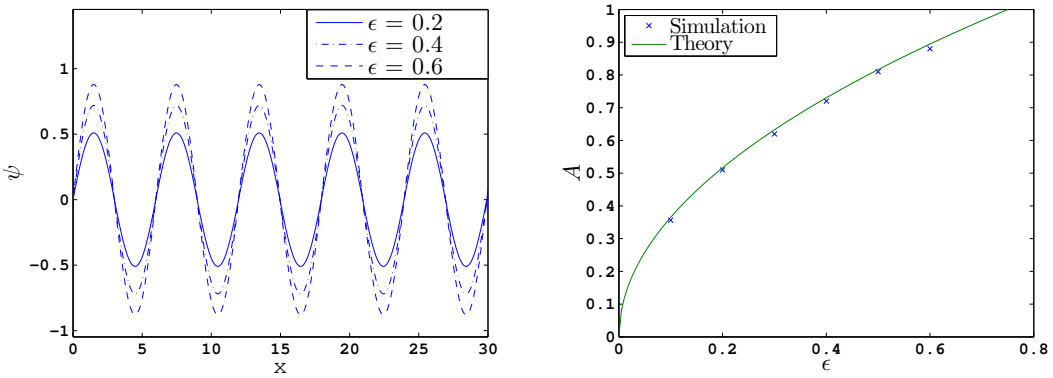

(a) Sine functions for different ϵ. **(b)** The amplitude of ψ.

Figure 2.4: (a) The sine functions that were fitted to results from simulations with different ϵ in Figure 2.3, all plotted in one figure. The difference in amplitude is easier to see in this figure. The frequency was approximately the same for all three simulations. In (b) the amplitude from the simulations in (a) and from some additional simulations are plotted with the theoretical prediction in eq. 2.5.

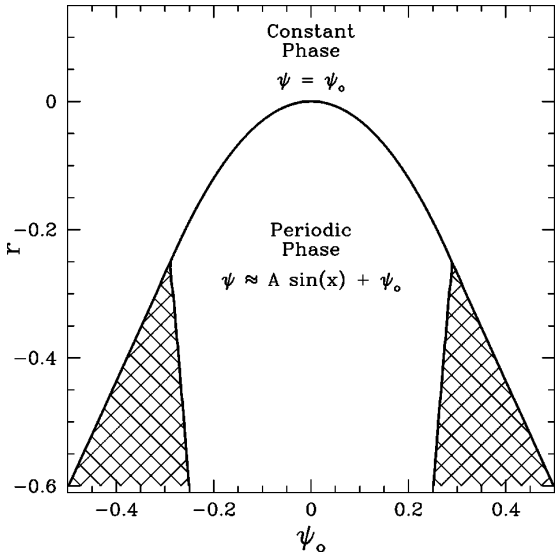

Figure 2.5: Phase diagram for the one-dimensional PFC equation, calculated by Elder and Grant [6], p. 5. The diagram shows that the choice of parameters ϵ and ψ_0 determine the phase. On the y-axis $r = -\epsilon$. The melting point is at $\epsilon = 0$. The x-axis shows the mean order parameter ψ_0. The constant phase is the liquid phase, and the periodic phase is the solid, crystalline phase. The hatched regions show the coexistence phase.

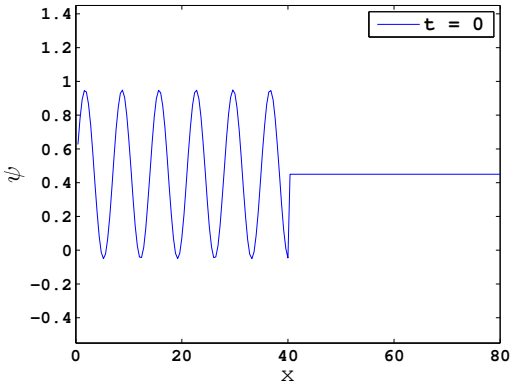

Figure 2.6: A crystal placed next to a liquid, with $\psi_0 = 0.45$ for both phases. The crystal was intialized with $\epsilon = 0.2$.

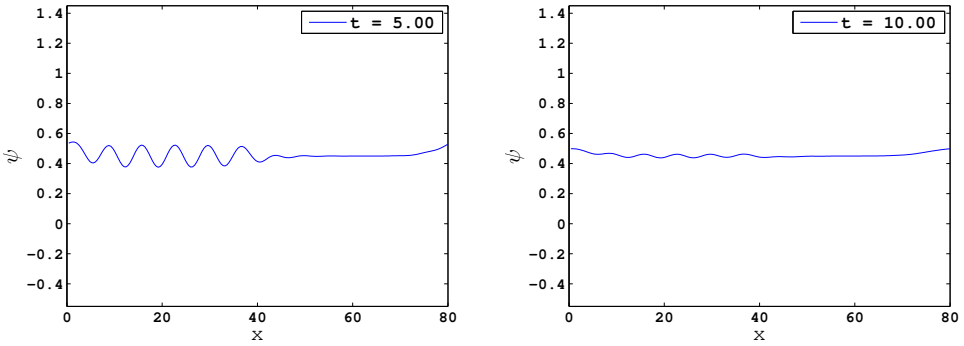

(a) The crystal is starting to melt. **(b)** The crystal is completely melted.

Figure 2.7: A crystal melting into the liquid phase. The figures show the process at two different timesteps. The parameters are $\epsilon = 0.2$ and $\psi_0 = 0.45$.

In Figure 2.6 a crystal has been placed in a liquid by initializing ψ as a sine function next to a constant function. The amplitude and the wavelength of the sine function were chosen from the results of the fitted curves in Figure 2.4. The behavior of the system depends on the values of ϵ and ψ_0.

Figure 2.7 shows the evolution of a system initialized as a crystal placed in a liquid. The values of the parameters were chosen to be $\epsilon = 0.2$ and $\psi_0 = 0.45$, which places the system in the constant region of the phase diagram. The temperature is below the melting point, but the choice of order parameter ensures that the system is in the constant phase. Under these conditions we would expect the crystal to melt, and the figure also shows the crystal rapidly disappearing into the liquid phase.

We also tried to grow a crystal. With $\epsilon = 0.4$ and $\psi_0 = 0.1$, we should be in the periodic region of the phase diagram. The starting point was very similar

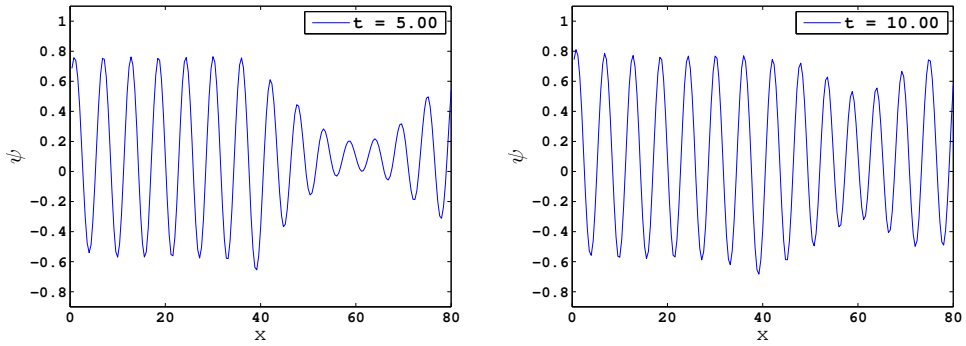

(a) The crystal is growing. **(b)** The order parameter is periodic.

Figure 2.8: The crystal is growing into the liquid phase. (a) and (b) show the simulation at two different times. The parameters are given as $\epsilon = 0.4$ and $\psi_0 = 0.1$.

to Figure 2.6, except that the values of ψ_0 and ϵ were different, and therefore also the amplitude of the crystal. The results in Figure 2.8 show the periodic phase expanding into the liquid phase. The crystal is growing. Because we have periodic boundary conditions, the crystal grows from both sides of the liquid.

We attempted to place a crystal in a liquid in the coexistence phase and let the system equilibrate as two coexisting phases. Then a hyperbolic tangent function was fitted to the interface between the crystal and the liquid, as was done in two dimensions by Backofen and Voigt [14]. We wanted to compare the results for different values of ϵ. The choices for ψ_0 that seemed to give the most stable results, were when we had different values for the crystal phase $\psi_{0,c}$ and the liquid phase $\psi_{0,l}$. $\psi_{0,c}$ was chosen from the boundary between the periodic and the coexistence phase, and $\psi_{0,l}$ from the boundary between the constant and the coexistence phase, as seen in the table below.

ϵ	$\psi_{0,l}$	$\psi_{0,c}$
0.3	-0.32	-0.29
0.35	-0.35	-0.28
0.4	-0.38	-0.27
0.45	-0.41	-0.27
0.5	-0.43	-0.26
0.55	-0.47	-0.26
0.6	-0.5	-0.25

The amplitude and wavelength of the initial crystal were chosen from the simulation results in Figure 2.3 and 2.4 for different ϵ. After a little time, the two phases seemed relatively stable. It is possible that the equilibration could have continued after the measurements were made, but in that case it happened very slowly. Because the calculation of the phase diagram is based on an approximation, a crystal in a liquid in the coexistence phase may never be completely

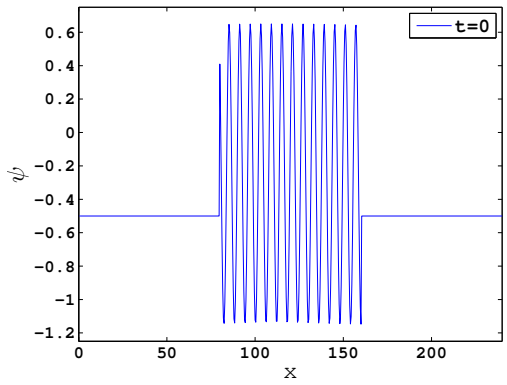

Figure 2.9: Initial configuration of a crystal placed in a liquid for the coexistence simulations. In this plot the parameters are $\epsilon = 0.6$, $\psi_{0,l} = -0.5$ and $\psi_{0,c} = -0.25$.

stable. The initial crystal placed in a liquid can be seen in Figure 2.9. The undercooling is $\epsilon = 0.6$, and the two phases have different values of ψ_0.

The coexistence simulations were performed for seven different values of ϵ. The results from four of them can be seen in Figure 2.10. When we believed that the crystal and the liquid were equilibrated and coexisting, we fitted tanh-functions to the interfaces on both sides of the crystal. In Figure 2.11, the tanh-functions from all seven simulations are plotted together, for both sides of the crystal. The left and the right interface have approximately the same steepness for the same ϵ value. As can be seen in Figure 2.11, the interface is sharper and the amplitude is larger for larger values of ϵ, or a deeper quench. This is the same trend that was also found in the 2D case by Backofen and Voigt [14]. We attempted to find a data collapse of the functions, but we were unable to find a good result.

2.2 The hyperbolic phase field crystal model in one dimension

In Section 2.1 we looked at results from simulations using the parabolic PFC equation. In this section we will examine the hyperbolic PFC equation as defined by Galenko and Elder [9],

$$\tau \frac{\partial^2 \psi}{\partial t^2} + \frac{\partial \psi}{\partial t} = \nabla^2[(-\epsilon + (1 + \nabla^2)^2)\psi + \psi^3] \tag{2.6}$$

where τ is the relaxation time of the flux to the steady state. This modified version of the PFC model includes fast dynamics. When ϵ is large, fast front dynamics can occur, and atoms can become trapped. This behavior can not be described by the parabolic equation [9].

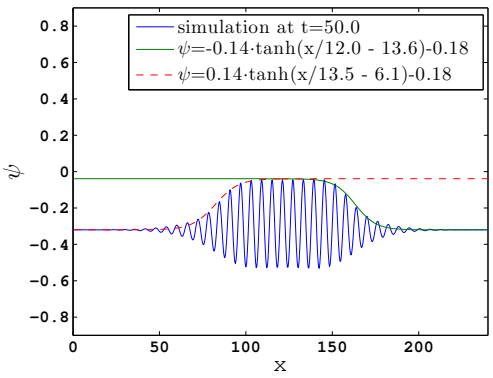

(a) $\epsilon = 0.3$.

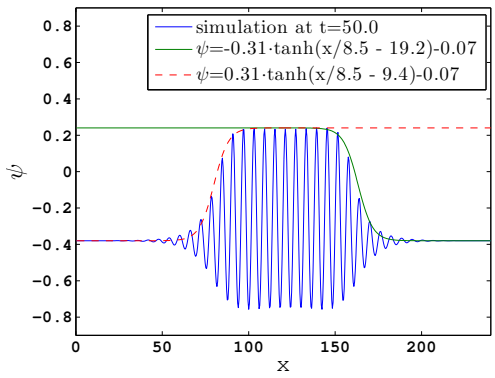

(b) $\epsilon = 0.4$.

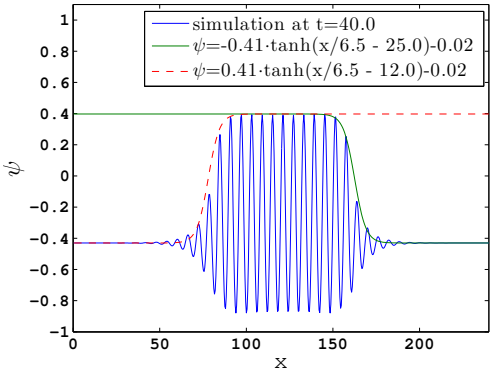

(c) $\epsilon = 0.5$.

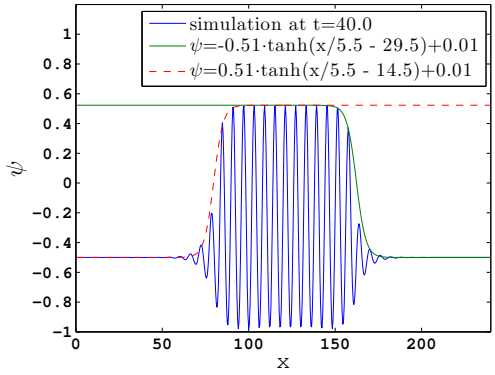

(d) $\epsilon = 0.6$.

Figure 2.10: The plots show the equilibrated systems with a crystal and a liquid in coexistence. tanh-functions are fitted to the interfaces.

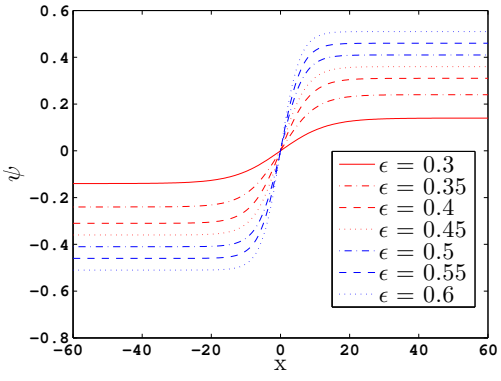

(a) Left side interface.

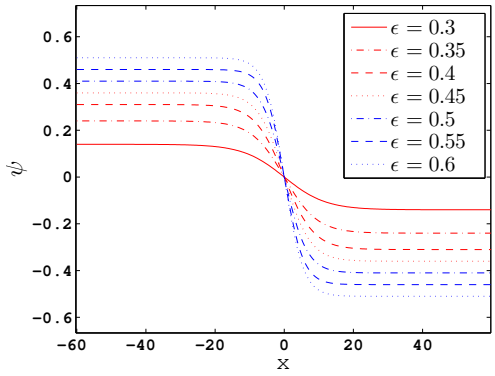

(b) Right side interface.

Figure 2.11: The tanh-functions fitted to the interfaces between the crystal and the liquid in the coexistence phase for different values of ϵ.

Galenko and Elder [9] used the one-dimensional case to look at the difference in the selection of velocity and wavenumber in the parabolic and hyperbolic case. In order to do this they performed a marginal stability analysis. The system that was studied was that of a solid front propagating into an unstable phase. A prediction was made for the front velocity V and the wavenumber k_f in the front for different ϵ and τ. An analysis of the Eckhaus instability was also made. In Figure 2.12 the results from this analysis can be seen. The calculations were made for $\tau = 0$, 2 and 5, where $\tau = 0$ corresponds to the parabolic equation. The front velocity can be seen to decrease when τ increases. The wavenumber k_f increases when τ increases. Both the front velocity and the front wavenumber increase with a larger quench. When the undercooling ϵ and the relaxation time τ is large, k_f enters the Eckhaus instability region. For each value of τ, there is a critical value of ϵ on the border between the metastable region and the Eckhaus instability region. The parabolic equation does not enter the unstable region.

In the rest of the chapter we will perform the marginal stability analysis and compare the results to our own simulations. Simulations of similar systems have been performed previously [15, 16], and we wanted to see if we could obtain the same results.

2.3 Marginal Stability Analysis

Galenko and Elder [9] performed a marginal stability analysis on the parabolic and the hyperbolic PFC equation in order to predict the pattern that would form behind a solid front moving into a homogeneous phase, in the one-dimensional case. A more general approach to the marginal stability analysis was examined by Dee and Langer [8]. The hypothesis is that the selected pattern in a front moving into a homogeneous phase is chosen from the edge of stability. In other words, it is marginally stable. The analysis is made in one dimension, so the pattern that forms behind the front is described by the wavenumber in the periodic solution. The velocity of the propagating front can also be determined from this analysis.

The stability analysis is performed by introducing a perturbation $\delta\psi$ of the order parameter ahead of the front. Because the values of ψ are small ahead of the front, we can linearize the PFC equation. We can make a Fourier transformation of this equation, or assume a solution on the form $\delta\psi = Ae^{\omega t+ikx}$, and put this into our equation. Either way, we find an expression for the dispersion relation $\omega(k)$, and perform the marginal stability analysis on this. We assume that the front moves at a constant velocity V.

The following conditions must be met for the equation to be marginally stable. The most unstable mode at the front is found at

$$iV + \frac{\partial\omega}{\partial k}\Big|_{k^*} = 0 \tag{2.7}$$

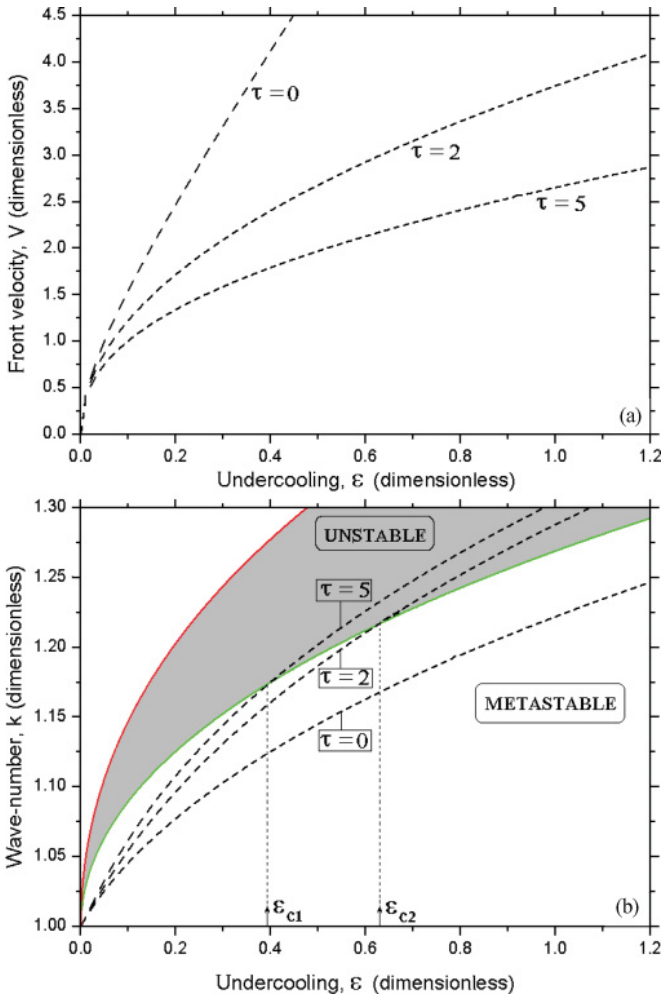

Figure 2.12: The results from the marginal stability analysis on the parabolic and hyperbolic PFC model as calculated by Galenko and Elder [9], p. 6. The calculations were made for $\tau = 0$ (parabolic PFC), $\tau = 2$ and $\tau = 5$. The top figure shows the velocity of a front propagating into an unstable phase for different values of ϵ and τ. The bottom figure shows the wavenumber k_f at the front for different ϵ and τ. The dashed region is a region of Eckhaus instability.

where k^* is the wavenumber at the front.

The front should be stationary in a reference frame moving with the velocity V, which gives the condition

$$\Re[ik^*V + \omega(k^*)] = 0 \tag{2.8}$$

When this condition is met, the front neither grows nor decays. If the front grows, the solution is no longer stable. If it decays it is stable, but if we want the marginally stable solution, the front must be stationary in the moving reference frame.

From these two equations we can find the velocity V of the front, and the wavenumber k^* at the front. If we want to find the wavenumber k_f that forms behind the front we need an additional condition. In the stationary reference frame, the peaks in the periodic solution are stationary. In the moving reference frame, the peaks move with a velocity $-V$. The frequency of the oscillations can be seen as a flux of nodes moving from the front into the bulk. The frequency at the front $\Omega = \Im[ik^*V + \omega(k^*)]$ must be equal to $k_f V$ in the bulk.

From this we find that the wavenumber that forms behind the front is

$$k_f = \frac{\Im[ik^*V + \omega(k^*)]}{V} \tag{2.9}$$

This wavenumber is different from the equilibrium wavenumber that minimizes the free energy of the system.

In order to solve the above equations we have to find the dispersion relation $\omega(k)$ for the parabolic and the hyperbolic case.

2.3.1 The parabolic equation

We first look at the parabolic case. The expansion $\delta\psi = \psi - \psi_0$ where $\psi_0 = 0$ is put into eq. 2.3. The equation is linearized, giving the expression

$$\frac{\partial \delta\psi}{\partial t} = \frac{\partial^2}{\partial x^2}\left[-\epsilon + \left(1 + \frac{\partial^2}{\partial x^2}\right)^2\right]\delta\psi \tag{2.10}$$

If we assume that the solution of this equation is on the form $\delta\psi = Ae^{\omega t + ikx}$, and put this into the equation, we get the dispersion relation

$$\omega = k^2\left(\epsilon - (1 - k^2)^2\right) \tag{2.11}$$

Putting this expression for ω into eq. 2.7- 2.9, we get the conditions

$$iV + \left.\frac{d\omega}{dk}\right|_{k^*} = iV + 2k^*[\epsilon - 1 + 4(k^*)^2 - 3(k^*)^4] = 0 \tag{2.12}$$

$$\Re\left[ik^*V + \omega(k^*)\right] = 0 \tag{2.13}$$

$$k_f = \frac{\Im[ik^*V + \omega(k^*)]}{V} \tag{2.14}$$

The wavenumber k^* has both a real and imaginary part:

$$k^* = k^*_{\mathrm{Re}} + ik^*_{\mathrm{Im}} \tag{2.15}$$

which has to be considered when solving the above equations.

As Galenko and Elder [9], we also solved these equations numerically. In order to do that the definition $k^* = k^*_{\mathrm{Re}} + ik^*_{\mathrm{Im}}$ was inserted into eq. 2.12. Then the equation was divided into two equations, a real and an imaginary part, as seen below,

$$iV + i2(\epsilon-1)k_{\mathrm{Im}} + i24k^2_{\mathrm{Re}}k_{\mathrm{Im}} - i8k^3_{\mathrm{Im}} - i30k^4_{\mathrm{Re}}k_{\mathrm{Im}} + i60k^2_{\mathrm{Re}}k^3_{\mathrm{Im}} - i6k^5_{\mathrm{Im}} = 0 \tag{2.16}$$

and

$$2(\epsilon-1)k_{\mathrm{Re}} + 8k^3_{\mathrm{Re}} - 24k_{\mathrm{Re}}k^2_{\mathrm{Im}} - 6k^5_{\mathrm{Re}} + 60k^3_{\mathrm{Re}}k^2_{\mathrm{Im}} - 30k_{\mathrm{Re}}k^4_{\mathrm{Im}} = 0 \tag{2.17}$$

Here we have used the notation $k = k^*$ to increase the readability of the expressions.

From eq. 2.17 we found k^*_{Im} as a function of k^*_{Re}:

$$k_{\mathrm{Im}} = \frac{\sqrt{15k^2_{\mathrm{Re}} - \sqrt{3}\sqrt{60k^4_{\mathrm{Re}} - 40k^2_{\mathrm{Re}} + 5\epsilon + 7} - 6}}{\sqrt{15}} \tag{2.18}$$

We were only interested in the real part of the solution. Then eq. 2.13 was rewritten like this

$$V = \frac{1}{k^*_{\mathrm{Im}}}\Re[\omega(k^*)] \tag{2.19}$$

so that V could be written as a function of k^*_{Re} and k^*_{Im}. Putting eq. 2.18 and 2.19 into eq. 2.16, and finding when this expression was equal to zero, gave us a value for k^*_{Re}. This value was then put into our expressions for V and k^*_{Im}, so that these quantities could be determined. k_f was found by putting our results for $k^* = k^*_{\mathrm{Re}} + ik^*_{\mathrm{Im}}$ and V into eq. 2.14. This procedure was performed for many different values of ϵ.

2.3.2 The hyperbolic equation

The marginal stability analysis was also performed on the hyperbolic case, eq. 2.6. Introducing the same perturbation as in the parabolic case, $\delta\psi = \psi - \psi_0$, where $\psi_0 = 0$, and linearizing the equation gives,

$$\tau\frac{\partial^2\delta\psi}{\partial t^2} + \frac{\partial\delta\psi}{\partial t} = \frac{\partial^2}{\partial x^2}\left[-\epsilon + \left(1 + \frac{\partial^2}{\partial x^2}\right)^2\right]\delta\psi \tag{2.20}$$

The perturbation is assumed to have the same form as in the parabolic case, $\delta\psi = Ae^{\omega t+ikx}$. Putting this into the above expression gives the relation,

$$\tau\omega^2 + \omega = k^2(\epsilon - (1-k^2)^2) \tag{2.21}$$

We define $\alpha(k) = k^2(\epsilon - (1-k^2)^2)$, and solve for ω,

$$\omega_\pm = \frac{-1 \pm \sqrt{1+4\tau\alpha(k)}}{2\tau} \tag{2.22}$$

In the following we use the solution ω_+ for the dispersion relation, because it describes the fastest growing modes, or the most unstable modes. Performing the marginal stability analysis in eq. 2.7- 2.9 on this dispersion relation gives the following equations,

$$iV + \frac{d\omega_+}{dk}\Big|_{k^*} = iV + \frac{2k^*[\epsilon - 1 + 4(k^*)^2 - 3(k^*)^4]}{\sqrt{1+4\tau\alpha(k^*)}} = 0 \tag{2.23}$$

$$\Re\left[iVk^* + \frac{\sqrt{1+4\tau\alpha(k^*)}-1}{2\tau}\right] = 0 \tag{2.24}$$

$$k_f = \frac{1}{V}\Im\left[iVk^* + \frac{\sqrt{1+4\tau\alpha(k^*)}-1}{2\tau}\right] \tag{2.25}$$

As before $k^* = k^*_{\mathrm{Re}} + ik^*_{\mathrm{Im}}$, and the equations have to be solved numerically. Equation 2.24 was rewritten like this

$$V = \frac{1}{k^*_{\mathrm{Im}}}\Re\left[\frac{\sqrt{1+4\tau\alpha(k^*)}-1}{2\tau}\right] \tag{2.26}$$

This expression for V was put into eq. 2.23. The resulting expression was solved numerically for $k^* = k^*_{\mathrm{Re}} + ik^*_{\mathrm{Im}}$. We took the absolute value of k^*_{Im}, as the numerical solution was negative. With a solution for k^*, we could find V. When the result for k^* and V were put into eq. 2.25 to find k_f, we also took the absolute value of this quantity.

Our results for the velocity and the wavenumber at the front can be seen in Figure 2.16 and 2.20. The figures show the result for the parabolic case and the hyperbolic case for $\tau = 2$ and 5. The figures also show the simulation results obtained in Section 2.4.

2.4 Results

In this section the spectral method [17, 18] was implemented, a new computational scheme to solve the differential equation in the PFC model. The spectral

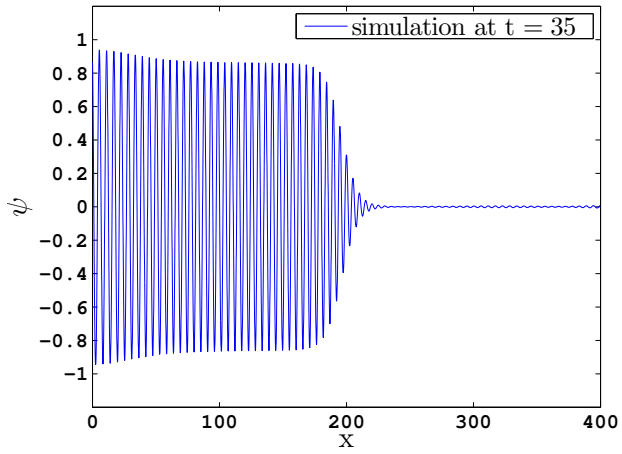

Figure 2.13: A propagating front for the parabolic case when $\epsilon = 0.7$. The center of the simulation "box" is at $x = 0$. This figure only shows the right half of the system.

method is explained in the Appendix. This method is more computationally efficient than the forward Euler method, because it uses a faster method of calculating the spatial derivatives. The method we have used solves the spatial derivatives by using the Fourier transform. The Fourier transform can transform a time or space dependent signal to a frequency dependent function. The benefit of using this scheme is that we can use larger time steps, which speeds up the computation. This is especially useful for the more complicated hyperbolic equation.

In order to test the results from the marginal stability analysis, a system with $\psi_0 = 0$ was initialized. The center of the system was initialized with small random fluctuations. The same random initial fluctuations were used in all the following simulations. In the simulations, a bulk with a periodic pattern was observed to form in the center of the system, and then move towards both sides of the system. This is the system we used to model a front propagating into a homogeneous liquid, the model that was used in the marginal stability analysis.

The propagating front in one of these simulations can be seen in Figure 2.13. This is a simulation of the parabolic equation. The front propagated from the center in both directions, but the figure only shows the right side of the simulation "box". In the following, our measurements were made on the propagating front on the right side of the system. In all the following simulations on the 1D case $\Delta x = 0.1$. For the parabolic case $\Delta t = 1 \cdot 10^{-4}$, and for the hyperbolic case $\Delta t = 8 \cdot 10^{-5}$.

The velocity was measured by first finding the position of the front as a function of time, as can be seen in Figure 2.14. The front was defined as the first peak on the right with an amplitude that was equal to or larger than $\psi_{\text{thresh}} = 0.2A$, where A is the amplitude of the bulk. This was the threshold of the

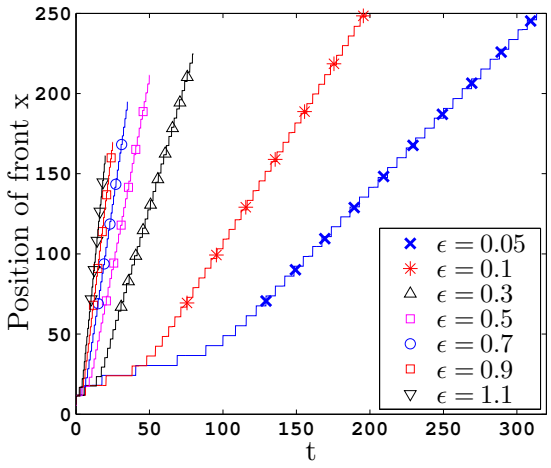

Figure 2.14: The position of the front as a function of time for $\tau = 0$. The solid lines show the position of the front peak. The markers indicate which ϵ the measurements are made for.

measurements on the front. As can be seen in the figure, the measurements are a little uneven in the beginning, because the bulk has not yet formed. Then they form a stair-like pattern, because the peaks in the front are stationary. In order for the front to move, a new peak has to appear and propagate the front. In order to find the velocity V, the position of the front is approximated by a linear fit $x(t) \approx Vt$, and the slope of this line is the velocity of the front. In order to find the position of the front, the systems with smaller ϵ are measured for the entire length of the system, while the systems with larger ϵ are measured for a smaller length. With larger ϵ the fluctuations ahead of the front began to form independent bulks, and the front quickly disappeared after that. This was observed in both the parabolic and the hyperbolic case. An example of this can be seen in Figure 2.15. This could be an effect of the periodic boundary conditions.

Measurements of the velocity for the parabolic case and the hyperbolic case for $\tau = 2$ and 5, can be seen in Figure 2.16. The measurements are made for $\epsilon = 0.05$, 0.1, 0.3, 0.5, 0.7, 0.9 and 1.1. The predictions from the marginal stability analysis are also plotted. For small ϵ the results agree very well with the prediction from the marginal stability analysis. When ϵ increases in the parabolic case, the simulation results for the velocity are a little smaller than the theoretical prediction. However, the results for the hyperbolic case seem to fit the theory very well.

When measuring the front velocity, we tried changing different parameters to discover what effect they had on our results. In Figure 2.17 the results from the parabolic case can be seen. The system size in the figure refers to the right half of the system, so when $x = 400$, the size of the entire system is $x = 800$. At

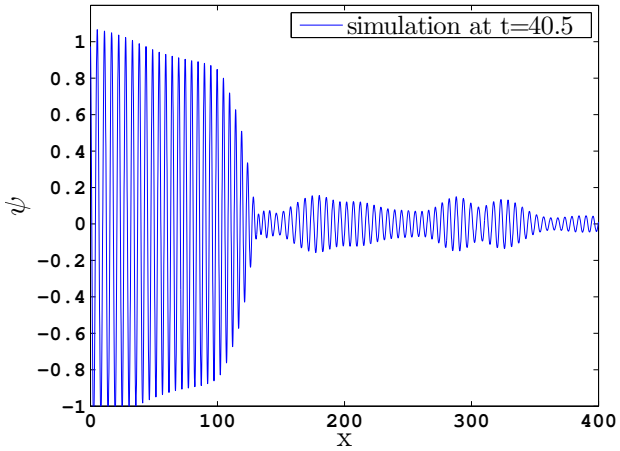

Figure 2.15: The right front of a system when $\tau = 2$ and $\epsilon = 0.9$.

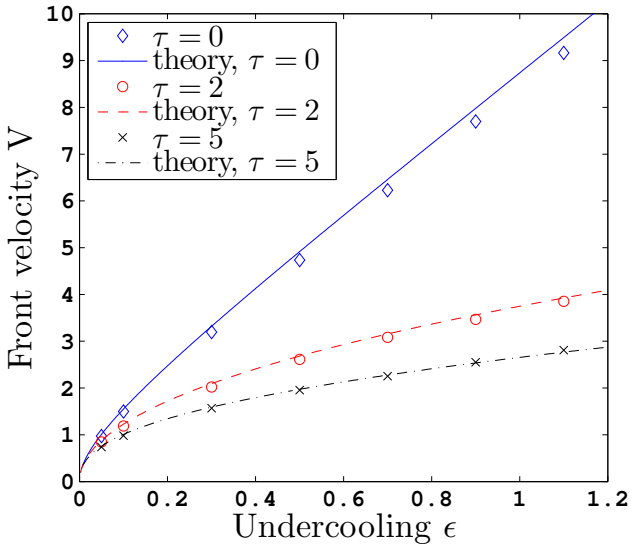

Figure 2.16: Front velocity as a function of the undercooling ϵ. The data points are simulation results, and the solid lines are the predictions made by the marginal stability analysis. These measurements were made with a system size $n = 8000$, a grid size $\Delta x = 0.1$ and a threshold of $0.2A$. The right half of the system, on which the measurements were made, had the size $x = 400$.

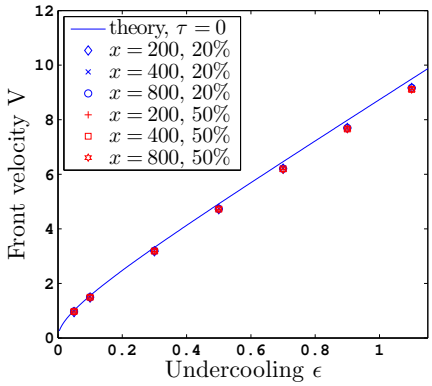

(a) Results for all ϵ.

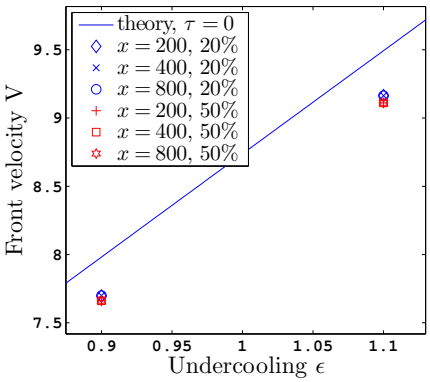

(b) Results for $\epsilon = 0.9$ and 1.1.

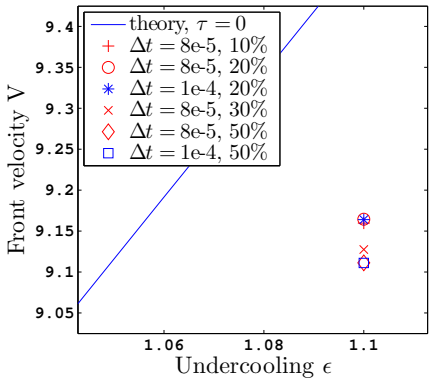

(c) Results for different Δt and ψ_{thresh}.

Figure 2.17: (a) Front velocity results from simulations of the parabolic PFC equation for different system sizes and thresholds. The system size x refers to the right half of the system. The thresholds 20% and 50% corresponds to $0.2A$ and $0.5A$. (b) A closer look at some of the results in (a). (c) Results from different timesteps and thresholds. The system size is $x = 400$ for all the results in (c).

first glance the results for different system sizes and thresholds look very similar. But there is a small difference in the results for the larger ϵ values. The different system sizes do not seem to change the velocity, but there is a slight difference between the thresholds $0.2A$ and $0.5A$, as can be seen in Figure 2.17b. When the threshold is small, the velocity is slightly closer to the prediction from the marginal stability analysis. The timestep of the simulations was also attempted changed, as can be seen in Figure 2.17c, but this did not have an effect on the results. Changing the threshold had a larger impact also here.

In Figure 2.18, we tried changing some of the parameters for $\tau = 2$ in the hyperbolic case. In Figure 2.18a the choice of threshold affects the results, while the results are independent of system size. For larger ϵ the difference in results for different thresholds increases. In Figure 2.18b the results are also affected by

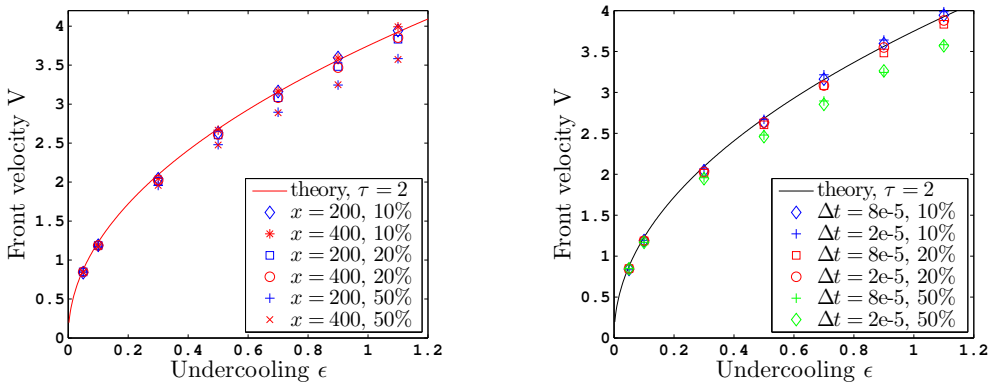

(a) Results for different x and ψ_{thresh}. **(b)** Results for different Δt and ψ_{thresh}.

Figure 2.18: (a) Front velocity results from simulations of the hyperbolic PFC equation with $\tau = 2$ for different system sizes and thresholds. The system size corresponds to the right half of the system, and the threshold 10% corresponds to $\psi_{\text{thresh}} = 0.1A$. (b) Results from simulations with different timesteps and thresholds. The system size is $x = 200$ for the simulation results in (b).

the choice of threshold, but not by the difference in timestep. As in the parabolic case, the choice of threshold affects the results more than the system size or the timestep. With smaller threshold the velocity increases and approaches the result from the marginal stability analysis. The effect is more pronounced in the hyperbolic case than in the parabolic case. The difference in results increases as ϵ increases.

What could be seen for $\tau = 2$ in Figure 2.18, can also be seen for $\tau = 5$ in Figure 2.19. Changing the system size gives a small difference in the results for the front velocity, while changing the threshold gives a larger difference. The front velocity increases when the threshold decreases. For the threshold $\psi_{\text{thresh}} = 0.1A$, the velocity is larger than the theory for the larger ϵ values.

We also made an attempt at finding the wavenumber behind the front. We did this by finding the average wavelength behind the front λ, and using this to find the wavenumber $k_f = 2\pi/\lambda$. We noticed that the amplitude of the crystal is slightly larger in the center of the bulk than it is closer to the front. This is especially apparent in the hyperbolic case, as can be seen in Figure 2.15, but it can also be seen in the parabolic case in Figure 2.13. Therefore, we did not include the peaks in the center when we found the wavenumber behind the front. We also did not include the area in the front, when the amplitude begins to decrease towards ψ_0. Our results are plotted in Figure 2.20. The results for the parabolic case are close to the predictions from the marginal stability analysis. For the hyperbolic case, the results are lower than the predicted values, and the results for the different values of τ are very similar. Because of the fluctuations ahead of the front that limit the lifespan of the propagating front, the simulation

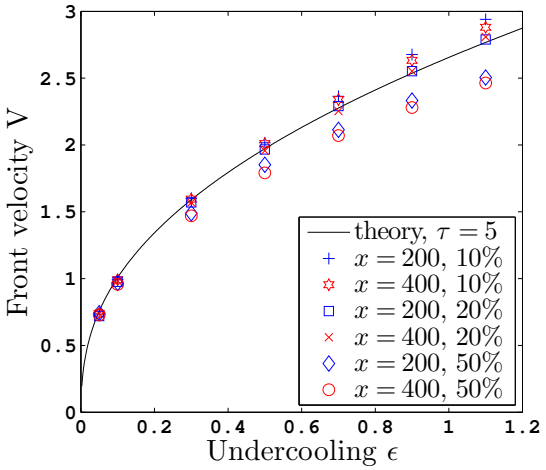

Figure 2.19: Front velocity results from the hyperbolic equation for $\tau = 5$, for different thresholds and system sizes.

is unable to run very long for large ϵ and τ. In the parabolic case, the number of peaks used to find the average wavelength is larger than in the hyperbolic case. This could make the results more accurate when $\tau = 0$.

We also let a simulation run for a long time, in order to let it equilibrate and find the equilibrium wavenumber. The results for the parabolic case when $\epsilon = 0.7$ can be seen in Figure 2.21. A relatively sharp peak has appeared at $k = 1.139$, but there are other wavenumbers present. A section of the order parameter ψ can also be seen with a sine function with the measured wavenumber. This is a very good fit, but at other places in the system they are slightly unsynchronized.

When $\tau = 2$ and $\epsilon = 0.7$, the bulk wavenumber was found to be $k = 1.107$. This value was also found for $\tau = 5$. These results are much lower than the k_f predictions for $\epsilon = 0.7$, but still higher than the equilibrium value at $k = 1$.

2.5 Summary of the 1D-case

In this chapter we have examined the parabolic and hyperbolic PFC equation in one dimension. We first solved the parabolic case using a finite difference scheme for both the time derivative and the spatial derivatives. We looked briefly at the effects of different initial conditions, and how these decided whether the system would end up in a constant phase or a periodic phase that could be described by the one-mode approximation. These results were predicted by the phase diagram in Figure 2.5. We spent some time with the coexistence phase, and made measurements on the interface between a periodic and a constant phase in coexistence. We observed the same trend as was found by Backofen and Voigt [14] when they performed simulations on a 2D system. The steepness of the interface

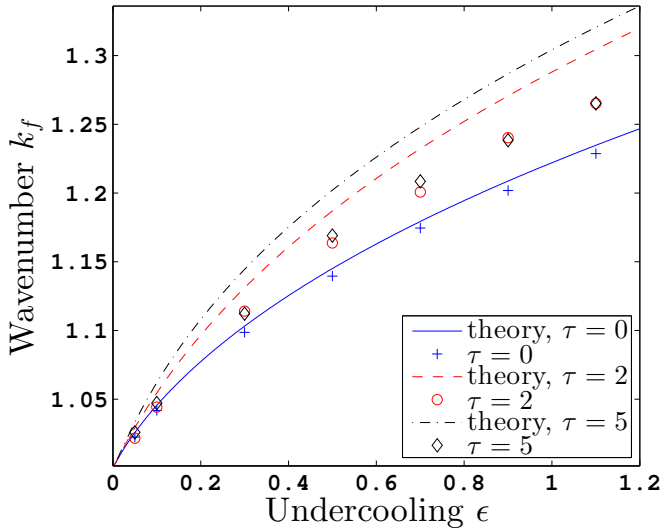

Figure 2.20: The wavenumber behind the front k_f as a function of the undercooling ϵ. The data points are simulation results, and the solid lines are the predictions made by the marginal stability analysis.

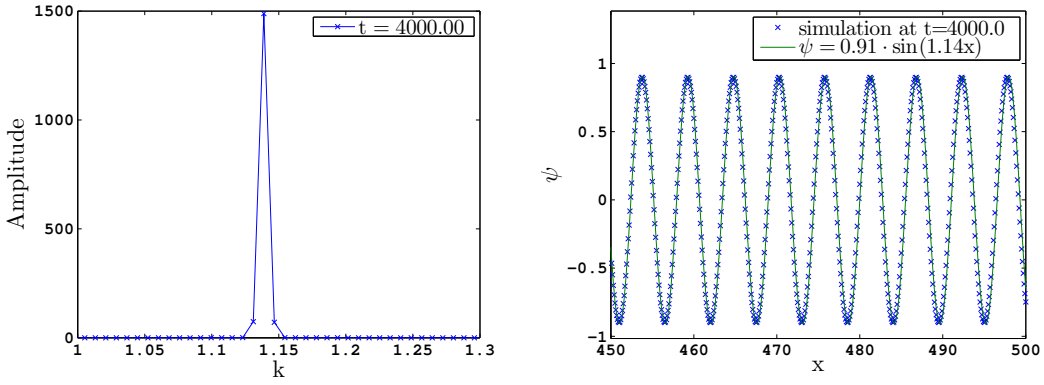

(a) Fourier analysis. **(b)** A section of ψ.

Figure 2.21: These plots show the results of an equilibrated system for the parabolic model when $\epsilon = 0.7$. (a) Fourier analysis that shows what wavenumbers are present in the system. (b) A section of the simulation results plotted with a sine function with the wavenumber found in (a).

and the amplitude of the crystal phase increased with increasing ϵ.

We then began to look at the marginal stability analysis of the PFC equation, in order to predict the behavior of the system. The marginal stability analysis is simpler to perform and test in the one-dimensional case than in two or three dimensions. We also wanted to look at the different behaviors of the parabolic and hyperbolic systems. In order to speed up the computation, a spectral method was implemented to calculate the spatial derivatives.

In both the parabolic and the hyperbolic case, the simulations with low values of ϵ are observed to be the most stable. For larger undercooling, the clearly defined front disappeared before it reached the end of the simulation "box". We assume that fluctuations ahead of the two fronts interact and grow into separate bulks that stop the propagation of the front. This limits the time that measurements of the front can be made for large ϵ and could be a source of error.

The results for the front velocity that seemed to give the best fit with the marginal stability analysis were for a system size $x = 400$ for the right half of the system, and the threshold $\psi_{\text{thresh}} = 0.2A$. When looking closer at the results from different simulations, the parameter that seemed to make the most difference was the value of the threshold. This would imply that the front changes shape over time. Changing the system size had a much smaller affect on the results. The effect of changing the threshold increased in the hyperbolic case. For the parabolic case, the effect was very small. It might be possible to look at the front velocity measurements as converging towards the theoretical predictions as the threshold is lowered. The exception is $\tau = 5$, where the results seem to increase further than the theoretical value for the largest ϵ-values. Because the marginal stability analysis is performed for a small amplitude perturbation, it is possible that the front should be defined as the first oscillation from the homogeneous liquid, which then gets picked up as the threshold is lowered.

For all the simulations, the results were less scattered for the small ϵ values, and these results were also the best match for the theory. This could be because the theory is derived for small amplitudes. It may be inaccurate for larger values of ϵ, as the amplitude increases with the undercooling.

The measurements of the front velocity have a good agreement with the theory, and the results for different τ are clearly differentiable. When we tried to measure the wavenumber behind the front k_f, as seen in Figure 2.20, our results were not so good. For the parabolic case, the results are close to the theory, but for the hyperbolic simulations k_f is lower than the theory predicts and the results are almost on top of each other. The predicted k_f for the two values of τ are relatively close to each other, so we would not expect a large difference between the simulation results for $\tau = 2$ and 5, but the measured k_f is clearly smaller than the theory predicts. There could be different explanations for this. The behavior observed for large ϵ, where independent bulks form ahead of the front and stop the propagation of the front, could have something to do with it. Under these

conditions, the number of peaks in the front could be too small to give accurate measurements. There is also a possibility that the method we have used might not give the most accurate results. We have found the wavenumber by measuring the average wavelength of the peaks behind the front, and using this to determine k_f. But we have made some assumptions regarding exactly where the front and the area behind the front is. It is possible we have misunderstood where k_f and k^* are to be found. Previous simulations on similar systems [15, 16] seem to have measured different parts of the system to find k_f. We considered using the Fourier transform, as seen in Figure 2.21a to find k_f, but there were either too many frequencies present to determine which one was k_f, or the resolution was not high enough to get good results.

Galenko and Elder [9] also find which wavenumbers could be affected by the Eckhaus instability, as can be seen in Figure 2.12. The theory predicts that the wavenumbers for $\tau = 2$ and 5 enter the Eckhaus instability region when ϵ increases. It is possible that this could also have affected our measurements of the wavenumber k_f to some degree. We are not sure how the Eckhaus instability might affect the system.

This concludes our examination of the 1D PFC equation. The systems we have studied in this chapter are relatively abstract, but will hopefully provide a basic understanding of the PFC equation as we study two-dimensional crystals in Chapter 3, 4 and 5.

Chapter 3

The PFC equation in 2D

3.1 Introduction

In one dimension, the solid phase was shown as a sine function. In two dimensions, the phase field crystal model can solidify in two forms of patterns. The solid phase appears as a striped pattern or a hexagonal pattern, depending on the values of the initial order parameter ψ_0 and the undercooling ϵ. A phase diagram can be seen in Figure 3.1.

An example of both a hexagonal and a striped pattern emerging from random initial fluctuations can be seen in Figure 3.2. The atoms are identified here as the maxima of the system. The atoms are placed at minima when ψ_0 is positive, and at maxima when ψ_0 is negative.

In two dimensions the modeled system shows more complicated behaviour than in one dimension. We can model polycrystalline materials with different crystal orientations and examine the long-term behaviour of these complicated systems. We can also identify dislocations and track their progression. The dynamics of the system as it attempts to reach the state with the minimum free energy is called coarsening.

3.2 The equilibrium crystal

As in one dimension, it is possible to calculate the equilibrium crystal in two dimensions using the one-mode approximation of ψ. Elder and Grant [6] calculated the one-mode approximation for the triangular phase to be

$$\psi = \psi_0 + A \sum_{j=1}^{3} e^{i\mathbf{k}_j \cdot \mathbf{r}} \; + \; \text{c.c.} \tag{3.1}$$

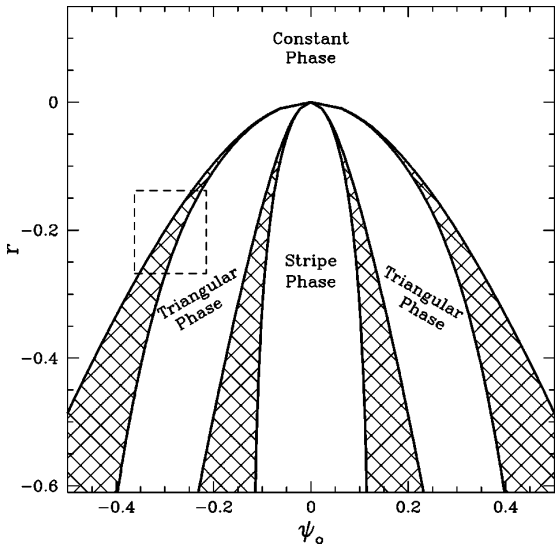

Figure 3.1: Phase diagram for the PFC equation in two dimensions, calculated by Elder and Grant [6], p. 7. The r on the y-axis is equal to $-\epsilon$. The constant phase is the liquid phase, and the periodic phase is the triangular and the stripe phase. The triangular phase is a hexagonal pattern. The hatched regions are the coexistence phases.

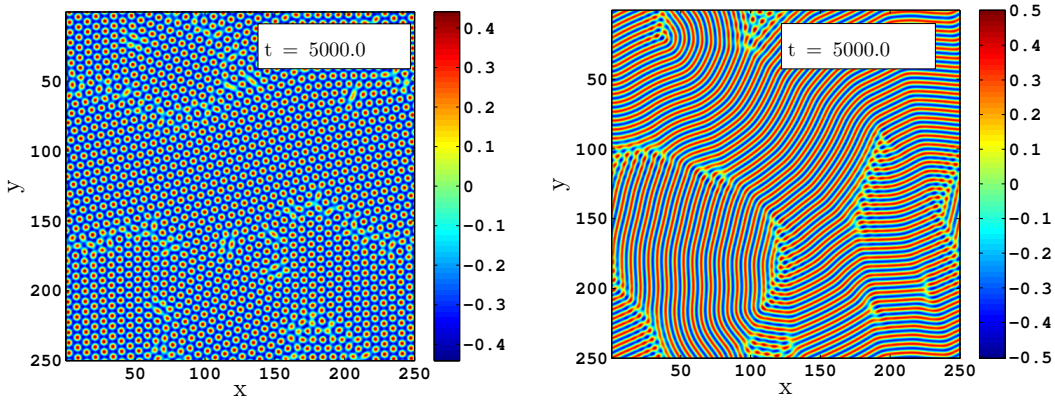

(a) Triangular phase **(b)** Stripe phase

Figure 3.2: Results of the PFC model in 2D from random fluctuations around ψ_0. (a) Results from a simulation with the parameters $\epsilon = 0.1$ and $\psi_0 = -0.12$, which puts the system in the triangular phase. The peaks represent atoms. The system size is 500×500 with $\Delta x = 0.5$, at $t = 5000$. (b) Results from a simulation with the parameters $\epsilon = 0.1$ and $\psi_0 = 0$, which puts the system in the stripe phase of the phase diagram. The system size is $n = 500$ with $\Delta x = 0.5$, at $t = 5000$.

where A is the amplitude, c.c is the complex conjugate and the $\mathbf{k}_j$ vectors are

$$\mathbf{k}_1 = \left(-\frac{\sqrt{3}}{2}, -\frac{1}{2}\right) \tag{3.2}$$

$$\mathbf{k}_2 = (0, 1) \tag{3.3}$$

$$\mathbf{k}_3 = \left(\frac{\sqrt{3}}{2}, -\frac{1}{2}\right) \tag{3.4}$$

These three vectors describe the triangular phase of the solid state. They are the basis vectors of the hexagonal pattern of the equilibrium state, given the appropriate values of ψ_0 and ϵ.

The expression for ψ can also be written as

$$\psi = \psi_0 + A \cdot 2\Re\left\{\sum_{j=1}^{3} e^{i\mathbf{k}_j \cdot \mathbf{r}}\right\} \tag{3.5}$$

In order to find A, the one-mode approximation of ψ is put into the expression for the free energy

$$F = \int d\mathbf{r}\left\{\psi\left[-\epsilon + (1+\nabla^2)^2\right]\frac{\psi}{2} + \frac{\psi^4}{4}\right\} \tag{3.6}$$

and the expression is integrated over one cell in order to find the total free energy in that cell. We want to find when the free energy differentiated with respect to the amplitude is equal to zero. When $dF/dA = 0$ the free energy is minimized, and the equilibrium state can be found when the free energy is at a minimum. Therefore we can solve this equation, and find the amplitude of the equilibrium state. Solving this equation gives two solutions for A

$$A_+ = \frac{1}{15}(-3\psi_0 + \sqrt{15\epsilon - 36\psi_0^2}) \tag{3.7}$$

and

$$A_- = \frac{1}{15}(-3\psi_0 - \sqrt{15\epsilon - 36\psi_0^2}) \tag{3.8}$$

A_+ gives the minimum of the free energy when ψ_0 is negative, A_- gives the minimum of the free energy when ψ_0 is positive.

We can rotate the crystal by multiplying the $\mathbf{k}_j$ vectors with a rotation matrix

$$R = \begin{bmatrix}\cos\theta & -\sin\theta \\ \sin\theta & \cos\theta\end{bmatrix} \tag{3.9}$$

where θ specifies the desired rotation angle.

3.3 Elastic excitations in the PFC model

As mentioned in Chapter 1, there are different versions of the PFC model. The versions we have simulated in this thesis are the standard, parabolic equation and the hyperbolic equation. However, a recent article by Heinonen et al. [12] suggests that neither of these equations model elastic dynamics correctly. We will describe their alternative formulation of the model, and dicuss the implications of their argument.

Heinonen et al. [12] argue that the standard phase field crystal model does not model elastic excitations correctly. Elastic excitations occur on a much smaller time scale than the diffusive dynamics described by the PFC equation. The authors claim that while the PFC model does include elastic excitations, they are modeled on a diffusive time scale when they should occur almost instantaneously. They suggest a method to avoid this effect. It involves separating the time scales for elastic and diffusive dynamics by mechanically equilibrating the system for each time step. The hyperbolic PFC equation was intended to address this issue [9], but Heinonen et al. [12] claim that their method gives more accurate results.

The approach uses the amplitude formulation of the PFC equation. This is a version of the PFC model that is closer to the continuum models at macroscopic scales. In this version of the PFC model, the amplitudes of the periodic ψ-field are complex, and contain information about the state of the system, deformations and crystal orientations. They also naturally separate out elasticity in the imaginary part of the amplitude equations. When the divergence of the stress tensor is zero, $\nabla \cdot \sigma = 0$, there is elastic equilibrium. This property is used to derive the elastic equilibrium conditions for the crystal phase.

The method is tested by performing several numerical simulations. In a 1D simulation with the amplitude formulation of the PFC equation, but without the mechanical equilibrium condition, a compressed crystal is placed in an undercooled liquid. When the simulation begins the whole system solidifies. Without the elastic equilibrium condition, the system is observed to solidify too fast for it to reach elastic equilibrium. In elastic equilibrium the crystal should no longer be compressed. According to the theory of elastic strains, the crystal should have stretched almost immediately. Instead, the system is in a strained state, and the simulation has to run for a long time before it is equally strained along the length scale. When the same system is simulated with the elastic equilibrium condition, the ψ-field solidifies more quickly, suggesting that the elastic dynamics of the system also affects the evolution of the ψ-field.

A 2D simulation was also performed. The two-grain system that was studied was the same that we will examine when we look at the 2D case in the next chapters. A circular crystal was placed inside a larger crystal with a different crystal orientation. The difference in crystal orientation is described by a misorientation

angle θ. Two systems were simulated, a warm system and a cold system. The parameters of the warm system corresponded to the parabolic PFC simulations performed by Wu and Voorhees [19], in order to compare results. We will take a closer look at the results of their paper and the theory of grain growth and rotation in Chapter 4. Heinonen et al. [12] set the misorientation angle to be $\theta = 5°$ to allow rotation of the center grain. The rotation is the elastic deformation in this case. For the warm case, they found that the results from the amplitude PFC equation agrees with the results from the standard PFC equation from Wu and Voorhees [19] and the results with the mechanical equilibrium condition. The authors believe that this agreement is caused by the choice of parameters placing the system close to the liquid state. The elastic energy is very small close to this state.

The cold case looks very different. The difference between the results with and without the mechanical equilibrium condition is large. The grain shrinks nearly ten times as fast with the mechanical equilibrium condition, which is also faster than in the warm case. As in the 1D case, the evolution of the ψ-field depends on the elastic dynamics. But the results also show that with the elastic equilibrium condition, the growth is faster for cold systems than warm systems.

Heinonen et al. [12] show that the elastic excitations affect the dynamics of the ψ-field, and that the standard PFC equation does not always model the dynamics correctly. When the quenching depth is large, the correct modeling of elastic excitations becomes more important. As we have not included the mechanical equilibrium condition in our simulations, there is a possibility that our results are not correct. We will discuss this possibility in Chapter 6.

Chapter 4

Grain growth and stagnation

In this chapter the theory behind grain growth will be explained. The classical grain growth theory will briefly be shown, before the Cahn-Taylor model [10] is examined. This model has been tested by different simulations [19, 20], and these papers will be summarized. This chapter is mostly concerned with cylindrical, two-grain systems. However, the dynamics of triple junctions [21, 19] is also briefly examined. This thesis is mostly concerned with the two-grain system, but triple junctions is a very important part of more complicated polycrystalline materials.

Stagnation of grain growth is examined by summarizing different papers that have studied the theory of this phenomenon [2] and examined the causes in simulations [3, 4]. An overview of their results will be given at the end of the chapter.

4.1 Grain growth theory

4.1.1 Classical grain growth

Following the derivation by Wu and Voorhees [19], the classical equation giving the normal velocity of the grain boundary is

$$v_{\mathbf{n}} = M\gamma\kappa \tag{4.1}$$

where M is the mobility, γ is the grain boundary energy and κ is the mean curvature of the grain boundary. When the grain boundary is circular the mean curvature can be written as $\kappa = 1/R$, where R is the radius. In order to find the growth dynamics, we can rewrite the above equation like this:

$$\frac{dR}{dt} = -\frac{M\gamma}{R} \tag{4.2}$$

The negative sign is included in order to look at shrinkage. If there is no rotation of the grains, the mobility and the grain boundary energy is constant, and we

can solve the problem as an integral:

$$\int_{R_0}^{R(t)} RdR = -M\gamma \int_0^t dt \tag{4.3}$$

which gives the solution

$$R^2(t) = R_0^2 - 2M\gamma t \tag{4.4}$$

This result shows that the area of the grain is expected to decrease linearly in time. This classical description does not include grain rotation or applied stress, but it can be used as an approximation of grain growth dynamics in certain circumstances.

4.1.2 The Cahn-Taylor model

Cahn and Taylor developed a unified model of grain boundary motion and grain rotation [10]. In two dimensions, the grain boundary velocity has two components, a component $v_{\mathbf{n}}$, that is normal to the grain boundary, and a component $v_{\parallel}$, that is tangential to the grain boundary. It is postulated that coupling of the normal and tangential velocity, and tangential motion caused by sliding of the grain boundary, can be expressed as a unified theory,

$$v_{\parallel} = S\sigma + \beta v_{\mathbf{n}} \tag{4.5}$$

where β is the coupling constant, and S is the sliding coefficient. Sliding is driven by tangential stress σ. It is assumed that the coupling constant is a function of the misorientation, $\beta = \beta(\theta)$.

The nomal velocity $v_{\mathbf{n}}$ is assumed to be linear to the driving force P, $v_{\mathbf{n}} = MP$, where M is the mobility. The rate of change of the volume free energy plus the work done by the stress is

$$\frac{dF}{dt} + \frac{dW}{dt} = -(f_V v_{\mathbf{n}} + \sigma v_{\parallel}) = -(Pv_{\mathbf{n}} + S\sigma^2) \tag{4.6}$$

where $P = f_V + \sigma\beta$ is the driving force. In the above equation we used the definition of $v_{\parallel}$ from eq. 4.5. From this relation we can now write the expression for $v_{\mathbf{n}}$ like this,

$$v_{\mathbf{n}} = M(f_V + \sigma\beta) \tag{4.7}$$

and eq. 4.5 can then be rewritten,

$$v_{\parallel} = S\sigma + \beta M(f_V + \sigma\beta) \tag{4.8}$$

In the simplest case, when the motion is driven by curvature and both S and β is zero, there is no coupling or sliding. If the interface is cylindrical with a radius R, the velocities of a cross-section area of the cylinder are

$$v_{\mathbf{n}} = \frac{M\gamma}{R} \tag{4.9}$$

$$v_{\parallel} = 0 \tag{4.10}$$

The normal motion is driven by curvature and there is no rotation. This is consistent with the classical theory. The unit vector $\mathbf{n}$ points into the cylinder.

Grain growth with small θ

If the misorientation θ is small, dislocations are clearly identifiable in the grain boundary. A pure symmetric tilt boundary has no motion caused by sliding, only coupling. By geometry, the tangential velocity is found to be $v_{\parallel} = 2\tan(\theta/2)v_{\mathbf{n}} \approx \theta v_{\mathbf{n}}$, which means that $\beta \approx \theta$ for small θ. If there is only one type of dislocation the misorientation can be written as $\theta = \rho b$, where ρ is the density of dislocations and b is the length of the Burgers vector that defines the dislocation type. For a grain boundary with different types of dislocations the misorientation is found to be $\theta_{\mathbf{n}} = \sum_i \rho_i \mathbf{b}_i$, where the different types of dislocations i are summed up. The glide force on a dislocation is found to be $f = -\sigma b$ while the climb force is found to be zero. With the assumption that the velocity is linear to the driving force with the mobility as the linearity constant, for a single type of dislocation the normal velocity becomes $v_{\mathbf{n}} = M_b b\sigma$. With different types of dislocations the velocity becomes

$$v_{\mathbf{n}}\mathbf{n} = \frac{1}{\sum_i \rho_i / M_{b_i}} \left(\sum_i \rho_i \mathbf{b}_i \right) \sigma \tag{4.11}$$

where the mobility $M = 1/(\sum_i \rho_i / M_{b_i})$. In the above expression the dislocations are assumed to have different mobilities M_i, but there are no dislocation reactions. With one type of dislocation the mobility becomes $M = M_b/\rho = M_b b/\theta$. This gives the normal velocity as $v_{\mathbf{n}}\mathbf{n} = M\beta\sigma_{\mathbf{n}}$.

The Cahn-Taylor model applied to the two-grain system

In the rest of this section the Cahn-Taylor model is applied to a cylindrical crystal placed inside a crystal with a different orientation. The cross-section of the cylinder is in two dimensions. The embedded crystal has a misorientation $\theta(t)$ and a radius $R(t)$. It is assumed that the crystal will rotate. The change in θ and R, and the relation to $v_{\parallel}$ and $v_{\mathbf{n}}$ can be expressed like this,

$$R(t)d\theta = v_{\parallel}dt \quad \text{or} \quad v_{\parallel} = R(t)\frac{d\theta}{dt} \tag{4.12}$$

$$dR = -v_{\mathbf{n}}dt \quad \text{or} \quad v_{\mathbf{n}} = -\frac{dR}{dt} \tag{4.13}$$

The driving force can be found from the rate of reduction of the total free energy and the rate of work done by an applied tangential stress. The total free energy consists of the surface free energy and the bulk free energy. The surface

free energy is defined as the length of the grain boundary multiplied with the grain boundary energy. The bulk free energy is determined by the area of the cross-section multiplied with the volume free energy. The rate of reduction of the free energy is,

$$\frac{dF}{dt} = \frac{d}{dt}(2\pi R(t)\gamma(\theta(t)) + \pi R^2 f_V) \tag{4.14}$$

and the rate of work done by an applied tangential stress is,

$$\frac{dW}{dt} = -2\pi R^2 \sigma \frac{d\theta}{dt} \tag{4.15}$$

The sum of these equations can be written like this,

$$\frac{dF}{dt} + \frac{dW}{dt} = 2\pi R \left(\left(\frac{\gamma}{R} + f_V \right) \frac{dR}{dt} + \left(\frac{\gamma'}{R} - \sigma \right) R \frac{d\theta}{dt} \right) \tag{4.16}$$

where $\gamma' = d\gamma/d\theta$.

In the above equation the terms γ/R and $-\gamma'/R$ can be interpreted as additions to respectively f_V and the applied stress σ. By using the addition to the applied stress σ and the expressions for the velocities $v_{\mathbf{n}}$ and $v_{\parallel}$ in eq. 4.12 and 4.13, eq. 4.5 can be rewritten,

$$R\frac{d\theta}{dt} = -\beta \frac{dR}{dt} + S\left(\sigma - \frac{\gamma'}{R} \right) \tag{4.17}$$

This is a rephrasing of the tangential velocity $v_{\parallel}$ as a function of coupling and sliding, but here the addition to the applied stress σ that was found in eq. 4.16 is included.

This expression for $R(d\theta/dt)$ is then inserted into the rate of change of the free energy plus the work done in eq. 4.16, and the expression becomes

$$\frac{dF}{dt} + \frac{dW}{dt} = 2\pi R \left(\left(\frac{\gamma}{R} + f_V - \beta \left(\frac{\gamma'}{R} - \sigma \right) \right) \frac{dR}{dt} - S \left(\frac{\gamma'}{R} - \sigma \right)^2 \right) \tag{4.18}$$

This equation can be interpreted to give the driving force for normal grain boundary motion as $P = f_V + \frac{\gamma - \beta\gamma'}{R} + \beta\sigma$. Because we have assumed a linear relationship between the velocity $v_{\mathbf{n}}$ and the driving force, with the mobility M as the constant of linearity, $v_{\mathbf{n}}$ can now be written as,

$$-v_{\mathbf{n}} = \frac{dR}{dt} = -M \left(f_V + \frac{\gamma - \beta\gamma'}{R} + \beta\sigma \right) \tag{4.19}$$

and by putting this expression for the normal velocity into the expression for the tangential velocity $v_{\parallel}$ in 4.17, the following equation is obtained,

$$v_{\parallel} = R\frac{d\theta}{dt} = \beta M \left(f_V + \frac{\gamma - \beta\gamma'}{R} + \beta\sigma \right) - S\left(\frac{\gamma'}{R} - \sigma \right) \tag{4.20}$$

It is possible to get a timeless relation between θ and R. The direct relation between the misorientation θ and the radius R can be found by dividing $v_{\|}$ with $v_{\mathbf{n}}$, which results in

$$\frac{d\theta}{d\ln R} = -\beta + \frac{(\gamma'/R - \sigma)}{M[f_V + (\gamma - \beta\gamma')/R + \beta\sigma]}S \tag{4.21}$$

These three equations describe the dynamics of a two-grain cylindrical system, as predicted by the Cahn-Taylor model. By examining these equations for special cases, new information and predictions can be obtained. In the following the cases where there is no coupling or sliding, only coupling, and only sliding will be further examined.

Two-grain system with no coupling or sliding

When there is no coupling or sliding ($\beta = 0$ and $S(\sigma - \gamma'/R) = 0$), the tangential velocity $v_{\|} = 0$, which means there is no rotation. The equation for $v_{\mathbf{n}}$ is reduced to

$$-v_{\mathbf{n}} = \frac{dR}{dt} = -M\left(f_V + \frac{\gamma}{R}\right) \tag{4.22}$$

If $f_V = 0$, the motion is driven by curvature, as in the classical description of grain growth. By integrating the equation, the grain growth is found to be $R^2(t) = R^2(0) - 2M\gamma t$. The area of the grain grows linearly. This is the same result as in the classical case.

Two-grain system with only sliding

If, however, there is only sliding ($\beta = 0$), the new equations for the velocity are

$$\frac{dR}{dt} = -M\left(f_V + \frac{\gamma}{R}\right) \tag{4.23}$$

$$R\frac{d\theta}{dt} = -S\left(\frac{\gamma'}{R} - \sigma\right) \tag{4.24}$$

These equations give different results depending on the applied stress σ, the volume free energy f_V and $d\gamma/d\theta$. The direction of rotation can be determined from the sign of $(\gamma'/R) - \sigma$. If $\sigma = 0$, the grain rotation $d\theta/dt = -S\gamma'/R^2$ wants to decrease the grain boundary energy γ. However, for small θ, the Read-Shockley relation gives $\gamma(\theta) = a_1|\theta| + a_2|\theta|\ln(1/|\theta|)$. As θ approaches 0, $d\gamma/d\theta$ goes to infinity. If the grain wants to rotate to decrease γ, it has to rotate to increase θ.

If $f_V = 0$ and $\sigma = 0$, the normal velocity becomes $dR/dt = -M\gamma/R$, which looks like the classical equation, but behaves differently because of the grain rotation. M and γ is dependent on the misorientation, and when there is rotation, they are no longer constant.

Under these conditions eq. 4.21 becomes

$$\frac{d\theta}{d\ln R} = \frac{S\gamma'}{M\gamma} \tag{4.25}$$

This equation can be integrated if the parameters $\gamma(\theta)$, $S(\theta)$ and $M(\theta)$ are known. From the Read-Shockley relation for small θ the approximation $\gamma'/\gamma \approx 1/\theta$ can be found. Whether the grain reaches coincidence before the grain radius is zero, depends on the assumptions made about M and S.

The misorientation of the grain does not necessarily go to zero. There are local minima of γ that can give a constant θ, if the grain rotates to this value of $\gamma(\theta)$.

Two-grain system with only coupling

If there is only coupling ($S = 0$), the velocity equations become,

$$-v_{\mathbf{n}} = \frac{dR}{dt} = -M\left(f_V + \frac{\gamma - \beta\gamma'}{R} + \beta\sigma\right) \tag{4.26}$$

$$v_{\parallel} = R\frac{d\theta}{dt} = \beta M\left(f_V + \frac{\gamma - \beta\gamma'}{R} + \beta\sigma\right) \tag{4.27}$$

The relation between θ and R becomes

$$\frac{d\theta}{d\ln R} = -\beta \tag{4.28}$$

This means that if the misorientation θ is found not to depend on the grain radius R, there is only coupling in the system. For small θ this equation gives an interesting result. As was found earlier, if θ is small, $\theta \approx \beta$. If also $\sigma = 0$, eq. 4.28 can be written $d\ln|\theta|/d\ln R = -1$. By integrating this equation the solution $R(t)\theta(t) = R_0\theta(R_0) =$ constant is found. This means that the dislocations are conserved in the coupling-only case. It also means that as $R(t)$ decreases, θ must increase, even if this increases the grain boundary energy. This is possible because the grain shrinks fast enough that $\int \gamma\, dA$ decreases even though γ increases.

In the general case, the direction of the grain rotation depends on the coupling constant β. When $\beta(\theta) = 0$, θ is constant. If $\beta(\theta_i) = 0$ and θ is close to θ_i, β can be approximated by $\beta(\theta) = \beta'(\theta_0)(\theta - \theta_i)$. Whether the grain rotates towards or away from θ_i depends on the sign of $\beta'(\theta_i)$, but integrating $d\theta/d\ln R = -\beta$ shows that the grain actually only rotates towards θ_i when the grain radius approaches zero.

If there is an applied stress σ, the motion will still be caused by coupling, as seen in the equations above. If $\beta\sigma = f_V + (\gamma - \beta\gamma')/R$, both $v_{\mathbf{n}}$ and $v_{\parallel}$ will be zero. Under these circumstances all motion stops.

For small θ, when $f_V = 0$ and $\sigma = 0$, the approximation $\gamma - \beta\gamma' = a_2|\theta|$ can be made. The normal velocity becomes $-v_{\mathbf{n}} = -M_b b a_2/R$. The grain growth becomes $R^2(t) = R_0^2 - 2M_b|b|a_2 t$, which has a temperature dependence, unlike the classical grain growth. θ increases even though γ' is positive, because $\int \gamma \, dA$ decreases as θ increases.

Summary of the predictions from the Cahn-Taylor model

In conclusion, when a grain boundary moves there can be both coupling and sliding present, causing the grain to rotate. In general, rotation driven by coupled motion causes the misorientation θ to increase, while rotation driven by sliding causes θ to decrease. In both cases the decrease of grain boundary energy drives the system. When there is only coupling and θ is sufficiently small, the dislocations are conserved. When there is only sliding, the number of dislocations must decrease. If there is sliding present in the system it must be possible for dislocations to annihilate. If the number of dislocations is not conserved, there is sliding present in the system.

4.2 Simulation papers on bicrystal grain growth

4.2.1 A PFC study

Wu and Voorhees [19] performed PFC simulations on a two-grain and a three-grain system, in order to measure grain growth and rotation. The systems were in 2D. The following summary describes the two-grain system, which is also called a bicrystal. The three-grain system is described in Section 4.4.2. The circular crystal embedded in another crystal with a different orientation is the same system that the Cahn-Taylor model [10] was applied on above.

The model

The bicrystal is implemented as a circular grain with one crystal orientation placed inside a larger grain with a different crystal orientation. The simulations are performed for different values of the misorientation θ. The grain boundary between these two grains is found by identifying the crystal defects. In an ideal hexagonal crystal, every atom has six neighbours. Defects often appear as a pair of atoms with five and seven neighbours, but a defect can be defined as any atom with another number of neighbours than six.

Grain growth and rotation

In the simulations the undercooling ϵ and the initial order parameter ψ_0 are held fixed relatively close to the melting point, while the misorientation θ is varied.

With the hexagonal crystal structure $\theta = 15°$ is a large misorientation angle, while $\theta = 5°$ is a small misorientation angle. As is consistent with the classical theory expressed in eq. 4.4, for both large and small misorientations the domain area shrinks linearly with time. However, the shrinking rate and the grain rotation are different. The rate of shrinking is much faster for large θ than small θ. And while there is no rotation in the large misorientation case, in the small misorientation case the center grain rotates to increasing θ as it shrinks.

Since there is no rotation in the classical grain boundary dynamics, the classical descrition is only valid for the large misorientation case. The dislocations are very close to each other when θ is large, which makes the grain boundary almost continuous. The authors argue that this makes it possible to describe the system with classical grain growth theory. When θ is small, the grain boundary is made up of individual dislocations. Their number is conserved, and they move radially to the center of the grain. The grain rotation in the small misorientation case is probably caused by coupling of the normal and the tangential motion of the grain boundary. In the Cahn-Taylor model [10], rotation towards increasing θ occurs in the coupling-only case, and it is only in this case that the number of dislocations is conserved.

While the dynamics of the bicrystals with large and small misorientation is different, in both cases the area of the grain shrinks linearly in time. This is not the case for grains with an intermediate misorientation, with θ between 5° and 15°. The grain growth of the bicrystal with a θ in this range is observed to alternately slow down and speed up. The grain also changes shape as it shrinks, alternating between a circular and a hexagonal shape.

In the intermediate range some of the dislocations are observed to move tangentially, and there is very little grain rotation. The tangential motion is dependent on the location and the Burgers vector of the dislocation. The dislocations therefore move at different velocities. Some of the dislocations are observed to move through other dislocations until they reach one they can react with. The different tangential motion of the dislocations changes the spacing between the dislocations. This affects the grain boundary motion, as a small spacing between dislocations make it possible for atoms to migrate through the grain boundary with diffusion. Parts of the grain boundary with small dislocation spacing move with a high velocity. When the dislocations are far apart, the grain boundary moves more slowly. This difference in velocity is assumed to cause the faceting-defaceting process observed in the article, as different parts of the grain boundary move at different velocities.

4.2.2 An MD study

Trautt and Mishin [20] examined grain growth and rotation of a two-grain system with molecular dynamics (MD) simulations. The results were compared with the

predictions made by the Cahn-Taylor model [10].

The model

The set-up is a crystal cylinder placed inside a larger crystal with a given grain misorientation θ. The measurements are made on a cross-section of the cylinder. The system is made of copper, which has a face-centered cubic (fcc) structure. In the 2D cross-section of the cylinder, a copper atom in the equilibrium position has four nearest neighbors. The results from this study are therefore not immediately comparable to the PFC study done by Wu and Voorhees [19] in 2D, where an atom in the equilibrium position has six nearest neighbors.

Grain growth and rotation

Because the time scale of the MD simulation is limited, the simulations only looked at relatively large misorientations ($\theta = 16°$, $28°$, $37°$ and $44°$). The grain growth at smaller misorientations was too slow to measure. The slow growth is presumed to be caused by the reduced driving force, as the grain boundary energy is smaller for a small misorientation angle. The grain growth was much slower for $\theta = 16°$ than for the other misorientation angles, whose growth velocity was almost the same. In all the simulations, the center grain shrinked until it disappeared.

Grain rotation was observed for low temperatures, up to $0.8T_m$, where T_m is the melting temperature. At $0.98T_m$ only the bicrystal with the lowest initial θ was observed to rotate. This was assumed to be because coupling disappears at high temperatures. This is because the coupling constant β is zero at high temperatures [20]. As there is also no rotation caused by sliding at high temperatures, there is a large resistance towards sliding in the system.

At $0.6T_m$ the rotation of the grains approached $\theta \approx 36°$, whether this required increasing or decreasing the misorientation angle. The authors suggest this is caused by the coupling constant β changing signs at this angle, due to the crystallography.

The dislocations are not constant in any of the simulations. This is asumed to be because there is some sliding present in all the simulations. It is assumed that the dislocations would be conserved with smaller θ, as the dislocations would then be farther apart.

Premelting

Premelting was also observed. With a temperature just beneath the melting point, high-angle grain boundaries can become liquid. On the other hand, low-angle grain boundaries can reach metastable states above the melting point. However, when a low-angle grain boundary with $\theta = 16°$ and a temperature

above the melting point rotates towards higher θ, the grain boundary, and then the rest of the center grain, melts. Whether the melted pocket is recrystallized or melts the rest of the crystal depends on whether the cylinder radius is smaller or larger than a critical radius. This critical radius changes with the temperature of the system.

Prohibited rotation

Grain rotation was prohibited by fixing the inner region of the center grain. With prohibited rotation the shrinking of the grains slowed down. In the absence of rotation, when $v_{\|} = 0$, shear stresses σ must counteract the rotation. With the condition $v_{\|} = 0$ put into the expression for $v_{\|}$ in eq. 4.20, an expression for σ can be found. It has been assumed that the volume free energy f_V is zero. Inserting the expression for σ into the equation for $v_{\mathbf{n}}$ in eq. 4.19, the following expresson is found,

$$v_{\mathbf{n}} = -\frac{dR}{dt} = \frac{MS\gamma}{R(\beta^2 M + S)} \tag{4.29}$$

where M, S, β and γ are assumed to be constants because the misorientation θ is constant. The growth is found to be,

$$R^2(t) = R_0^2 - \frac{2MS\gamma}{\beta^2 M + S}t \tag{4.30}$$

The area of the grain is predicted to grow linearly when the motion is coupled at low temperatures. When coupling disappears at high temperatures, $\beta = 0$ and $R^2(t) = R_0^2 - 2M\gamma t$. However, if S is small, the growth is approximately $R^2(t) \approx R_0^2 - 2S\gamma t/\beta^2$, which means that the shrinking rate is determined by the coupling constant S when sliding is difficult.

The simulation results seem linear for the high and low temperatures, but slightly curved for intermediate temperatures. The linear results for high temperatures argue that there is little or no coupling in this case. According to the theory, sliding towards minima of γ can occur in the absence of coupling. This was not observed, which implies that sliding is not present in this case. For lower temperatures, the absence of grain rotation was caused by additional sliding counteracting the coupling. The slow growth can be explained by the equation $R^2(t) \approx R_0^2 - 2S\gamma t/\beta^2$, which is valid when sliding is difficult. The growth is dependent on S instead of M in this case. When coupling disappears close to the melting point, the sliding also stops, and the grain growth with rotation prohibited begins to approach the free grain growth.

The fixed region was also used to apply a strain field by slowly rotating back and forth at a low temperature. This applied a shear stress on the grain boundary and caused an oscillatory displacement of it. When the misorientation angle was increased the grain shrank, and when it was decreased the grain grew.

The smaller rotation oscillations resulted in nearly reversible grain boundary oscillations, but with larger rotation amplitude the grain shrank more than it grew during a cycle. The reversible grain boundary oscillations suggested that the motion was coupled and the dislocations conserved. For the large rotation amplitude the dislocations were not conserved.

Mobility measurements

Grain boundary mobility M is defined as $v_{\mathbf{n}} = MP$, where $v_{\mathbf{n}}$ is the normal grain boundary motion and P is the driving force. With the definition $v_{\mathbf{n}} = -dR/dt$ and the classical driving force $P = \gamma/R$, the above relation becomes $-dR/dt = M\gamma/R$. The reduced mobility M^* is defined as

$$M^* = -\frac{1}{2}\frac{dR^2}{dt} \tag{4.31}$$

which is equal to $M\gamma$ from the former equation. This quantity was measured. Because it depends on misorientation, it was measured during a limited time period, to avoid rotation influencing the results. The results varied with temperature and initial misorientation. The reduced mobility increased with increasing temperature, and with increasing misorientation. However, the difference between $\theta = 16°$ and $\theta = 28°$ was much larger than between $\theta = 28°$, $37°$ and $44°$. When the temperature approached the melting point, the reduced mobility for the different misorientations approached the same value. For the larger initial misorientations, the mobility decreased a little before reaching the melting point. According to the article this could mean that the grain boundary energy decreased because it became a liquid.

From the assumption $M \approx M_d b/\theta$ for discrete dislocations, where M_d is the mobility of a dislocation and b is the magnitude of the Burgers vector, it would be expected that the mobility decreased with misorientation. Because the mobility increased with misorientation instead of decreasing, the number of dislocations is not conserved.

Dislocation reactions

When rotation decreases due to sliding, dislocation annihilation has to occur. If the coupled motion is not perfect, there is some sliding involved. The MD simulations showed that the number of dislocations was not conserved, meaning that dislocation reactions happened. As the number of dislocations decreased, the rotation caused by sliding was towards decreasing angles.

Because of the orientation of the Burgers vectors of the dislocations, they can not annihilate with their neighbors. Instead they have to travel to the other side of the cylinder cross-section in order to annihilate with a dislocation with an opposite Burgers vector. The paper suggests that this motion occurs by

dislocations dissociating and recombining with their neighbors. Each dislocation only has to travel a short distance, but it appears as if the first dislocation moves far.

4.3 Experimental paper on grain growth in sheared colloidal crystals

Gokhale et al. [22] look at grain boundary mobility experimentally. The experiments are performed on colloidal crystals. The goal of the experiments is to find how shear strain causes roughening and changes mobility, and whether it can cause directional grain growth. The effects of roughening on mobility was also studied by Holm and Foiles [3], who also look at the relation to stagnation. The article will be further studied in Section 4.6.1. The measurements were done on high-angle grain boundaries, as the dislocations in these boundaries are so close that the interface is continuous. The high-angle grain boundaries were chosen so that the misorientation angles between them were within a narrow range. The applied shear strain was oscillatory, $\varepsilon = \varepsilon_0 \sin(\omega t)$. The frequency of the oscillations was constant, while the amplitude ε_0 was changed.

The roughness of the boundary was characterized as the root-mean-square fluctuations of the interface. Strain was applied to the system, and the roughness of the grain boundaries was measured for the different strains. $\mathrm{GB}_{\parallel}$ is short for grain boundaries with a normal parallel to the applied strain, and $\mathrm{GB}_{\perp}$ is short for grain boundaries with a normal perpendicular to the applied strain. When the strain was increased, the roughness of $\mathrm{GB}_{\parallel}$ increased more than the roughness of $\mathrm{GB}_{\perp}$. The motion of $\mathrm{GB}_{\parallel}$ also changed from a step-like motion to a continuous motion as the strain was increased. This difference in motion between a rough and a smooth grain boundary was also discussed in the paper by Holm and Foiles [3]. The free energy of the interface is at a minimum for a smooth interface, but strain and thermal energy can cause grain boundary roughening.

The effect of grain boundary roughening on the grain boundary mobility M is investigated. The grain boundary velocity is defined as

$$v_{GB} = M\Gamma\kappa + M\sigma_{ext} \tag{4.32}$$

where Γ is the grain boundary stiffness, κ is the curvature, and σ_{ext} is applied stress. Because the strain is oscillatory the second term is expected to be zero. As the amplitude of the strain is increased it is found that Γ decreases more rapidly for $\mathrm{GB}_{\parallel}$ than $\mathrm{GB}_{\perp}$ while M increases more rapidly for $\mathrm{GB}_{\parallel}$ than $\mathrm{GB}_{\perp}$. The reduced mobility $M^* = M\Gamma$ determines if anisotropic grain growth occurs. It is found that $M^*_{\parallel} > M^*_{\perp}$ when ε_0 is large. This means that $v_{\parallel} > v_{\perp}$, and the grain growth is anisotropic when colloidal crystals are sheared.

On a microscopic scale, the grain boundary moves by single-atom hops across the boundary. The grain boundary mobility is affected by hops normal to the grain boundary. When the strain is increased, the displacements are observed to go from an isotropic distribution to an anisotropic distribution in the shear direction for both $GB_{\parallel}$ and $GB_{\perp}$. This has a more pronounced effect on $M_{\parallel}^{*}$ than $M_{\perp}^{*}$.

The paper finds that the strain does not affect the driving force of the grain boundaries, only the roughness. This is similar to the way temperature affects the grain boundaries in the paper by Holm and Foiles [3]. The kinetic roughening is anisotropic, causing anisotropic effective mobilities, velocity and directional grain growth.

4.4 Triple junctions

In a polycrystalline material, which is more complicated than the two-grain system studied in Section 4.1 and 4.2, there are triple junctions present. Triple junctions are junctions where three crystals meet. The presence of triple junctions affect the grain boundary dynamics, and in this section we will summarize a theoretical article [21] and PFC simulations of a three-grain system [19].

4.4.1 The dynamics of grain growth with triple junction drag

Gottstein and Shvindlerman [21] look at the effect of triple junctions on grain growth. Three different descriptions of triple junction dynamics are studied, the Von Neumann-Mullins relation, grain growth affected by triple junction drag, and grain growth controlled by triple junction kinetics.

The Von Neumann-Mullins model

The Von Neumann-Mullins model assumes that triple junctions have the same mobility as the grain boundaries, and that the angle of every triple junction is 120°. The rate of change of the grain area A is

$$\frac{dA}{dt} = -\oint V dl \tag{4.33}$$

where V is the grain boundary velocity and dl is an element of the perimeter of the grain. The grain growth is driven by curvature, as $V = M_b \sigma \kappa$. M_b is the grain boundary mobility, σ is the surface tension and $\kappa = d\phi/dl$ is the curvature. The rate of change is found to be

$$\frac{dA}{dt} = \frac{\pi M_b \sigma}{3}(n-6) \tag{4.34}$$

where n is the number of triple junctions. The rate of change is not dependent on the shape of the grain, only the amount of triple junctions. When $n < 6$ the grain will shrink, and when $n > 6$ the grain will grow.

Grain growth affected by triple junction drag

Because the grain boundary mobility M_b and the triple junction mobility M_{tj} are in fact different, the above equation is not accurate. In order to look at grain boundary motion affected by triple junction drag, a model with a single triple junction in a three-grain system is used. Two of the boundaries are curved. The two boundaries join with a plane grain boundary along the x-axis to form a triple junction. The curved boundaries are symmetric around the x-axis. The largest distance between the two curved grain boundaries is a. This system is representative for grains with $n < 6$. The normal grain boundary velocity v is related to the velocity V parallel to the x-axis like this, $v = V \cos\phi$, where ϕ is the tangential angle at any point along the grain boundary.

An expression for the shape $y(x)$ of one of the curved boundaries was found by using expressions for the velocity and the curvature κ to set up a differential equation and solving it for $y(x)$. The result was,

$$y(x) = \frac{a}{2\Theta} \arccos(e^{-2\Theta x/a + \ln(\sin\Theta)}) - \frac{a}{2\Theta}\left(\frac{\pi}{2} - \Theta\right) \tag{4.35}$$

where Θ is the contact angle of the triple junction.

With the driving force $\sigma(2\cos\Theta - 1)$ acting on the triple junction, the velocity of the triple junction is $V_{tj} = M_{tj}\sigma(2\cos\Theta - 1)$. The steady-state velocity of the system is $V = 2\Theta M_b \sigma/a$. With these velocities a relation between the mobilities and the angle Θ can be found,

$$\frac{2\Theta}{2\cos\Theta - 1} = \frac{M_{tj}a}{M_b} = \Lambda \tag{4.36}$$

Without triple junction drag $\Theta \to \pi/3$, which is the equilibrium angle. When the triple junction mobility is much smaller than the grain boundary mobility, $\Theta \to 0$. Θ is a function not only of the mobilities M_b and M_{tj}, but also of the grain size, with the parameter a included in the expression.

With the assumption that $n > 6$, the model has more triple junctions and curved grain boundaries. The x-axis of the system was placed between two triple junctions. The shape of the boundary between them was found to be

$$y(x) = -\frac{x_0}{\ln\sin\Theta} \arccos(e^{(x/x_0)\ln\sin\Theta}) \tag{4.37}$$

where x_0 is the length along the x-axis from the origin to the projection of the closest triple junction to the x-axis. The triple junction velocity is found to be

$V_{tj} = M_{tj}\sigma(1 - 2\cos\Theta)$ and the steady-state velocity of the boundary system is $V = -M_b\sigma \ln\sin\Theta/x_0$. This gives the relation

$$-\frac{\ln\sin\Theta}{1-2\cos\Theta} = \frac{M_{tj}x_0}{M_b} = \Lambda \tag{4.38}$$

When the grain growth is dragged by triple junctions in this instance Θ increases compared to the equilibrium value.

When the assumptions behind the Von Neumann-Mullins relation are no longer fulfilled, a new expression for the grain area's rate of change is needed. The velocity of a boundary affected by drag can be written like this, $V = M_b(\sigma\kappa - f/a)$, where a is the spacing between triple junctions and $f = V/M_{tj}$ is the dragging force. Rewriting this to give an expression for V and using the expression for dA/dt in eq. 4.33, results in this rate of change

$$\frac{dA}{dt} = -\frac{\sigma M_b}{1+1/\Lambda}[2\pi - n(\pi - 2\Theta)] \tag{4.39}$$

where Λ has different expressions for $n < 6$ and $n > 6$. When $n < 6$, Θ decreases. When $n > 6$, Θ increases. For both cases the grain growth slows down. As Θ is determined by the mobilities of both grain boundaries and triple junctions, in addition to the grain size, it is no longer possible to determine whether a grain will shrink or grow simply by the number of triple junctions.

Grain growth controlled by triple junction kinetics

It is also possible to predict the rate of change from the assumption that the grain growth is controlled by triple junctions. When this happens the polycrystalline material will coarsen to a polygonal shape, where the grain boundaries are straight lines and the curvature approaches zero. The structure can still change in time, and if $n = 3$ the grain growth becomes unstable. Shrinking grains whose motion is determined by grain boundary mobility eventually reaches a size where triple junction kinetics determine the growth.

The rate of change is $dA/dt = -vP$, where v is the normal velocity of the boundary and P is the perimeter. As all the grain boundaries are plane between the junctions, the motion is not driven by curvature, but determined by the triple junction velocity that was derived previously. Expressing v in the terms of the triple junction velocity gives $v = M_{tj}\sigma[2\sin(\pi/n) - 1]\cos(\pi/n)$, when $\Theta = \pi(n-2)/2n$. The rate of change for triple junction kinetics becomes

$$\frac{dA}{dt} = -M_{tj}\sigma\left[2\sin\left(\frac{\pi}{n}\right) - 1\right]\cos\left(\frac{\pi}{n}\right)P \tag{4.40}$$

Summary of the three triple junction dynamics

The different assumptions give different growth dynamics. The Von Neumann-Mullins relation gives a size-independent grain growth, where all the angles at the triple junctions are the same equilibrium value. The number of triple junctions decide whether or not the grain grows or shrinks. The grain boundary dynamics with triple junction drag gives triple junction angles Θ that deviate from the equilibrium value. It decreases when $n < 6$, and increases when $n > 6$. Θ is determined by the mobilities and the grain size. Because the rate of change depends on Θ, it is no longer just n that decides whether a grain shrinks or grows. For triple junction kinetics the rate of change is dependent on the perimeter of the grain, in addition to n. When $n \to \infty$, the rate of change approaches the value $\lim_{n\to\infty} dA/dt = M_{tj}P\sigma$, whereas the Von Neumann-Mullins rate of change continues to increase.

4.4.2 A PFC study of a triple junction system

A three-grain system is examined by Wu and Voorhees [19] with the PFC model, in addition to the two-grain simulations summarized in Section 4.2.1. The three-grain system is initialized as a circular crystal embedded in a bicrystal matrix. The bicrystal matrix is divided by a planar grain boundary. The bicrystal matrix is symmetric along the planar grain boundary, with misorientation angles $\theta_1 = 5.2°$ and $\theta_2 = -5.2°$ for the upper and lower halves. The center grain has $\theta = 0°$. In the three-grain system, there are two triple junctions where the three different grains meet.

In the article it is shown that the center grain shrinks with negligible rotation. This is assumed to be due to the geometric constraints of the system, as the upper and lower part of the grain want to rotate in a clockwise and a counter-clockwise motion, respectively. Because the center grain wants to rotate in both directions, the rotation is negligible. As the center grain shrinks, the shape of the crystal changes from a circular shape to a lens-shape. The upper and lower grain boundary move faster than the triple junctions. The dislocations along the grain boundary of the center grain move vertically instead of radially, and the spacing of the dislocations remains constant. As the upper and lower grain boundary move toward each other, dislocation reactions occur in these junctions. Dislocations in the bicrystal grain boundary react alternately with dislocations from the upper and lower grain boundary of the central grain, creating a new dislocation. This continues until the system reaches equilibrium, when the center grain is gone and there is only the planar grain boundary of the bicrystal matrix left. The evolution of the system depends on the dislocation reactions at the triple junctions.

This is not the only way a three-grain system can behave. Depending on the misorientation of the grains, other dislocation reactions can occur. The misori-

entation angles decide what kind of Burgers vector the dislocations have, and the Burgers vector decides what kind of dislocation reactions that can happen. Under certain circumstances, the dislocations of the upper and lower grain boundary can only react with each other, and not the planar bicrystal grain boundary.

The end state of the system is not necessarily the bicrystal matrix with the planar grain boundary. A nonplanar grain boundary can be in a metastable equilibrium state if the elastic energy of the system is approximately equal to the grain boundary energy. If the driving force of the grain boundary energy is not large enough to reach the final equilibrium state, the state is metastable.

4.5 Summary of grain growth theory

4.5.1 Comparing the simulations to the Cahn-Taylor model

The two-grain system described by the Cahn-Taylor model [10] detailed in Section 4.1.2 has been simulated using the PFC model by Wu and Voorhees [19] and using molecular dynamics (MD) by Trautt and Mishin [20]. However, there are some differences between them that make it hard to compare the two. The PFC study is in 2D, and the MD study is in 3D, even though the measurements are made on a 2D cross-section. The crystal structure of the systems are also different. The MD simulation has an fcc (face-centered cubic) crystal structure, and the PFC simulation has a 2D hexagonal crystal structure. In 2D, this means that the MD simulations have four nearest neighbors, while the PFC simulations have six nearest neighbors. This changes the type of dislocation it is possible to have, and the Burgers vectors of these. In addition, the MD simulations are performed with physical parameters. Due to the definition of the PFC model, the PFC simulations are performed with dimensionless quantities.

While the MD simulations are performed at many different temperatures, the PFC simulations have used one temperature near the melting point. And while the PFC simulations study misorientation angles between 5° and 15°, the MD simulations only look at $\theta > 16°$, because the time scale of shrinking for the smaller θ are too long for the MD simulations. With different crystallography, these angles can not be readily compared.

Both the PFC and the MD studies test predictions made by the Cahn-Taylor model. Rotation of the center grain means that either sliding, coupling or both is present in the system. The direction of the rotation can indicate which mechanism dominates. Sliding is a mechanism that is driven by a decrease in the grain boundary energy $\gamma(\theta)$ or an applied stress σ. The decrease in γ is accomplished by rotating to smaller θ or to a local minimum in γ. Coupling is driven by a decrease in the total grain boundary energy $\int \gamma dA$. For small θ the rotation goes to increasing values of θ. This is possible if the area is reduced quickly enough that $\int \gamma dA$ still decreases.

A good test for the coupling-only case is whether or not there is dislocation conservation. This only occurs in the coupling-only case. The PFC simulation with $\theta = 5°$ has dislocation conservation, and is therefore an example of the coupling-only case. In the MD simulations on the other hand, dislocations are annihilated, which means that there is at least some sliding present.

Coupling is expected to disappear close to the melting point [20]. In the MD simulations, all rotation disappears at high temperatures, at least for $\theta \geq 28°$. That means that there is also no sliding present in this case, which means that coupling is the most dominant mechanism in this system. There is some rotation when $\theta = 16°$. The PFC study observes rotation for the smallest θ, but not for the larger θ at high temperatures. The results from the two different methods do not disagree.

The absence of rotation can mean that there is no coupling or sliding, as is assumed in the MD case for high temperatures. It can also mean that the mechanisms counteract each other. In the case of prohibited rotation, it is assumed that the amount of sliding in the system is incresed to counteract the coupling. This assumption is supported by the center grain shrinking more slowly, because the sliding coefficent S determines the growth when S is small. This also supports the assumption that sliding is more difficult than coupling in this system.

The nonlinear growth of the intermediate misorientation in the PFC simulations is probably caused by the dislocation motion. The rotation is small, but present, which means that the center grain is not free of coupling and sliding. As the grain boundary in this case is neither completely continuous or completely composed of discrete dislocations, the theory is difficult to apply.

4.5.2 Dislocation reactions and grain boundary motion

The two studies observe different dislocation dynamics, and in the PFC study the dislocation motion is very different for the different misorientations. In the large misorientation case, the PFC study can not observe individual dislocations. Instead, the grain boundary is continuous. In the small misorientation case, the dislocations are conserved and move radially to the center of the grain. There are no dislocation reactions until the center grain is so small, that the dislocations have to interact with each other.

The behavior at the intermediate misorientation case is different. The area does not shrink linearly in time and the dislocations are observed to move tangentially along the grain boundary. The tangential motion of the individual dislocation depends on its type and position, which means that some dislocations have a higher tangential velocity than others. This results in some parts of the grain boundary having dislocations more closely clustered than other parts. The spacing between dislocations affects the normal motion of the grain boundaries. The parts of the grain boundary with closely clustered dislocations move faster

than others. In this case there are also dislocation reactions. Dislocations travel along the grain boundary, passing through other dislocations, until they reach one they can react with and form a new dislocation.

In the MD study dislocations are annihilated. This means that they must be able to travel, because they can only annihilate with a dislocation from the other side of the grain. The dislocations are observed to move by dissociating and reforming with their neighbors, so that every dislocation only moves a short distance. In the PFC simulations, dislocations with high velocity were observed to pass through dislocations with lower velocity. This might be a different interpretation of the mechanism described for the MD simulations. Annihilation does not seem to have been observed in the PFC simulation, at least not until the end of the simulation, when the center grain disappears. This difference in dislocation reactions could be caused by the difference in crystallography.

Tangential motion is only observed in the intermediate misorientation case in the PFC simulations. However, the tangential motion of each dislocation in the MD simulations is very small, and the authors believe that if the spacing between the dislocations had been smaller, there would be no reactions. The large misorientations causes the small spacing between the dislocations. The reason individual dislocations can be observed in these high-angle grain boundaries are in part due to the crystallography of the system. When $\theta = 15°$ in the PFC simulations, the grain boundary was perceived as continuous, even though the MD simulations can measure dislocations for higher θ. It is also possible that the exact position of the atoms in the MD simulations make the dislocations easier to measure.

The grain boundary motion is different in the MD and PFC simulations. In the PFC study the dislocations are observed to move by glide and climb, while in the MD study they move only by glide. Wu and Voorhees [19] claim that the high temperature allows for dislocation climb. This also makes it possible for the center grain to keep its circular shape, so that the area of the grain boundary is at a minimum. The MD simulations are also performed at high temperatures, but there is no sign of dislocation climb.

The experiment on colloidal crystals [22] summarized in Section 4.3 does not examine the Cahn-Taylor model. Instead it looks at the motion of grain boundaries on an atomic level. The grain boundaries in this experiment are continuous, as all the measurements are made on high-angle grain boundaries, but they have a varying degree of roughness. The paper looks at how strain changes the roughness, and how the roughness changes the mobility. The main result is that directional strain causes directional grain growth. The smooth grain boundaries move slowly while the more rough or uneven grain boundaries move faster. The motion is also different, as the smooth boundaries move in a step-like manner, while the rough boundaries move evenly.

4.5.3 The triple junction system

The dynamics of a polycrystalline system is more complicated than a two-grain system, in part because there are triple junctions present. Triple junctions are not included in the Cahn-Taylor model [10], but they change the dynamics significantly. Gottstein and Shvindlerman [21] derived a theoretical framework for triple junctions, which was summarized in Section 4.4.1. Wu and Voorhees [19] performed a PFC simulation of a system with two triple junctions, which was summarized in Section 4.4.2.

The triple junction theory can be divided into three cases: the classical description, the dynamics affected by triple junctions drag, and triple junction kinetics, where the triple junction mobility is the mobility of the whole system. In addition to these three cases, the number of triple junctions in a grain is important to the dynamics. In the classical theory the difference between a grain growing or shrinking is at $n = 6$, where n is the number of triple junctions. For the other theories the partition is less strict, as there are other parameters also influencing the growth. The classical theory is not correct in practice, so the two others are the most interesting. They should be simple to differentiate, as the grain boundaries in the system affected by drag are curved, while in the system governed by triple junction kinetics, the grain boundaries are plane. It is aso suggested that triple junction kinetics takes over when the grain is small.

The system in the PFC simulations is an ideal three-grain system. It covers only a small part of the theory of triple junction drag, as there are only two triple junction kinetics. As expected by the theory, since there are only two triple junctions, the center grain shrinks. The triple junctions move more slowly than the grain boundaries, as expected. It looks like the dynamics are simply dragged by the triple junctions, but it is difficult to know for sure, as there are only two triple junctions. The grain boundaries can not be straight without the triple junctions disappearing. In the simulations they were also observed to act as sinks for the dislocations in the curved grain boundaries. Comparing this to the Cahn-Taylor model, as there was no rotation in the system the spacing between the dislocations must be constant. This was only made possible by the dislocations reacting at the triple junctions. Presumably, this system has enough similarities to the Cahn-Taylor model, with the circular center grain, that the comparison is possible.

4.6 Stagnation of grain growth

The equilibrium state of a polycrystalline material is a single crystal. When grain growth stops before this state is reached, we have stagnation. There are different explanations for this behavior. The system could have reached a metastable state, where the grain boundary energy is zero, as derived by Li et al. [2]. Or the

grain boundary mobility could affect the dynamics, as discussed by Holm and Foiles [3].

4.6.1 Stagnation in pure materials

Holm and Foiles [3] investigate the possibility of grain boundary mobility as the cause of grain growth stagnation. Different simulation methods are used. Stagnation is often connected to solute drag, but as stagnation also occurs in pure materials, another explanantion is needed.

The mobility of the grain boundary tells us how fast the grain boundary can move. According to the article the mobility can be divided into high- and low-mobility boundaries. The high-mobility boundaries are rough at an atomic level, and the motion of the boundary is continuous. The low-mobility boundaries are smooth, and the motion is stepwise. A boundary can change from one type to the other at a characteristic temperature T_r, which is different from boundary to boundary. With increasing temperature, the grain boundaries change from smooth, low-mobility to rough, high-mobility boundaries. This process is called roughening. Gohhale et al. [22] found that roughening can also be caused by straining the system.

Holm and Foiles [3] find that when all the boundaries are high-mobility, there is no stagnation. The polycrystalline material coarsens until all the different grains in the system have grown into one grain. When low-mobility boundaries are included, the mean grain size increases until it suddenly slows down at a finite grain size. Simulations are made with different numbers of low-mobility boundaries included. When the fraction of low-mobility grain boundaries f_0 increases, the finite grain size decreases.

Some time after the growth slows down, the system stagnates. As f_0 increases, the stagnant grain size decreases. The system stagnates earlier in the coarsening process when f_0 is large. Relating this to how f_0 increases with decreasing temperature, shows that the stagnant grain size decreases with decreasing temperature.

The article concludes that smooth-boundary pinning is a mechanism that can explain stagnation, also in high-purity materials. The results suggest that stagnation does not demand that all the boundaries are low-mobility.

4.6.2 Stagnation in nanocrystalline materials

Li et al. [2] look at stagnation of grain growth in nanocrystalline materials with solute segregation. The paper argues that stagnation is caused by the decrease of grain boundary energy, not the solute drag force as previously believed. Two

well-known models in this field, Burke's model,

$$\frac{dD}{dt} = \alpha M \gamma_0 \left(\frac{1}{D} - \frac{1}{D_{\max}} \right) \tag{4.41}$$

and the model proposed by Michels et al., modified from Burke's model,

$$\frac{dD}{dt} = \alpha M \gamma_0 \left(\frac{1}{D} - \frac{D}{D_{\max}^2} \right) \tag{4.42}$$

describe the evolution of the mean grain diameter D in time t. M is the grain boundary mobility, γ_0 is the grain boundary energy, and α is a constant of proportionality. $D_{\max}$ is the maximum grain size after the stagnation. In both of the above equations the last terms are the drag force terms that slow down the growth, and cause stagnation. Because these terms are velocity independent, it is argued that they cannot be interpreted as the solute drag force, as the solute drag force is proportional to the grain boundary velocity.

The authors of the paper instead find inspiration from the thermodynamic strategy, by decreasing the grain boundary energy. When the grain boundary energy is zero, a metastable equilibrium with a grain size $D_{\max}$ can be reached. The grain boundary energy can be written as follows when incorporating the solute segregation,

$$\gamma = \gamma_0 - \Gamma(\Delta H_{\text{seg}} + \bar{R}T \ln X_g) \tag{4.43}$$

where γ_0 is the grain boundary energy for the pure solvent, X_g is the bulk concentration, ΔH_{seg} is the enthalpy of segregation, $\bar{R}$ is the ideal gas constant and Γ is the solute excess at the grain boundary. The grain boundary energy is reduced by the solute segregation.

The final grain size $D_{\max}$ can be found by assuming that in the final state the grain boundary is saturated with solute atoms. This assumption gives the relation

$$X_{\text{total}} = \frac{3\Gamma V_M}{D} + X_g \tag{4.44}$$

where V_m is the molar volume of the ally. This has previously been found to give the relation,

$$\gamma_0 = \Gamma_0 \left[\bar{R}T \ln \left(X_{\text{total}} - \frac{3\Gamma_0 V_M}{D_{\max}} \right) - H_{\text{seg}} \right] \tag{4.45}$$

which can be used to find $D_{\max}$.

The expression for the grain boundary energy is put into the ideal grain growth law,

$$\frac{dD}{dt} = \alpha M \left[\gamma_0 - \Gamma(\Delta H_{\text{seg}} + \bar{R}T \ln X_g) \right] \frac{1}{D} \tag{4.46}$$

Then Γ is assumed to be either proportional to D, which can be supported by rearranging the terms in eq. 4.44, or Γ is assumed to be proportional to D^2. The

first assumption results in the Burke model, and the second assumption results in the Michel model.

The article concludes that the drag forces responsible for the stagnation of grain growth can be caused by decrease in grain boundary energy due to solute segregation. Both the grain boundary energy and mobility are affected by the solute segregation.

4.6.3 A PFC study of grain growth rotation and stagnation

Bjerre et al. [4] study a 2D polycrystalline material with the PFC model. The expression for the free energy in the model is slightly different than the one used in this thesis, it uses some different constants and it has an additional term. The free energy is formulated as follows,

$$\mathcal{F}[\psi;T] = \int d\mathbf{r} \left[\frac{1}{2}\psi(\nabla^2+1)^2\psi - \frac{\epsilon}{2}\psi^2 - \frac{1}{6}\psi^3 + \frac{1}{12}\psi^4\right] \tag{4.47}$$

In order to model a polycrystalline material, crystal seeds are randomly placed in the simulation space. Results are obtained for different temperatures according to two protocols for ψ_0. One protocol places the parameter sets for the simulations inside the solid phase, with the same ψ_0 value for all the simulations, and the other protocol places the parameter sets along the line between the solid and the solid-liquid coexistence phase.

The classical theory predicts that the grain grows linearly, $\langle A\rangle \sim t$. In experiments the grain growth has been found to behave like a power-law in time, $\langle A\rangle \sim t^{\alpha}$, but there is no unified theory to determine the scaling exponent α.

In the simulations, the coarsening dynamics of the systems close to the melting point are found to act like a power-law in time. The scaling exponent depends on the quenching depth. Close to the melting point $\alpha \approx 1/2$, and for slightly lower temperatures it approaches $\alpha \approx 1/4$. For even lower temperatures stagnation sets in very quickly. The coarsening is also affected by grain rotation, which is found to decrease as the mean grain size increases. Small grains rotate more than larger grains. The rotation decreases most rapidly for low temperatures, as the grain growth also stagnates.

Stagnation is observed at low temperatures. The average grain size in the stagnated state was measured, and found to increase with increasing temperature, especially when approaching the melting point. For intermediate quenching depths, measurements from the coexistence line have slightly larger mean grain size in the stagnated states.

A relation was found between the grain growth and the rotation rate,

$$\left|\frac{\Delta\theta}{\Delta A}\right| \sim A^{-\nu} \tag{4.48}$$

where $\nu \approx 1.25$. This result was found for $\epsilon = -0.03$. If the grain rotation is caused by pure coupling, the tangential velocity can be expressed, $v_{\parallel} = Rd\theta/dt = \beta v_n$. The dislocation conservation in the coupling-only case results in the condition $R(t)\theta(t) = \text{const}$, which can also be expressed, $\theta(t) \sim A^{-1/2}(t)$. With these assumptions, the constant in the above equation is given as $\nu = 3/2$. This prediction is slightly different from the simulation results. It is assumed that the complicated structure of a polycrystalline material allows for sliding, dislocation reactions and possibly premeltings, which can explain the difference in the predicted and measured value of ν.

The article finds a power-law dependent growth for higher temperatures, and a grain growth stagnation for lower temperatures. It also finds a relation between grain growth rate and rotation rate.

4.6.4 Summary of stagnation theory

It is known that coarsening does not always result in the equilibrium state i.e., a single crystal. When the system reaches a metastable state that is not the equilibrium state grain growth stagnation occurs. This can be observed in many systems. Different explanatory models have been suggested to address this issue and some of them have been described in this section.

Grain growth stagnation in nanocrystalline materials with solute segregation has often been related to solute drag force, but as derived by Li et al. [2] and summarized in Section 4.6.2, it may be more accurate to state that stagnation is caused by decreased grain boundary energy. This assumption can lead to two known dynamic equations describing grain growth with drag terms.

A proposed mechanism that can cause stagnation is the low-mobility grain boundaries described by Holm and Foiles [3] and summarized in Section 4.6.1. According to this study, all the grain boundaries do not have to be low-mobility in order to cause stagnation. It is enough that a given amount of grain boundaries are low-mobility. The low-mobility grain boundaries are characterized by being smooth and moving in a step-like motion. The high-mobility grain boundaries are roughened and move continuously. A low-mobility boundary can become a high-mobility boundary by a roughening process caused by increasing temperature until it reaches a characteristic temperature T_r. Therefore stagnation is more likely to occur at low temperatures. In Section 4.3 an experiment performed by Gokhale et al. [22] on grain boundaries is summarized. It shows that shear strain can also cause a roughening process, but the effect is most pronounced on grain boundaries with normal n parallel to the shear. Stagnation is therefore most likely to happen in systems with low temperature and little applied strain.

Simulations of a polycrystalline material, performed by Bjerre et al. [4] and described in Section 4.6.3, shows that stagnation sets in at high quenching rates. The simulations are performed using the PFC model. The results show that the

stagnation sets in more rapidly at low temperatures. The size of the average stagnated grain increases closer to the melting point. This is consistent with the results from Holm and Foiles [3]. The size of the stagnant grain is affected by the parameters' location in the phase diagram. The mean grain size is allowed to grow slightly larger when the system is placed at the line between the solid phase and the coexistence phase. In the solid phase, the stagnation sets in earlier in the coarsening process. The difference is most pronounced close to the melting point. At lower temperatures the stagnant grain size approaches the same value.

In Chapter 5 we will present our results from 2D PFC simulations. From this brief overview of stagnation theory, we would expect to find stagnation as a result of low-mobility grain boundaries at deep quenches. We did not include strain in our systems, and as there can be no solute segregation in our standard PFC model, the grain boundary energy can not be affected by this.

Chapter 5

Simulation results for the 2D bicrystal

In Chapter 4 we examined grain growth theory. In order to test some of the predictions that were made, we use the PFC equation to simulate 2D systems resembling the two-grain system discussed in the section on the Cahn-Taylor model [10], Section 4.1.2. The two-grain system is also called a bicrystal. We examine systems with the same misorientation angles that were used in the previous PFC simulations by Wu and Voorhees [19] that were described in Section 4.2.1.

5.1 The set-up

A bicrystal was initialized in 2D as a circular crystal embedded in a larger crystal with a different crystal orientation. The crystal structure was hexagonal. The system was initialized according to the one-mode approximation to the ψ-field of the equilibrium crystal, described in Section 3.2. The two crystals were both implemented as equilibrium crystals, but the one in the center was rotated a given angle. This angle is the misorientation angle θ between the two grains. A rotation matrix was multiplied with the basis vectors $\mathbf{k}_j$ in the one-mode approximation, in order to rotate the center grain. The rotation brought the system out of equilibrium.

The center grain was implemented as a perfect circle in the middle of the simulation box, disregarding the position of the atoms. The interface between the crystals was very sharp. In the beginning of the simulation the grain boundary formed, and the positions of the dislocations were determined. This is the beginning of the coarsening process when initializing the system as we have done. It is possible to initialize the system like this because in the PFC model the atoms are not uniquely defined, unlike in for instance molecular dynamics simulations. The PFC equation was solved with the spectral method [17, 18], which is explained in

the Appendix. In most of this chapter we have used the parabolic PFC equation,

$$\frac{\partial \psi}{\partial t} = \nabla^2[(-\epsilon + (1+\nabla^2)^2)\psi + \psi^3] \tag{5.1}$$

We have also used the hyperbolic PFC equation in order to compare some of our results from the parabolic model to a different PFC model,

$$\tau\frac{\partial^2 \psi}{\partial t^2} + \frac{\partial \psi}{\partial t} = \nabla^2[(-\epsilon + (1+\nabla^2)^2)\psi + \psi^3] \tag{5.2}$$

The constant τ is the flux relaxation time. In these expressions we have taken the functional derivative $\delta\mathcal{F}/\delta\psi$ of the free energy.

The parabolic PFC equation has been used in most of the following sections, while the hyperbolic equation has been used in Section 5.7 and 5.8.

The boundary conditions are periodic. This results in the outer crystal being essentially infinite. In order to avoid strain along the edges of the simulation "box", the system size is chosen with care, so that the crystal is periodic over the edges. Additional strain in the system can affect the dynamics of the bicrystal. In order to implement the crystal correctly, we used the method mentioned in the article by Mellenthin et al. [23], where the basis vectors of the hexagonal pattern are used to calculate the repeating patterns in the crystal. The general method can be used for any crystal orientation. We were able to simplify the method, as the outer crystal in our simulations has not been rotated. In the implementations in this chapter the system size is therefore chosen to have a grid 502×502 and spatial resolution $\Delta x = \Delta y = 1.0$. This is one of the possible grid sizes when we want a simulation "box" with equal sides and equal grid spacing. There are approximately 4500 atoms in the system, and approximately 560 atoms in the center grain at the beginning of the simulation.

An example of the evolution of the bicrystal can be seen in Figure 5.1, where the center grain is being absorbed by the infinite, outer grain. The grain boundary is found at the break in periodicity. The atoms in this area are not as clearly defined as in the two grains.

In order to find appropriate values of undercooling ϵ and mean order parameter ψ_0 for the simulations, we use the phase diagram in Figure 3.1. The values are chosen from the edge between the triangular phase and the solid-liquid coexistence phase. The parameter sets we have used in the simulations can be seen in the following table.

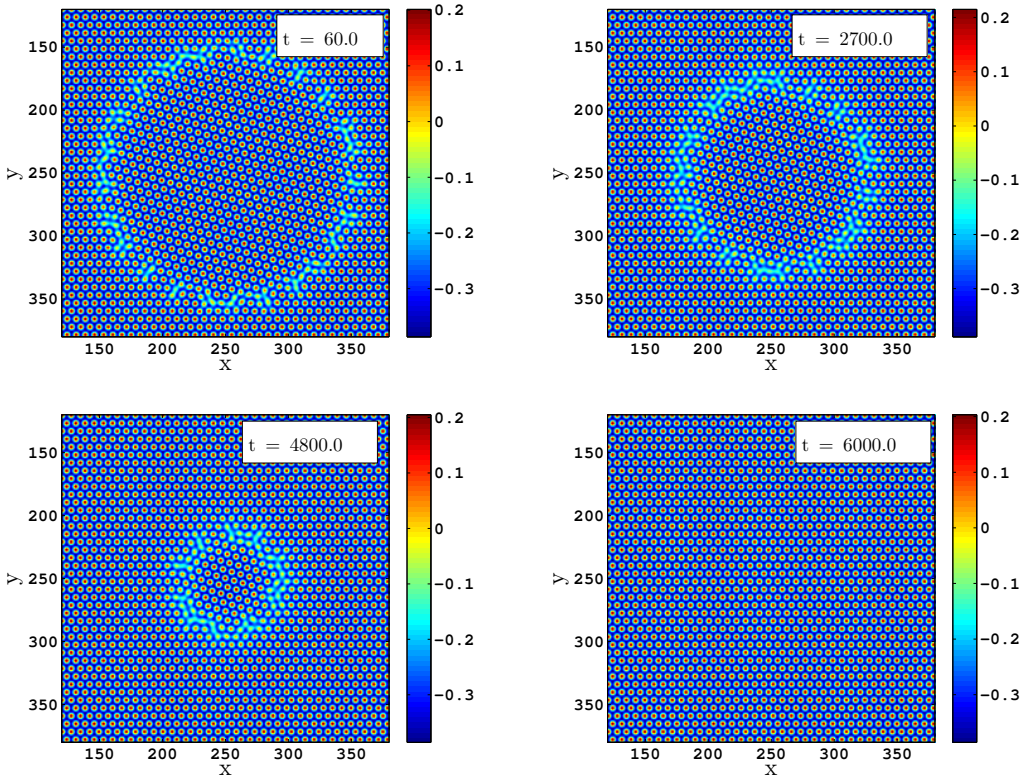

Figure 5.1: A bicrystal with a misorientation angle $\theta = \pi/12 = 15°$ at four different times. The parameters of the simulation are $(\epsilon, \psi_0) = (0.1, -0.195)$. The atoms are located at the maxima. The grain boundary can be found at the break in periodicity. The edges of the simulation "box" have been cropped.

ϵ	ψ_0
0.1	-0.195
0.15	-0.23
0.2	-0.27
0.25	-0.29
0.27	-0.295
0.28	-0.30
0.29	-0.305
0.3	-0.31
0.32	-0.32
0.35	-0.33
0.4	-0.34
0.5	-0.37

The first parameter set is the same as the one that was used in the PFC simulations [19] summarized in Section 4.2.1. This was chosen in order to make it easier to compare the results. In the simulations we used $\Delta x = 1.0$ and $\Delta t = 0.06$ for the smallest ϵ-values. As we began to use higher values of ϵ we had to use smaller values of Δt. The amplitude of the ψ-field increased with ϵ and the ψ-field became sharper. In order to avoid that the system collapsed, we needed to use a higher time resolution for these parameters.

We performed simulations on three different misorientation angles. We used the relatively large misorientation $\theta = 15°$, the intermediate misorientation $\theta = 10°$ and the small misorientation $\theta = 5°$. These are the same misorientations that were used by Wu and Voorhees [19]. We wanted to see what effect the misorientation and the quenching rate had on grain growth.

5.2 The Voronoi diagram

In order to find the dislocations and the grain boundary, a Voronoi diagram was used. In order to use the Voronoi diagram, the position of each atom had to be determined. Because we use negative values for the mean order parameter ψ_0 in the simulations, the atoms are located at the maxima of ψ. An atom is interpreted as a peak with a maximum value larger than a given threshold. The threshold was chosen to be at $\psi_{\text{thresh}} = 0.5A + \psi_0$, where the amplitude A is defined as $A = \psi_{\max} - \psi_0$, and $\psi_{\max}$ is the maximum value of the order parameter while ψ_0 is the mean value. The ψ-field was then turned into a binary image with all ψ-values above the threshold given one value, and all the values below the threshold given another value. The atom was then located at the center of mass of each cluster with ψ-values above the threshold.

When the positions of the atoms are known, a Voronoi diagram can be made of the system. The Voronoi diagram finds the nearest neighbors of each atom

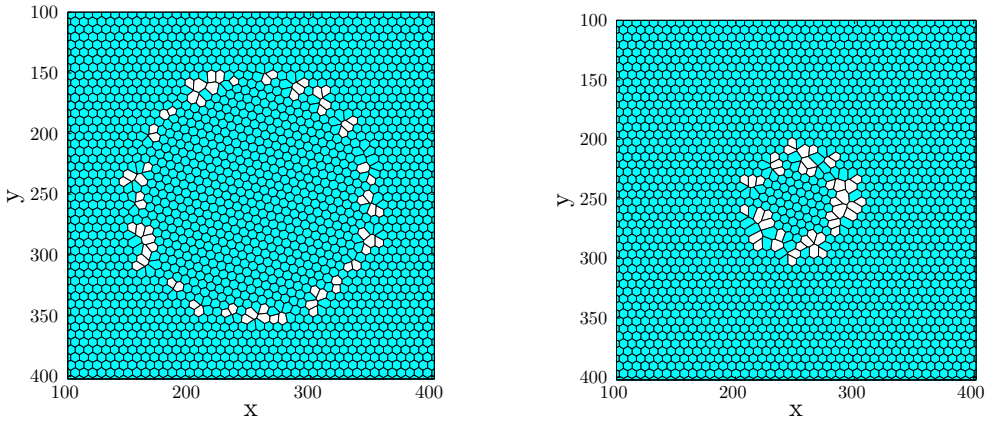

(a) $t = 60$ **(b)** $t = 4800$

Figure 5.2: The Voronoi diagram corresponding to Figure 5.1 for $t = 60$ and $t = 4800$. The simulation parameters are $(\epsilon, \psi_0) = (0.1, -0.195)$ and $\theta = 15°$. The edges have been cropped. The atoms with six neighbors are colored light blue and the atoms with a different number of neighbors are colored white.

by drawing a straight line between the atom and the surrounding atoms. Then a normal is drawn at the midpoint of each line. The normal continues until it intersects with another normal. If the atom has six neighbors, the normal lines form a hexagon. This is the pattern of the equilibrium crystal, when the free energy is at a minimum. The Voronoi diagram can not be used at the edges of the system, but since the grain boundary is not at the edge, this is not a problem.

The number of vertices is the same as the number of neighbors. Dislocations are found where an atom has a different number of neighbors than six. A typical dislocation configuration is a pair of atoms with five and seven neighbors. Two of the Voronoi diagrams corresponding to the bicrystal evolution in Figure 5.1 can be seen in Figure 5.2. The dislocations in this case are more disordered than the pair configuration mentioned above.

The grain boundaries for the different misorientations $\theta = 5°$, $10°$ and $15°$ look very different. When $\theta = 15°$, the dislocations are very close together and the grain boundary is almost continuous. When $\theta = 5°$, the individual dislocations are identifiable. The Voronoi diagrams for $(\epsilon, \psi_0) = (0.3, -0.31)$ for the three different misorientations can be seen in Figure 5.3. The time is $t = 3000$ in all the simulations. The dislocations are more clearly defined in these images, even for the large misorientation. They also form dislocation pairs of five and seven atoms. This suggests that our dislocation analysis using Voronoi diagrams is more accurate at larger ϵ-values.

Because the grain boundary in the bicrystal is circular, there is a straightforward way to calculate the crystal growth. If we know the position of each

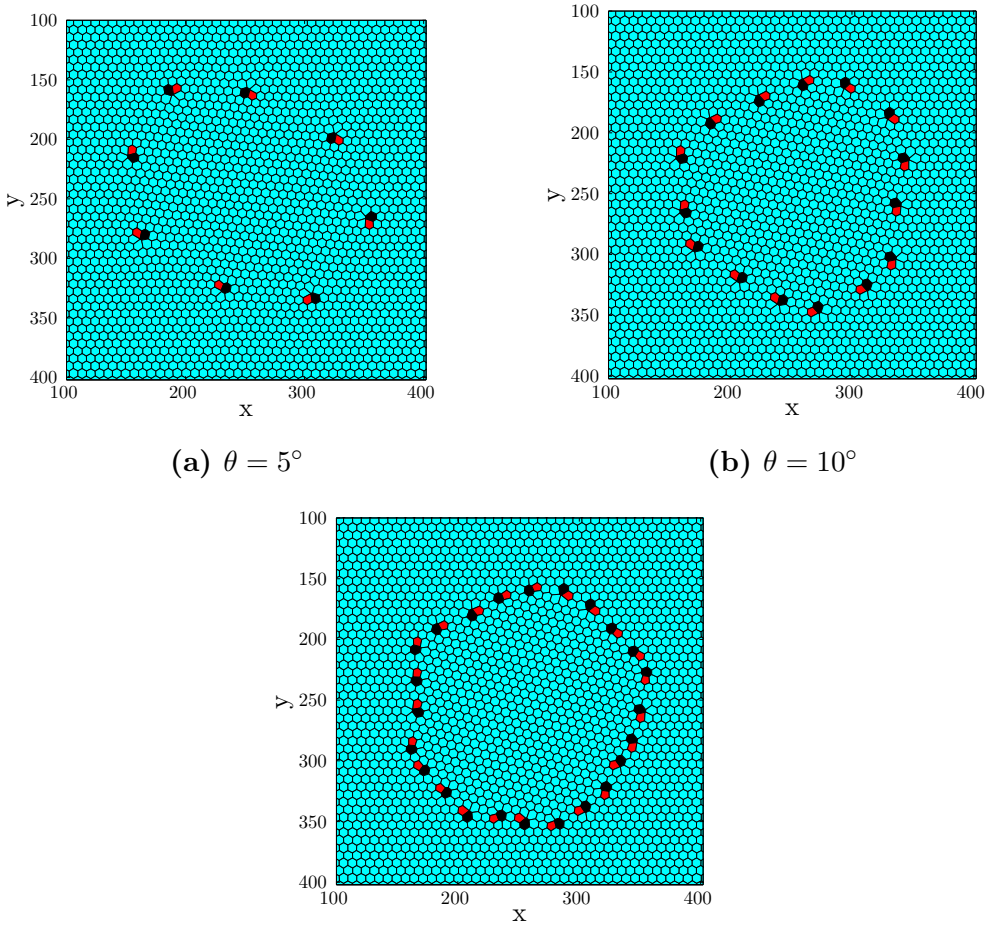

(a) $\theta = 5°$ **(b)** $\theta = 10°$

(c) $\theta = 15°$

Figure 5.3: Voronoi diagrams for three different misorientations. The figures show the center of the system. The parameters are $(\epsilon, \psi_0) = (0.3, -0.31)$ and $t = 3000$ for all the simulations. The atoms with six neighbors are colored light blue, the atoms with seven neighbors are colored black, and the atoms with five neighbors are colored red.

dislocation we know where the grain boundary is. The radius of the center grain was found by measuring the distance between each dislocation and the center of the system. Then the mean radius R was found, along with the standard deviation σ_R of the measurements. In order to measure how fast the center grain shrank we used the value R^2, which is proportional to the area. The error $\sigma_{R^2} = 2R\sigma_R$ was calculated with the approach from Squires' textbook [24].

5.3 Large misorientation

In this section and in Section 5.4 and 5.5 we will show our results from bicrystal simulations with different misorientation angles. In this section we look at results from bicrystal simulations with a relatively large misorientation, $\theta = 15°$. We ran simulations with parameter sets from the table in Section 5.1. The Voronoi diagram was used to track the position of dislocations in time.

The ψ-field evolution for $(\epsilon, \psi_0) = (0.1, -0.195)$ with this misorientation can be seen in Figure 5.1, and Figure 5.2 shows two Voronoi diagrams from the same simulation. The center grain shrinks while seemingly keeping its circular shape. The ψ-field shows the grain boundary to be almost continuous. In the Voronoi diagram the grain boundary can also be easily identified, but the dislocations are placed unevenly along it. Some of the atoms with six neighbors in the vicinity of the grain boundary have slightly skewed hexagonal shapes.

The Voronoi diagram when $(\epsilon, \psi_0) = (0.3, -0.31)$ in Figure 5.3c looks different. In this case the grain boundary is clearly made up of dislocation pairs with five and seven neighbors. The grain boundary is almost continuous also in this case. The atoms and dislocations seem to be more clearly defined for the larger ϵ-value.

The number of dislocations as a function of time can be seen in Figure 5.4a. The plot shows a selection of the simulations we ran. In the legend only the undercooling ϵ is stated. The corresponding ψ_0-value can be read from the table in Section 5.1. For the lowest values, when $\epsilon = 0.1$ and $\epsilon = 0.2$, the number of dislocations fluctuates before it drops to zero. When there are no more dislocations, the center grain has disappeared. However, when ϵ increases, the fluctuations decrease and when ϵ is larger than $\epsilon = 0.2$, the dislocations do not drop to zero. The fluctuations for the small ϵ-values support the indication from the Voronoi diagrams in Figure 5.2 and 5.3c that a larger ϵ-value leads to more well-defined dislocations. It is also interesting to see that for the larger ϵ-values the number of dislocations are the same. The misorientation seems to determine the number of dislocations.

The square of the radius of the center grain as a function of time can be seen in Figure 5.4b. The center grain shrinks faster for lower ϵ-value, when the temperature is closer to the melting point. As was seen in the dislocation plot, the systems with $\epsilon = 0.1$ and $\epsilon = 0.2$ reach the equilibrium state of the single crystal.

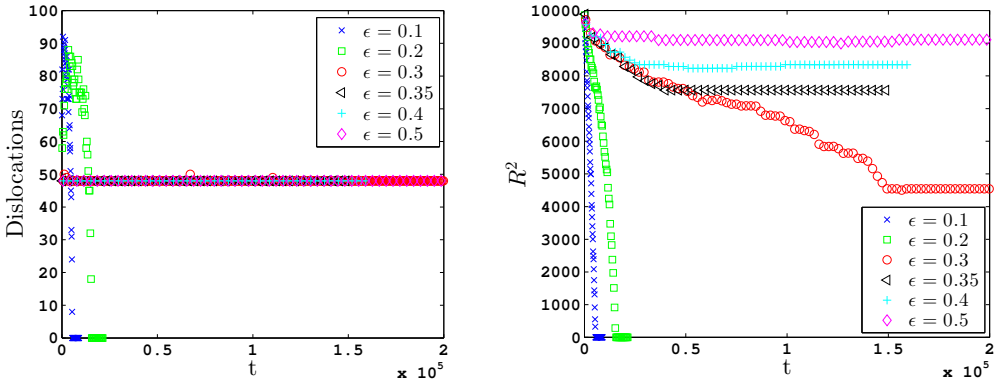

(a) Dislocations as a function of time **(b)** R^2 as a function of time

Figure 5.4: (a) The number of dislocations as a function of time when the misorientation $\theta = 15°$. (b) The square of the radius of the embedded crystal as a function of time when the misorientation $\theta = 15°$. The legend shows the ϵ-value, and the corresponding ψ_0 value can be read from the table in Section 5.1.

For $\epsilon = 0.3$, the growth stops suddenly, and we have grain growth stagnation. For the larger values of ϵ, the growth also suddenly slows down dramatically. The larger ϵ is, the sooner the growth seems to slow down, and the final grain size is larger for the larger ϵ-values.

In Figure 5.5 the results from the simulations with $\epsilon = 0.1$ and $\epsilon = 0.3$ are plotted with the standard deviation. The grain growth for $\epsilon = 0.1$ appears to be linear in time, at least when the standard deviation is taken into account. In the plot of $\epsilon = 0.3$, the grain shrinks for some time before stagnation sets in. The grain growth before stagnation appears to be slightly nonlinear, even with the standard deviation included. It is possible to interpret the growth as linear, but the plot is less convincing than for $\epsilon = 0.1$. For higher values of ϵ, the stagnation sets in too soon to determine the growth before stagnation.

There seem to be small, slow fluctuations in some of the plots of R^2, after the stagnation is believed to have set in. Because of these fluctuations, it is difficult to determine exactly when the stagnation begins. Both for $\epsilon = 0.4$ and $\epsilon = 0.5$, the center grain slowly shrinks and then grows a little. It is not impossible that if the system had been allowed to continue for a very long time, there could still be some very slow growth, but it does not seem likely.

5.4 Small misorientation

In this section we used the misorientation $\theta = 5°$ to run simulations for a small misorientation. An example of the ψ-field and the corresponding Voronoi diagram for this misorientation can be seen in Figure 5.6. The simulation parameters for

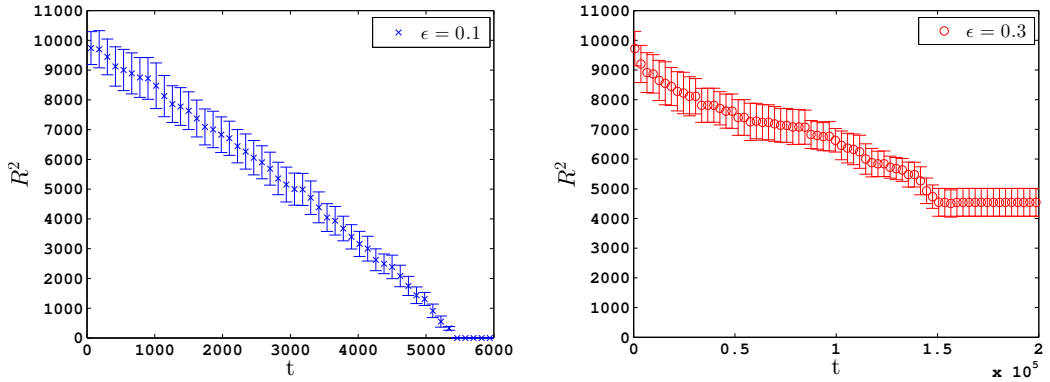

Figure 5.5: The plots show the square of the radius as a function of time for (ϵ, ψ_0)=(0.1, -0.195) and (0.3, -0.31). The misorientation is $\theta = 15°$. The results are plotted with the standard deviation of the measurements. For $\epsilon = 0.3$ there is grain growth stagnation.

the figure are $(\epsilon, \psi_0) = (0.1, -0.195)$ and the figure is from the time $t = 3000$. In this case the grain boundary is composed of discrete dislocations, and looks very different from the continuous grain boundary in the large misorientation case in Figure 5.1, which is from a simulation with the same ϵ and ψ_0. The ψ-field for $\theta = 5°$ clearly shows the individual dislocations. The Voronoi diagram shows the same dislocations as clusters of two or three atoms, with some imperfect hexagonal shapes surrounding them. Compared to the Voronoi diagram for the same misorientation, but with $\epsilon = 0.3$ in Figure 5.3a, the larger ϵ-value gives more clearly defined dislocations, just as was observed in the large misorientation case.

In the figures, the circular shape of the initial center grain appears not to have been conserved perfectly. The dislocations may be moving with slightly different normal velocities, or the system was forced to take this shape during the initial coarsening process, when the grain boundary was created and the necessary dislocations were formed.

Figure 5.7a shows the number of dislocations as a function of time. As in the large misorientation case, the number of dislocations fluctuates for $\epsilon = 0.1$ and $\epsilon = 0.2$, before it drops rapidly to zero. For larger ϵ, the number of dislocations appear to be constant, and they do not drop to zero. The fluctuations in the measurements are even more surprising here than in the large misorientation case. In the ψ-field for $\epsilon = 0.1$ in Figure 5.6 we observe the individual dislocations. Yet we still see fluctuations in dislocations for this ϵ-value. It seems likely that this method of measuring dislocations is not the best tool to analyze systems with small ϵ-values. We see more clearly defined dislocations in the Voronoi diagram for $\epsilon = 0.3$ in Figure 5.3a.

The square of the radius for different ϵ-values is plotted in Figure 5.7b. For $\epsilon = 0.1$ and $\epsilon = 0.2$, the grain growth appears to be linear in time, as in the large

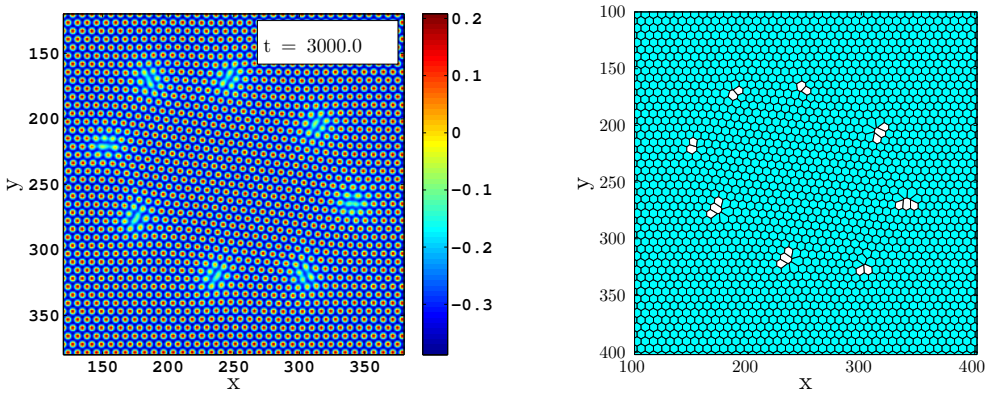

Figure 5.6: A bicrystal with a misorientation $\theta = \pi/36 = 5°$ at $t = 3000$, and a part of the corresponding Voronoi diagram. The parameters of the simulation is $\epsilon = 0.1$ and $\psi_0 = -0.195$. In the Voronoi diagram the atoms with six neighbors are colored light blue and the atoms with a different number of neighbors are colored white.

misorientation case, but it is much slower. For the undercooling $\epsilon = 0.3$ and larger, the grain growth stagnates, as for the large misorientation case. However, the stagnation process looks very different in this case. The growth slows down much earlier in the simulation and the dynamics for different ϵ-values are very similar to each other. But as in the large misorientation case there appear to be small fluctuations of the center grain area after the stagnation has set in.

In Figure 5.8 we can see the trajectory of the dislocations as the grain shrinks from a simulation with $(\epsilon, \psi_0) = (0.2, -0.27)$. There was no stagnation in this simulation. Each trajectory is made up of a pair of dislocations moving together, like the ones seen in the Voronoi diagram in Figure 5.3a. The dislocations appear to be moving approximately radially to the center, and the number of dislocations appear to be conserved, at least until just before the center grain disappears. As will be discussed in Section 6.3, this indicates that the center grain rotates.

5.5 Intermediate misorientation

The intermediate misorientation we ran simulations for is $\theta = 10°$. The grain boundary for this misorientation when $\epsilon = 0.3$ can be seen in the Voronoi diagram in Figure 5.3b. In the figure it seems to be composed of discrete dislocations that are closer to each other than in the small misorientation case.

In Figure 5.9a the number of dislocations have been plotted as a function of time. As in the dislocation plots for the other misorientations, there are fluctuations for the small ϵ-values. The fluctuations become smaller as ϵ increases until the number of dislocations becomes constant for the larger ϵ. In Figure 5.9b the square of the radius is plotted as a function of time. The grain growth stagnation

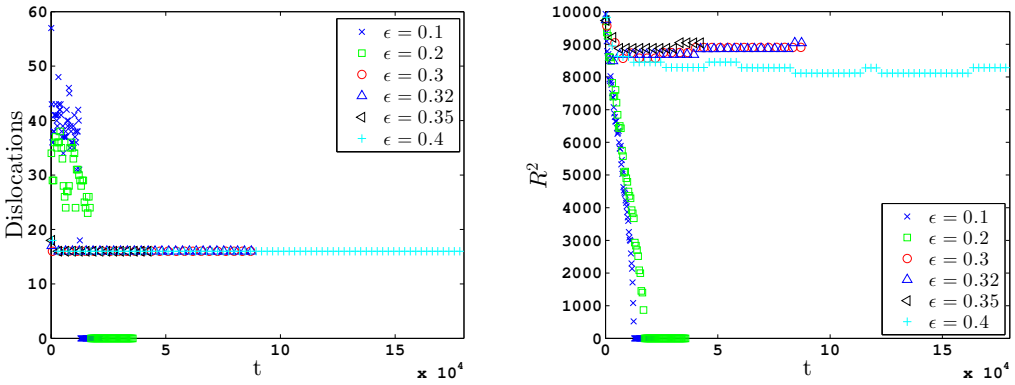

(a) Dislocations as a function of time **(b)** R^2 as a function of time

Figure 5.7: (a) The number of dislocations as a function of time when the misorientation is $\theta = 5°$. (b) The square of the radius of the embedded crystal as a function of time when the misorientation is $\theta = 5°$. The legend shows the ϵ-value, and the corresponding ψ_0 value can be read from the table in Section 5.1.

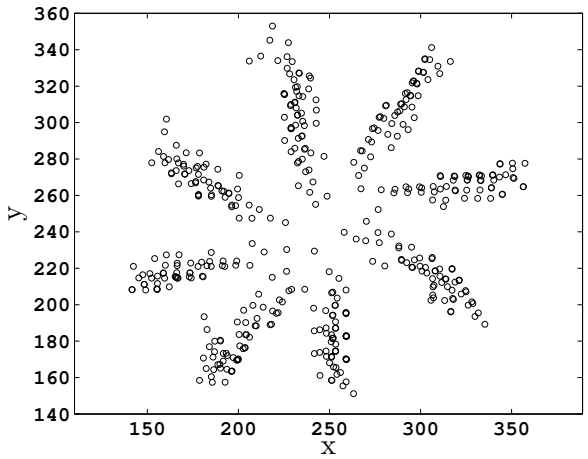

Figure 5.8: Dislocation trajectory for $(\epsilon, \psi_0) = (0.2, -0.27)$ when $\theta = 5°$. The dislocations move approximately radially to the center.

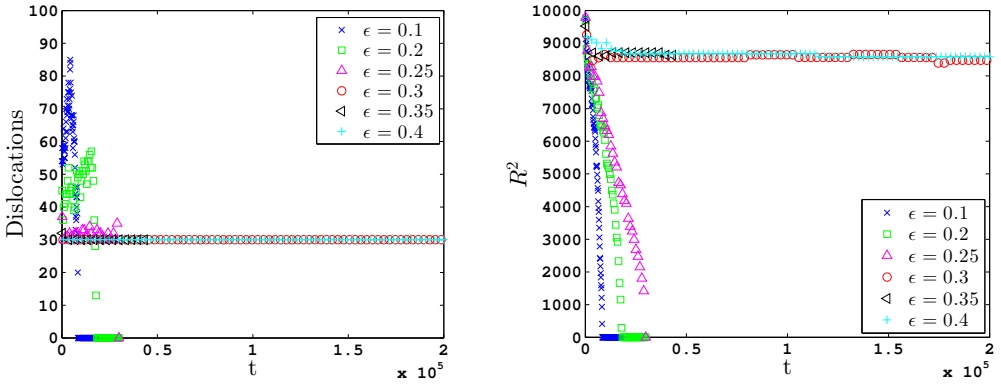

(a) Dislocations as a function of time **(b)** R^2 as a function of time

Figure 5.9: (a) The number of dislocations as a function of time when the misorientation is $\theta = 10°$. (b) The square of the radius of the embedded crystal as a function of time when the misorientation is $\theta = 10°$. The legend shows the ϵ-value, and the corresponding ψ_0 value can be read from the table in Section 5.1.

seems to begin at $\epsilon = 0.3$, as in the simulations with other misorientations. The grain growth dynamics for simulations with stagnation are very similar to each other, as in the small misorientation case.

In Figure 5.10 the dislocation trajectory for $\theta = 10°$ when $\epsilon = 0.25$ can be seen. Dislocation pairs move to the center of the system as the grain shrinks. There are more dislocations along the grain boundary in this case than in the small misorientation case. As mentioned in Section 4.2.1, Wu and Voorhees [19] found that some of the dislocations moved tangentially in a similar system with the same misorientation. That might also be happening here, but it is difficult to be certain based on this figure. The system studied in that article was larger than the one studied here, so the dislocations had more time to move around before the center grain disappeared. In our figure the dislocations appear to move independently at first, but when they get closer to each other they may begin to interact with each other. As the center grain disappears they are all annihilated, but there may be some reactions before that.

According to the Wu and Voorhees [19] there is a faceting-defaceting process in the intermediate misorientation case, resulting in nonlinear grain growth. The grain growth for all three misorientations is plotted in Figure 5.11 in order to compare the results. The parameters in all the simulations are $(\epsilon, \psi_0) = (0.1, -0.195)$. The plot shows that as the misorientation increases, the growth speeds up. The growth for $\theta = 10°$ could be interpreted as slightly less linear, especially in the beginning of the simulation, but the results are inconclusive. It is possible that our system is too small to observe the faceting-defaceting dynamics.

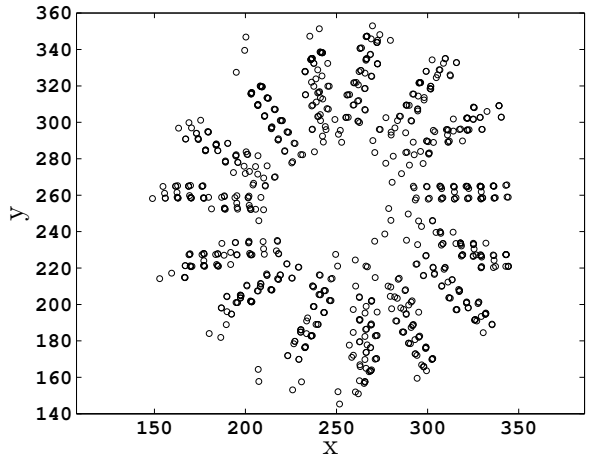

Figure 5.10: Dislocation trajectory for $(\epsilon, \psi_0) = (0.25, -0.29)$ when $\theta = 10°$.

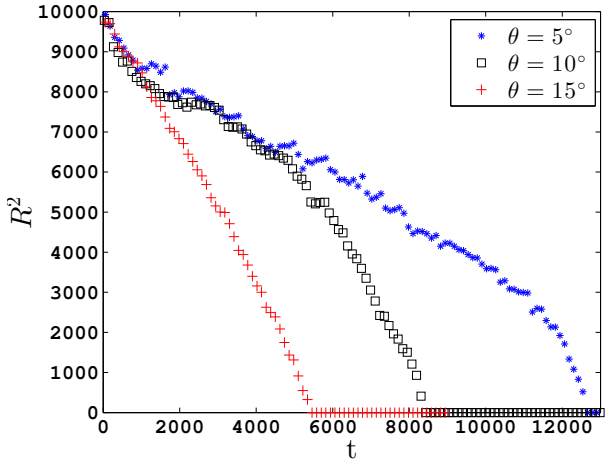

Figure 5.11: The square of the radius of the embedded crystal as a function of time for different misorientations when $(\epsilon, \psi_0) = (0.1, -0.195)$.

5.6 Reduced mobility

For small ϵ, when there is no stagnation, the grain growth appears to be linear in time, $R^2 \propto t$. When $\theta = 10°$ there could be a faceting-defaceting process occuring, as mentioned in the previous section, but our results are inconclusive. Therefore we have chosen to assume that the grain growth is linear also for this misorientation, in order to find a value for the reduced mobility M^*. The reduced mobility is defined as

$$M^* = -\frac{1}{2}\frac{dR^2}{dt} \tag{5.3}$$

as explained in Section 4.2.2. M^* was measured by finding the constant of proportionality α in the linear expression $R^2 = \alpha t$, and inserting this into the equation for M^*. The new expression becomes $M^* = -\alpha/2$. Because the center grain is shrinking, the constant α is negative, and the reduced mobility is therefore a positive value.

We measured the reduced mobility M^* in our simulations without grain growth stagnation. In Figure 5.12a the reduced mobility is plotted as a function of the undercooling ϵ. In Figure 5.12b M^* is plotted as a function of the misorientation θ. The reduced mobility M^* appears to decrease with increasing ϵ. As the temperature goes down the grain boundary moves more slowly. This is especially apparent in the figure where M^* is plotted as a function of θ. The results for M^* are almost consistently decreasing as ϵ increases. There is a slight inconsistency for $\epsilon = 0.15$, which was only measured for one misorientation. Ideally we should have had some more measurements for the different ϵ and θ. Judging by the same figure, the mobility also seems to depend on the misorientation. For $\theta = 5°$ the results for M^* are much closer to each other than for the other misorientations, where the results are much more scattered. However, this is mostly due to the results for $\epsilon = 0.1$. The other results are much closer together.

In this calculation we have not considered how rotation of the grain might change the measurements. M^* is expected to be dependent on θ, so this could be a source of error. We have also assumed that the change in area is linear in time, which is not necessarily a correct assumption in all the simulations.

5.7 The hyperbolic PFC model

We also ran some simulations using the hyperbolic PFC model. We were mostly interested in discovering whether we found grain growth stagnation using this model as well. We therefore performed simulations for $(\epsilon, \psi_0) = (0.4, -0.34)$, as we had observed stagnation in this case for the parabolic equation. As in the 1D case in Chapter 2, we chose to run simulations for $\tau = 2$ and $\tau = 5$, where τ is the flux relaxation time. The grain growth is plotted as a function of time for $\theta = 15°$

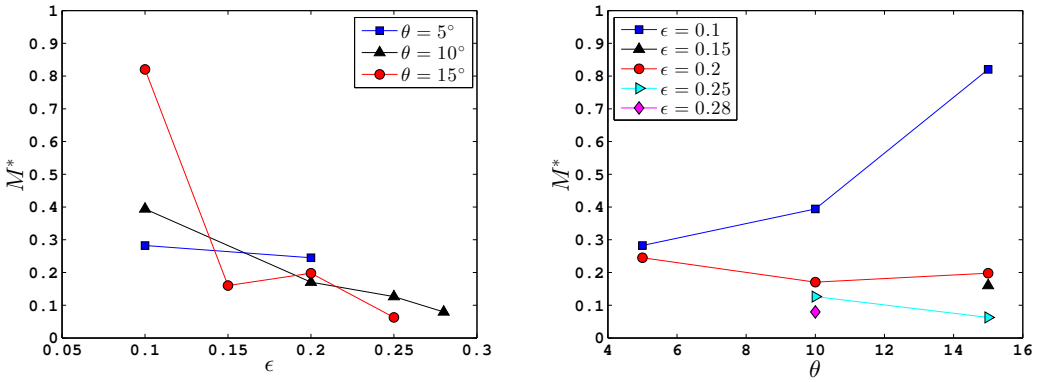

(a) M^* as a function of ϵ **(b)** M^* as a function of θ

Figure 5.12: These plots of the reduced mobility only include results for ϵ-values that do not give grain growth stagnation. (a) The reduced mobility M^* as a function of ϵ for different misorientations. (b) M^* as a function of θ.

in Figure 5.13. The results for the parabolic case with the same parameters are also plotted. The plot shows that there is grain growth stagnation also in the hyperbolic case, but it takes a little longer time to set in. There is very little difference for the different values of τ. Grain growth stagnation will be further considered in Section 5.8.

5.8 Grain growth stagnation

We wanted to take a closer look at the grain growth stagnation for the different misorientations and ϵ-values. In this plot we included results from more simulations around $\epsilon = 0.3$, and found that there is also stagnation for $\epsilon = 0.28$ for $\theta = 5°$ and $\theta = 15°$, but not for $\theta = 10°$. The value of ϵ for which stagnation first appears is therefore not very different for the different misorientations.

Because of the small fluctuations in the final grain size in some of the simulations, there can be some uncertainty as to what time exactly the stagnation sets in. We used the results from the Voronoi analysis and observations of the time evolution of the ψ-field, in order to determine when stagnation set in. In our observations of the ψ-field we could often not see the small fluctuations from the Voronoi analysis. Either the Voronoi analysis is imperfect, or at this late stage in the simulations the changes in ψ are so small that they are difficult to observe visually.

A plot of the time that grain growth stagnation sets in for the different values of ϵ and θ can be seen in Figure 5.14a. In the small and intermediate misorientation case, the stagnation time changes very little with ϵ. It appears to be constant for the misorientation. The stagnation appears to set in slightly faster

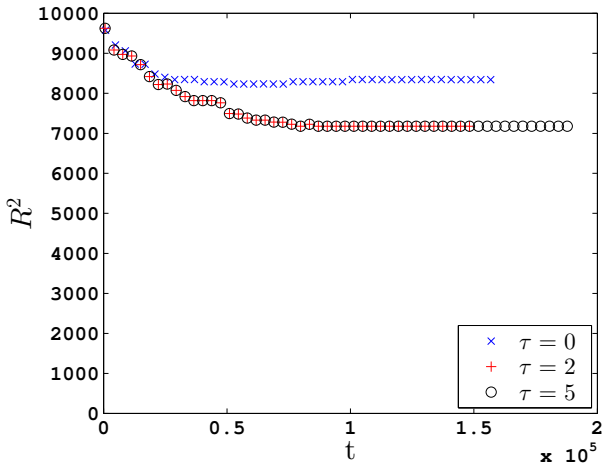

Figure 5.13: The square of the radius of the embedded crystal as a function of time for the parabolic case $\tau = 0$ and the hyperbolic case with $\tau = 2$ and 5. The parameters are $(\epsilon, \psi_0) = (0.4, -0.34)$ with $\theta = 15°$.

for $\theta = 5°$ than for $\theta = 10°$, but there is not a big difference between the two different θ. In the large misorientation case, the results look very different. The stagnation time first increases as ϵ increases, then it decreases and appears to reach a constant value. This is approximately the same value that was found for the lowest values of ϵ. As $\epsilon = 0.3$ looks so different from the results for the other ϵ-values, it is possible that it is an outlier, and that the stagnation time of $\theta = 15°$ is also a constant value.

The final grain size, plotted in Figure 5.14b as R^2, is also different for the different misorientations. The final grain size is approximately the same for $\theta = 5°$ and $\theta = 10°$. There is much larger variation in the large misorientation case than in the small and intermediate misorientation case. For large θ the final grain size increases with increasing ϵ, until it possibly converges to the constant values for the other misorientations. The results for $\epsilon = 0.3$ varies from the others also here. When the center grain has more time to shrink, when t_{stag} is larger, as when $\epsilon = 0.3$, the final grain size is smaller. However, the final grain size is relatively small for the lowest ϵ-values as well. Presumably the mobility of the grain boundary before stagnation decreases as ϵ increases.

The standard deviation σ_{R^2} in the plot of the final grain size comes from the uncertainty in the measurement of the area. The error is larger for the small misorientation measurements, probably because there are fewer dislocations in the grain boundary for $\theta = 5°$, and because the center grain is not a perfect circle, as can be seen in Figure 5.6.

Some simulations were run for the hyperbolic case as well. The simulations were run for the parameters $(\epsilon, \psi_0) = (0.4, -0.34)$ and the misorientations $\theta = 5°$ and $\theta = 15°$. We ran hyperbolic simulations with flux relaxation time $\tau = 2$

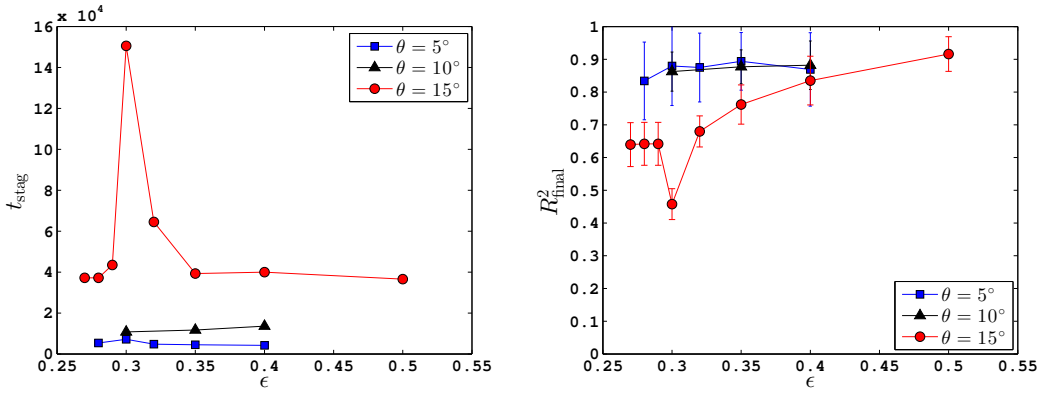

(a) Stagnation time as a function of ϵ **(b)** Final grain size as a function of ϵ

Figure 5.14: (a) The plot shows the stagnation time as a function of ϵ for the different θ. The stagnation time is defined as the time at which the system has slowed down sufficiently that we assume it has stagnated, although some of the results show fluctuations after this point. (b) R^2 of the center grain after stagnation, divided by R^2 of the initial grain. The error is σ_{R^2} from the measurement of R. The results are from simulations with the parameters in the table in Section 5.1.

and $\tau = 5$. The results for the stagnation time and the final grain size can be seen in Figure 5.15. The results are plotted with the results from the parabolic case for the same parameters and misorientations. The stagnation time and the final grain size is different for the parabolic case and the hyperbolic case, but the results are the same for $\tau = 2$ and $\tau = 5$. The time before stagnation sets in is significantly longer for the hyperbolic case. The difference between t_{stag} for the two misorientations is approximately the same in the hyperbolic and the parabolic case. This is also the case for the final grain size.

5.9 Summary of 2D simulations

The grain boundaries for the different misorientations look very different. When $\theta = 15°$, the grain boundary is almost continuous. When $\theta = 5°$, the individual dislocations are identifiable. Examples of the grain boundaries for the different misorientations can be seen in the Voronoi diagrams for $\epsilon = 0.3$ in Figure 5.3. The dislocations are more clearly defined in these images than they are in the Voronoi diagrams for $\epsilon = 0.1$ in Figure 5.2 and 5.6. They even form dislocation pairs of five and seven atoms. This suggests that the Voronoi diagrams are more accurate at larger ϵ-values. The number of dislocations are determined by the misorientation, and it increases when θ increases. From the dislocation plots we can read the number of dislocations when it becomes constant for larger ϵ. When $\theta = 15°$ there are 48 dislocations, when $\theta = 10°$ there are 30 dislocations, and

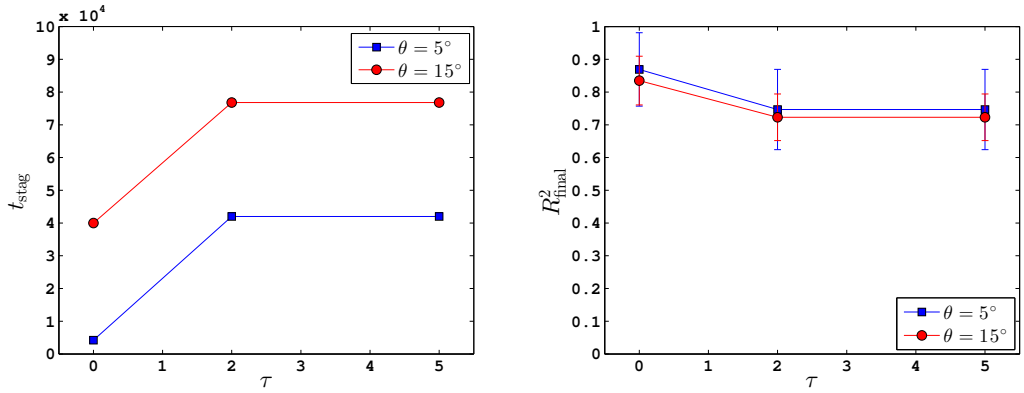

(a) Stagnation time as a function of τ **(b)** Final grain size as a function of τ

Figure 5.15: Stagnation measurements for the parabolic case ($\tau = 0$) and the hyperbolic case with $\tau = 2$ and 5. The simulations are for $(\epsilon, \psi_0) = (0.4, -0.34)$ and $\theta = 5°$ and 15°. (a) The plot shows the stagnation time as a function of τ. (b) R^2 of the center grain after stagnation, divided by R^2 of the initial grain. The error is σ_{R^2} from the measurement of R.

when $\theta = 5°$ there are 16 dislocations. These dislocations are grouped in pairs.

For small ϵ-values, when there is no stagnation, the grain growth appears to be linear in time, $R^2 \propto t$. When $\theta = 10°$ there could be a faceting-defaceting process occuring, but our results are inconclusive. The reduced mobility M^* appears to decrease with increasing ϵ. The results also seem to depend on θ.

At around $\epsilon = 0.3$ grain growth stagnation sets in. The misorientation θ has a big influence on how the stagnation dynamics are affected by the undercooling. Most notably, there is a difference between the results for $\theta = 15°$ and the results for the other misorientations. The difference between $\theta = 5°$ and $\theta = 10°$ is relatively small.

We found that there was grain growth stagnation also for the hyperbolic case, but it took a little longer to set in. There was very little difference between $\tau = 2$ and $\tau = 5$, at least in the systems we simulated.

Chapter 6

Discussion

6.1 The 1D PFC model

Our findings for the 1D case have been summarized and discussed in Chapter 2. The phase diagram and one-mode approximation calculated by Elder and Grant [6] are in agreement with our results. We found solidification and melting when expected, and we were able to simulate a crystal in coexistence with a liquid when the parameters were chosen from the solid-liquid coexistence region. By fitting envelope functions to the interface between the crystal and the liquid we were qualitatively able to confirm that the interface becomes steeper when ϵ increases. We were not able to quantitatively confirm the trend, as we were not able to find a data collapse for the results. This could in part be explained by the difference in the mean order parameter for the two phases, which was $\psi_{0,c}$ for the crystal and $\psi_{0,l}$ for the liquid. This causes the interface above and below $\psi_{0,l}$ in the liquid to be different. We chose to make our measurements on the largest interface. This difference in interface could make it more difficult to find a data collapse, and therefore a general function for the coexistence interface.

We also looked at a solid front propagating into a homogeneous liquid, in order to test the marginal stability analysis for both the parabolic and hyperbolic case. The simulation results for the front velocity seem to be in agreement with the theory. By changing the threshold used to find the position of the front, it seems like the results for the front velocity converge to the theoretical prediction when the threshold is lowered. The results for $\tau = 2$ fit best with this assumption. In the parabolic case the results do not change that much, and for $\tau = 5$ the results seem to converge for smaller ϵ, but for larger ϵ the results slightly exceed the theoretical prediction. A convergence caused by decreasing the threshold could be explained by the derivation of the marginal stability analysis. The basis of the theory is a perturbation with a small amplitude. Perhaps the front should therefore be defined as the first oscillation in the liquid, which can only be picked up by using a low threshold.

The results for the wavenumber k_f behind the front did not agree well with the theory, at least not for the hyperbolic case. There could be different reasons for this. We may have chosen an unstable method of measuring the wavenumber, by using the average wavelength in the given region. There was also some uncertainty as to where in the system k_f is supposed to be found. We chose to find k_f in the region between the rapidly decreasing amplitude of the front and the center of the bulk, which has slightly larger amplitude than the rest of the crystal behind the front. Figure 2.13 shows the amplitude change in the system. We chose not to interpret the entire bulk as the pattern behind the front, as the amplitude change could indicate that there was also a change in wavenumber. Therefore we chose to define k_f as the wavenumber of the crystal phase immediately following the front, and not necessarily of the whole bulk. This choice gave better results for the parabolic case.

Another possibility is that the Eckhaus instability could have influenced our system. Galenko and Elder [9] calculate the Eckhaus instability and find that it should affect k_f in the hyperbolic case when ϵ is large. We have not looked further into this possibility ourselves, and it is unclear exactly how the Eckhaus instability should influence our results. However, our results are much better for the parabolic simulations than the hyperbolic simulations, so it is not impossible that the results for the hyperbolic case could be connected to the Eckhaus instability. According to the plot in Figure 2.12 the Eckhaus instability only comes into effect at a certain ϵ, and our results deviate from the theory even for small ϵ. This could indicate that our results are not related to the Eckhaus instability.

A final possible explanation for the poor agreement between the measured k_f and the theoretical prediction when $\tau = 2$ and 5, is that the bulk behind the front has not had time to fully form before the front disappears. As shown in Figure 2.15, fluctuations ahead of the front were observed to interact, form separate bulks and "swallow" the front. This effect was especially pronounced in the hyperbolic case and for large ϵ, which could be related to the poor results under these condtions.

6.2 Comparison between 1D and 2D

In our simulations we have examined the PFC model both in 1D and 2D. The specific systems we have studied are slightly different, however, and not just in dimensionality. Aside from the coexistence simulations, the 1D case measures the solidification process, while the 2D case measures dynamics in a solidified system. The results are therefore difficult to compare. In both cases we have looked at both the parabolic and the hyperbolic PFC equation, though our measurements are more comprehensive for the hyperbolic model in the 1D case.

When we looked at a front propagating into a homogeneous phase in 1D, we found that the front velocity $V = dx/dt$, where x is the front position, increased

with ϵ, as in the theoretical predictions. In other words, when the temperature in the system decreased the front propagated faster. This can be seen in Figure 2.16. In the bicrystal case we simulated in 2D, the crystal growth slowed down when ϵ increased, as seen in the reduced mobility measurements $M^* = -\frac{1}{2}\frac{dR^2}{dt}$ in Figure 5.12. The dynamics depend very differently on ϵ in the two cases. This could be caused by the dimensionality or the difference in the type of system. It is also possible that our measurements on M^* are wrong, which will be further discussed in Section 6.6.

6.3 Grain growth and rotation

The dynamics of the circular bicrystal have been simulated in Chapter 5. The bicrystal has been described theoretically by both the classical model and the Cahn-Taylor model. Both models are explained in Section 4.1. The classical grain growth is determined by the grain boundary mobility M, the grain boundary energy γ and the curvature κ by the following relation, $v_{\mathbf{n}} = M\gamma\kappa$. When applied to the circular bicrystal the grain growth is found to be linear in time, $R^2(t) = R_0^2 - 2M\gamma t$. This equation applies to the case when there is no rotation and the grain boundary is continuous. When θ is constant, $M(\theta)$ and $\gamma(\theta)$ are also constant, which simplifies the calculation. The Cahn-Taylor model describes the general case.

The classical theory seems to apply to the case of $\theta = 15°$. For $\epsilon < 0.27$ there is no stagnation, and the center grain seems to shrink linearly, as expected. We assume that there is very little rotation in this case, as this has been measured in previous simulations on a similar system [19]. The system can also be described by the Cahn-Taylor model when there is no coupling or sliding, or in other words no rotation. With the added assumption that the volume free energy f_V is negligible, the Cahn-Taylor model gives the same equation as the classical theory. The reduced mobility measurements in Figure 5.12 shows that the grain growth also depends on ϵ, indicating that the mobility M or grain boundary energy γ depends on temperature, as well as misorientation.

In the small misorientation case, when $\theta = 5°$, the grain growth also appears to be linear in time for values of ϵ that do not give stagnation. Judging by the dislocation trajectory in Figure 5.8, the number of dislocations appear to be conserved, and moving approximately radially to the center of the system. This is a strong indication that there is rotation, and that it is caused by coupling of the normal and tangential velocity. There is probably no sliding involved. In the coupling-only case of the Cahn-Taylor model, the following relation is found, $R(t)\theta(t) = \text{const}$, which means that the number of dislocations is conserved, and when the grain shrinks the misorientation θ increases. For small θ, when there is no applied stress σ and no free volume energy f_V, the grain growth can be described by the following relation, $R^2(t) = R_0^2 - 2M_b|b|a_2t$, where M_b is the

mobility of the discrete dislocations, $|b|$ is the magnitude of the dislocations' Burgers vector and a_2 is a constant from the Read-Shockley definition of grain boundary energy. The small θ allows for the approximations that make it possible to reach this relation. We found the growth to be approximately linear, which fits the prediction of the Cahn-Taylor model. The Cahn-Taylor relation for this case looks different than the classical grain growth relation, and the grain growth for the different θ is not expected to show the same behavior. Judging by the plots of R^2 in Figure 5.11 and the plots of mobility in Figure 5.12, the grain growth depends on θ, but it also seems to depend differently on ϵ for the different θ. However, the data is slightly limited, especially for the small misorientation case.

The linear grain growth for both the small and large misorientation case are in agreement with the results found by Wu and Voorhees [19] for $\epsilon = 0.1$. We have used the same explanatory model as they used for these results.

The results for simulations in the intermediate region of θ, where we chose to look at $\theta = 10°$, seem to be less linear than for the other misorientations. We still assumed linearity when we found the reduced mobility in Figure 5.12, because our results are not very far from linearity. Wu and Voorhees [19] suggested that there was a faceting-defaceting process present in their simulations, causing the growth to be nonlinear. This process is assumed to be caused by the nature of the grain boundary for this misorientation, as the dislocations are too far apart for the grain boundary to be continuous and so close to each other that they can interact. The authors also observe tangential motion of some of the dislocations, causing the grain boundary to alternate between being continuous and being composed of discrete dislocations, which affects the normal velocity. This is assumed to cause the faceting-defaceting process. In our simulations, the dislocation trajectory in Figure 5.10 shows dislocations moving perpendicularly to the grain boundary. Some of them may move tangentially as well, but the results are inconclusive. With a larger system, like the one used by Wu and Voorhees [19], with which we could track the dislocations for a longer time, we might be able to observe this. However, that would require consideration of the problems discussed in Section 6.5, regarding our tools of analysis.

It is possible that the nature of the grain boundary for $\theta = 10°$ makes it more difficult for the Cahn-Taylor model to predict the results. Without the assumptions for the small misorientation case, and considering that both rotation and dislocation reactions were found for the intermediate case in previous simulations [19], there might be too many unknown parameters to find an expression for the growth.

6.4 Grain growth stagnation

In Section 4.6 we look at possible causes of grain growth stagnation. Stagnation occurs when the system reaches a metastable state, when it will cost more energy

for the system to relax further toward equilibrium than will be gained by doing so. The two causes of grain growth stagnation that we have looked at were solute segregation causing the grain boundary energy γ to decrease [2], and a given ratio of low-mobility grain boundaries in the system slowing down the grain growth until there is stagnation [3]. It is suggested that also a small ratio of low-mobility grain boundaries could cause grain growth stagnation.

It is the low-mobility grain boundaries that are the most likely cause of stagnation in our simulations. The ratio of low-mobility grain boundaries to all grain boundaries in the system increases when the temperature is low i.e., when ϵ is large. Therefore, according to Holm and Foiles [3], the stagnation sets in earlier when the temperature is lowered. We find stagnation for large ϵ, which seems to fit the theory of low-mobility grain boundaries causing stagnation.

The most pronounced differences between low- and high-mobility grain boundaries are their width and motion. High-mobility grain boundaries are rough and move continuously. Low-mobility grain boundaries are smooth and move in a step-like motion. The plot of R^2 as a function of time when $\epsilon = 0.3$ and $\theta = 15°$ in Figure 5.5 shows stagnation, but before the stagnation sets in the grain shrinks. This shrinkage is less linear than the shrinkage when $\epsilon = 0.1$ in the same figure. This nonlinearity could be a sign of low-mobility grain boundaries. The theory could be further tested by adding strain to the system. Strain can cause a roughening of the grain boundaries, as found by Gokhale et al. [22] and summarized in Section 4.3. If the low-mobility grain boundaries are causing the stagnation, there would presumably be less stagnation with more high-mobility grain boundaries in the system, created by applying strain.

In the plots in Figure 5.14 the measurements on the stagnation simulations can be seen. In Figure 5.14a we can see that the stagnation time increases with the misorientation θ. The stagnation time is the time it takes before the stagnation sets in. It appears to be independent of ϵ for $\theta = 5°$ and $10°$. The stagnation time for $\theta = 15°$ also appears to be independent of ϵ, except in the region around $\epsilon = 0.3$, but this could be an outlier. The smallest value of ϵ where stagnation is observed to occur also seems to depend on θ. We have not mapped out this region completely, but stagnation is observed for smaller ϵ when $\theta = 15°$ and $5°$ than when $\theta = 10°$. However, the differences are relatively small.

If the stagnation is caused by low-mobility grain boundaries, it is a little surprising that the amount of low-mobility grain boundaries do not seem to matter, as the stagnation time is independent of temperature for the smaller misorientations. However, since there is only one grain boundary perhaps the ratio of low-mobility grain boundaries becomes a less meaningful term. Possibly the entire grain boundary becomes low-mobility when a certain ϵ is reached, and this takes the same amount of time regardless of the temperature of the system.

It is possible that the type of grain boundary is also relevant. The continuous grain boundary for large θ looks and behaves differently than for small θ. The

grain boundary energy γ is assumed to increase with increasing θ. The grain boundaries with the smallest γ stagnate earlier than the ones with large γ. Perhaps the system reaches a metastable state earlier when γ is small because the energy in the system is already close to that of the equilibrium state. And perhaps when the grain boundary is continuous it takes a little more time for the grain boundary to reach the transition when it becomes low-mobility.

In Figure 5.14b the final grain size of the stagnated system is plotted as a function of ϵ. The results for $\theta = 5°$ and $10°$ appear to give approximately the same results, and to be independent of ϵ. When $\theta = 15°$ the final grain size increases with ϵ, possibly converging to the final grain size of the other misorientations.

If the grain boundary in the large misorientation case is high-mobility at first, the reduced mobility decreases with increasing ϵ. When the stagnation time is approximately the same, this could explain how the final grain size increases with increasing ϵ. As seen in Figure 5.11, the grain growth slows down for small θ. Perhaps the grain boundaries with discrete dislocations are already low-mobility.

It should be mentioned that some of our stagnation measurements are a little uncertain. The plots of R^2 seemed to fluctuate for some of the simulations, after observations of the ψ-field seemed to indicate that there was stagnation. There could be changes in the ψ-field that were too small for us to observe. We chose to find the stagnation by using a combination of observing the ψ-field and using the plot of R^2. It is perhaps not the most robust method and could therefore be a source of error.

In the hyperbolic case there is also grain growth stagnation, but the simulation runs a little longer before the stagnation sets in.

6.5 The Voronoi diagram analysis

We performed the dislocation analysis by using the Voronoi diagram. This turned out to be an inaccurate method for the small ϵ simulations, at least when tracking individual dislocations. The Voronoi diagram found the area where dislocations could be found, so the analysis could be used in finding the approximate area of the center grain, but the number of dislocations that was found was wrong for small ϵ. In the large ϵ simulations our results were good, but in these cases we had stagnation, and tracking the number of dislocations after grain growth stagnation was not that interesting.

The dislocation trajectories in Figure 5.8 and 5.10, that were found using the Voronoi diagram and appear to be accurate when comparing them to visualizations of the ψ-field, are for $\epsilon = 0.2$ and $\epsilon = 0.25$, which is directly below the values of ϵ that caused stagnation. The plots show where the dislocations can be found, and they appear to be conserved, at least before the grain shrinks to the size where the dislocations begin to react. But the plots of the number of

dislocations from the same data in Figure 5.7a and 5.9a show fluctuations in the number of dislocations. This makes it difficult to differentiate between when the dislocations are conserved and when there are dislocation reactions.

It would have been interesting to get a conclusive result on the number of dislocations, also for the small ϵ simulations. The Voronoi diagram may not have been the best method to identify dislocations. It is also possible that our definition of dislocations may not have been robust.

6.6 Are our results trustworthy?

We found grain growth stagnation in our bicrystal simulations of the larger ϵ-values. The question is whether these results are physically correct or if they are created by the PFC model. That depends on the accuracy of the PFC model.

Heinonen et al. [12] argue that the standard PFC model does not correctly model elastic excitations, as they relax on a smaller time scale than the diffusive dynamics of the ψ-field. They derived an alternate version of the PFC method that would mechanically equilibrate the system for each timestep. We summarized their article in Section 3.3. We have not implemented their method in our simulations, and as it seems like the mechanical equilibrium condition affects the ψ-field dynamics, our results, not only regarding stagnation, could be called into question. The change in ψ-field dynamics was especially apparent for the cold system they tested. However, they suggest that placing the system close to the liquid phase in the phase diagram would make the mechanical equilibrum condition less important, because the elastic energies are small under these conditions. All our simulations on the 2D bicrystal are performed on the edge between the solid phase and the solid-liquid coexistence phase. If the elastic energies are small enough for large ϵ as well as small ϵ, it is possible that our results could still be accurate.

However, the growth rate in our results and in Heinonen et al. [12] look different. According to the paper, the slope of the linear fit for R^2 as a function of time should become steeper for increasing ϵ when the mechanical equilibrium condition is included. In our results the opposite seems to be true. The growth slows down when the system becomes colder. In Figure 5.12 the reduced mobility M^* is plotted for the simulations without stagnation. The reduced mobility is found from the slope, so the results are comparable. In the figure we see that M^* seems to decrease as ϵ increases. In the reduced mobility measurements on the MD simulations by Trautt and Mishin [20], summarized in Section 4.2.2, the reduced mobility also decreases with decreasing temperature, except close to the melting point. Their results seem to resemble ours. The MD simulations look at larger misorientations than we have used and the system has a different crystal symmetry than the hexagonal pattern in the PFC simulations. This could have something to do with the different results, but the MD results still

seem inconsistent with the results from the PFC equation with the equilibrium condition.

If the difference in results from the standard and the mechanically equilibrated PFC equation is not only because of the proximity to the solid-liquid coexistence region in the phase diagram, the effects of the mechanical equilibrium condition seems to be the largest at large ϵ-values and it was at these values that we observed stagnation. We do not know if we would have found stagnation with the mechanical equilibrium condition, which means that our results could be wrong. The inability of the system to relax elastic strains could have caused grain growth stagnation. As the reduced mobility is different for this case and the MD case, it would be interesting to see the effects on grain growth for a larger selection of systems. And it would be interesting to see how our results might change with the elastic equilibrium condition included.

We also ran a few simulations with the hyperbolic PFC model, in order to test if there was stagnation also in this case. The hyperbolic model was suggested as a method to include smaller time scales into the simulations, and should therefore presumably be better at relaxing elastic excitations than the standard PFC model. We ran simulations with the hyperbolic model for $\epsilon = 0.4$ and we found grain growth stagnation, as we had in the parabolic case. However, the stagnation took a little longer setting in. It is possible that the hyperbolic model was also unable to properly relax the elastic excitations. The simulations did not really answer the question of whether the grain growth stagnation is a real physical phenomenon for this system.

It is not impossible that stagnation simply does not occur in the simple system of the bicrystal. The MD study by Trautt and Mishin [20] does not say anything about stagnation, and they perform simulations for many different temperatures. The MD simulations are not performed on the same misorientations as in our simulations, but in our results it does not seem like there is a large difference in when we can expect stagnation, depending on the misorientation. The difference in our PFC simulations and the MD simulations in the article, could be caused by difference in dimensionality as the PFC simulations are in 2D and the MD simulations are in 3D, or they could be caused by the difference in crystal structure. But the lack of any mention of grain growth stagnation in the MD bicrystal simulations is another indication that our results may not be accurate.

6.7 Further study

The most important question we were unable to answer is whether or not the observed grain growth stagnation is genuine. The article by Heinonen et al. [12] seems to suggest that the stagnation we observed could be an effect of the seemingly incorrect modeling of elastic excitations in the standard PFC model. This should be examined further, for instance by implementing the alternate version

of the PFC model that ensures mechanical equilibrium. Then we could run simulations with the same parameters as in this thesis, and compare the results.

It would also be interesting to include triple juctions into our systems, and see how these affect the dynamics. We could increase the complexity of the polycrystalline material, and observe how the dynamics are altered. Another method of increasing the complexity of the system considerably would be to increase the dimensionality. The PFC equation can be implemented in 3D, and this would probably change the dynamics of the system. The complexity is increased by both new types of dislocations and misorientations, as three-dimensional grains can rotate in more than one plane.

A further study should also include more tools of analysis. The Voronoi method is a relatively robust, if not the best suited tool for all systems. Some alternative tools would be useful.

The mobility of grain boundaries would also be interesting to study further. Our results seem to match those of the MD simulations by Trautt and Mishin [20], but not the two simulations performed by Heinonen et al. [12]. Perhaps there are other variables than the temperature and misorientation that determine the mobility. In short, there are many reasons it would be interesting to examine the mechanical equilibrium version of the PFC equation further.

Chapter 7

Conclusion

This thesis has mostly been an overview of existing theory on grain growth dynamics and the phase field crystal model. The PFC model is the tool we have used to simulate the systems. For the most part, we have set out to confirm the theory or results of others while gaining a deeper understanding of crystallization dynamics and the PFC model.

In our 1D simulations described in Chapter 2, we confirmed that a crystal can exist in coexistence with a solid, as had been done in 2D by Backofen and Voigt [14]. Qualitatively, we found the same interface trend as in that article. We also tried to examine some things that we have not been able to find in other works. The marginal stability analysis on the parabolic and hyperbolic PFC equation in 1D made predictions that have been examined to some extent [15, 16], but there are still some questions about this theory. Our measurements of the front velocity V gave a good agreement with the predictions from the marginal stability analysis. How we choose to define the front, however, seems to affect the results. It is possible that the front should be defined as the first oscillation of the homogeneous liquid.

Our measurements of the wavenumber behind the front k_f do not agree with the predictions from the marginal stability analysis, at least not for the hyperbolic case. This could be caused by a lack of robustness in our measurement techniques, but the measurements on the parabolic simulations gave the predicted results. The wavenumber for the larger values of τ and ϵ were predicted to be unstable from the Eckhaus instability, but this we were unable to determine. It is possible that in this case, the definition of the front is even more important. From the marginal stability analysis, it is a little unclear where exactly k_f can be found, and where the transition from k^* in the front and k_f behind the front occurs. It is also possible that the limited time of the simulations, especially for the hyperbolic case, could have affected the results. The front disappeared shortly after perturbations ahead of the front grew into separate bulks, limiting the window in which measurements could be made. Perhaps the system was unable to form a large enough bulk behind the front.

In our 2D simulations we limited our examinations to the bicrystal case. We found that the evolution of the simulations not affected by grain growth stagnation seemed to be in agreement with the Cahn-Taylor model and previous simulations [19]. The dynamics depended on the misorientation and the undercooling. The reduced mobility decreased with decreasing temperature, which also seemed to be in agreement with previous simulations [20]. However, our results are perhaps not completely correct. We think that the argument of Heinonen et al. [12], that the PFC model does not correctly model elastic excitations, could influence our results, both regarding reduced mobility and the stagnation that was observed for larger values of ϵ. However, it is not impossible that we have mistaken the growth suddenly slowing down as stagnation, even though we have run some of the simulations for a relatively long time to test this.

The stagnation was found to depend on both the misorientation and the undercooling ϵ, and it was probably caused by low-mobility grain boundaries. However, the effect could merely be a result of the PFC model itself, and not a physical phenomenon. It is hard to tell from the simulations we have performed, but our results should probably be tested by different models in order to answer this question.

The phase field crystal equation was initially considered useful because it could model dynamics on atomic length scales and diffusive time scales. The alternate formulation of Heinonen et al. [12] could become a necessary addition to the model if the standard PFC equation does not give correct results.

We have only considered one- and two-dimensional systems. The 2D systems can represent thin films, but the 1D case is mostly abstract. The results could perhaps still be relevant for real systems, not quantitavely but qualitatively. The marginal stability analysis is difficult to do in higher dimensions than 1D, and the Cahn-Taylor model is applied to a specific bicrystal system in 2D and would be difficult to apply to more complicated systems. The results could still be interesting in regard to more complicated systems, even if the the theory only applies to simplified systems.

Bibliography

[1] MC Cross and DI Meiron. "Domain coarsening in systems far from equilibrium". In: *Physical review letters* 75.11 (1995), p. 2152.

[2] Junjie Li, Jincheng Wang, and Gencang Yang. "On the stagnation of grain growth in nanocrystalline materials". In: *Scripta Materialia* 60.11 (2009), pp. 945–948.

[3] Elizabeth A Holm and Stephen M Foiles. "How grain growth stops: A mechanism for grain-growth stagnation in pure materials". In: *Science* 328.5982 (2010), pp. 1138–1141.

[4] Mathias Bjerre et al. "Rotation-induced grain growth and stagnation in phase-field crystal models". In: *Physical Review E* 88.2 (2013), p. 020401.

[5] KR Elder et al. "Modeling elasticity in crystal growth". In: *Physical review letters* 88.24 (2002), p. 245701.

[6] KR Elder and Martin Grant. "Modeling elastic and plastic deformations in nonequilibrium processing using phase field crystals". In: *Physical Review E* 70.5 (2004), p. 051605.

[7] KR Elder et al. "Phase-field crystal modeling and classical density functional theory of freezing". In: *Physical Review B* 75.6 (2007), p. 064107.

[8] G Dee and JS Langer. "Propagating pattern selection". In: *Physical Review Letters* 50.6 (1983), p. 383.

[9] PK Galenko and KR Elder. "Marginal stability analysis of the phase field crystal model in one spatial dimension". In: *Physical Review B* 83.6 (2011), p. 064113.

[10] John W Cahn and Jean E Taylor. "A unified approach to motion of grain boundaries, relative tangential translation along grain boundaries, and grain rotation". In: *Acta materialia* 52.16 (2004), pp. 4887–4898.

[11] Sven van Teeffelen et al. "Derivation of the phase-field-crystal model for colloidal solidification". In: *Physical Review E* 79.5 (2009), p. 051404.

[12] V Heinonen et al. "Phase-field-crystal models and mechanical equilibrium". In: *arXiv preprint arXiv:1311.7336* (2013).

[13] Pak Yuen Chan, Nigel Goldenfeld, and Jon Dantzig. "Molecular dynamics on diffusive time scales from the phase-field-crystal equation". In: *Physical Review E* 79.3 (2009), p. 035701.

[14] R Backofen and A Voigt. "Solid–liquid interfacial energies and equilibrium shapes of nanocrystals". In: *Journal of Physics: Condensed Matter* 21.46 (2009), p. 464109.

[15] PK Galenko et al. "Unconditionally stable method and numerical solution of the hyperbolic phase-field crystal equation". In: *Physical Review E* 88.1 (2013), p. 013310.

[16] Andrew J Archer et al. "Solidification fronts in supercooled liquids: How rapid fronts can lead to disordered glassy solids". In: *Physical Review E* 86.3 (2012), p. 031603.

[17] William H Press. *Numerical recipes 3rd edition: The art of scientific computing*. Cambridge university press, 2007. Chap. 20.7 Spectral Methods, pp. 1083–1096.

[18] Lloyd N Trefethen. *Spectral methods in MATLAB*. Vol. 10. Siam, 2000.

[19] Kuo-An Wu and Peter W Voorhees. "Phase field crystal simulations of nanocrystalline grain growth in two dimensions". In: *Acta Materialia* 60.1 (2012), pp. 407–419.

[20] ZT Trautt and Y Mishin. "Grain boundary migration and grain rotation studied by molecular dynamics". In: *Acta Materialia* 60.5 (2012), pp. 2407–2424.

[21] G Gottstein and LS Shvindlerman. "Triple junction drag and grain growth in 2D polycrystals". In: *Acta materialia* 50.4 (2002), pp. 703–713.

[22] Shreyas Gokhale et al. "Directional grain growth from anisotropic kinetic roughening of grain boundaries in sheared colloidal crystals". In: *Proceedings of the National Academy of Sciences* 109.50 (2012), pp. 20314–20319.

[23] Jesper Mellenthin, Alain Karma, and Mathis Plapp. "Phase-field crystal study of grain-boundary premelting". In: *Physical Review B* 78.18 (2008), p. 184110.

[24] Gordon Leslie Squires. *Practical physics*. Cambridge university press, 2001.

[25] Morten Hjort-Jensen. "Computational Physics, Lecture Notes Fall 2011".

Chapter 8

Appendix

8.1 The forward Euler scheme

The PFC model can be expressed as this differential equation:

$$\frac{\partial \psi}{\partial t} = \nabla^2 \left[-\epsilon\psi + (1+\nabla^2)^2\psi + \psi^3 \right] \tag{8.1}$$

In order to solve the above differential equation in one dimension, the explicit forward Euler scheme was implemented on the time derivative:

$$\psi_{t+\Delta t,n} = \psi_{t,n} + \Delta t \cdot \nabla^2 \left[-\epsilon\psi + (1+\nabla^2)^2\psi + \psi^3 \right] \tag{8.2}$$

The Laplacian ∇^2 was solved with this explicit scheme in 1D:

$$\frac{\partial^2 \psi}{\partial x^2} = \frac{\psi_{t,x-\Delta x} + \psi_{t,x+\Delta x} - 2\psi_{t,x}}{\Delta x^2} \tag{8.3}$$

This solution was derived from a Taylor expansion. In order to solve the higher order derivatives, this solution was applied several times.

8.2 The spectral method

8.2.1 The spectral method in 1D

The spectral method [17, 18] is more computationally efficient than the explicit Euler method, because it uses a simpler method of calculating the spatial derivatives. The method we have used is based on the Fourier transform, which can transform a time or space dependent signal to a frequency dependent function. The Fourier transform of a function is [18]

$$\hat{u}(k) = \int_{-\infty}^{\infty} e^{-ikx} u(x) dx \tag{8.4}$$

and the inverse Fourier transform is defined as

$$u(x) = \frac{1}{2\pi} \int_{-\infty}^{\infty} e^{ikx} \hat{u}(k) dk \tag{8.5}$$

If ψ is Fourier transformed, the spatial derivative can be found in Fourier space [17]:

$$\psi \longrightarrow \hat{\psi} \tag{8.6}$$

$$\hat{\psi} \longrightarrow ik\hat{\psi} \tag{8.7}$$

$$ik\hat{\psi} \longrightarrow \frac{d}{dx}\psi \tag{8.8}$$

When using the Fourier transform numerically, a discrete Fourier transform has to be used. The discrete Fourier transform can be written like this [18]:

$$\hat{v}(k) = \frac{2\pi}{N} \sum_{j=1}^{N} e^{-ikx(j)} v(j), \qquad k = -\frac{N}{2} + 1, \ \ldots \ , \frac{N}{2} \tag{8.9}$$

and the inverse Fourier transform is defined as

$$v(j) = \frac{1}{2\pi} \sum_{k=-N/2+1}^{N/2} e^{ikx(j)} \hat{v}(k), \qquad j = 1, \ \ldots \ , N \tag{8.10}$$

The parabolic PFC equation in Fourier space looks like this:

$$\frac{d\hat{\psi}}{dt} = -k^2(-\epsilon + (1 - k^2)^2)\hat{\psi} - k^2 \hat{\psi}_{\text{nonlinear}} \tag{8.11}$$

The first part of the above equation is now an ordinary differential equation, which can be solved analytically. The nonlinear term in the Fourier transformed equation is found like this: $\nabla^2 \psi^3 \rightarrow -k^2 \cdot \hat{\psi}_{\text{nonlinear}}$. Splitting the operator, we can solve the linear and the nonlinear part of the equation separately, and add the results afterwards. Using the forward Euler method, the numerical scheme becomes

$$\hat{\psi}(t + \Delta t) = \hat{\psi}(t) e^{L_k \Delta t} - \Delta t \cdot k^2 \hat{\psi}(t)_{\text{nonlinear}} \tag{8.12}$$

where $L_k = -k^2(-\epsilon + (1 - k^2)^2$. The vector k is in this instance

$$k = \left[0, \ \Delta k, \ 2\Delta k, \ \ldots \ , \frac{\pi}{\Delta x}, \ -\frac{\pi}{\Delta x} + \Delta k, \ -\frac{\pi}{\Delta x} + 2\Delta k, \ \ldots \ , -\Delta k\right] \tag{8.13}$$

where Δk is $2\pi/(N\Delta x)$ and N is the length of the vector. The solution in real space is found by doing the inverse Fourier transform on $\hat{\psi}$. The periodic boundary conditions are automatically incorporated, as the Fourier transform assumes that the signal is periodic.

The benefit of using this scheme is that we can use larger time steps, which speeds up the computation. This is especially useful for the more complicated hyperbolic equation.

The numerical scheme used to solve the hyperbolic equation was slightly different. The left hand side of the hyperbolic equation, eq. 2.6, was discretized by using the finite differences method:

$$\tau\frac{\partial^2\psi}{\partial t^2}+\frac{\partial\psi}{\partial t}\longrightarrow\tau\frac{\psi_{t+\Delta t}-2\psi_t+\psi_{t-\Delta t}}{\Delta t^2}+\frac{\psi_{t+\Delta t}-\psi_t}{\Delta t} \tag{8.14}$$

This gave the equation

$$\tau\frac{\hat{\psi}_{t+\Delta t}-2\hat{\psi}_t+\psi_{t-\Delta t}}{\Delta t^2}+\frac{\hat{\psi}_{t+\Delta t}-\hat{\psi}_t}{\Delta t}=L_k\hat{\psi}_t-k^2\hat{\psi}_{t,\text{nonlinear}} \tag{8.15}$$

Sorting the terms gives the following equation:

$$\hat{\psi}_{(t+\Delta t)}=\frac{2\tau+\Delta t}{\tau+\Delta t}\hat{\psi}_t-\frac{\tau}{\tau+\Delta t}\hat{\psi}_{(t-\Delta t)}+\frac{\Delta t^2}{\tau+\Delta t}(L_k\hat{\psi}_t-k^2\hat{\psi}_{t,\text{nonlinear}}) \tag{8.16}$$

In order to calculate the first timestep we assume that $\psi_{-\Delta t}=\psi_{\Delta t}$ [25]. For the first timestep we get the equation

$$\hat{\psi}_{\Delta t}=\hat{\psi}_0+\frac{\Delta t^2}{2\tau+\Delta t}(L_k\hat{\psi}_0-k^2\hat{\psi}_{0,\text{nonlinear}}) \tag{8.17}$$

8.2.2 The spectral method in 2D

In 2D the k-vector becomes two matrices, K_x and K_y.

$$K_x=\begin{pmatrix}0 & \Delta k & 2\Delta k & \cdots & \pi\Delta x & -\pi/\Delta x+\Delta k & \cdots & -\Delta k\\ 0 & \Delta k & 2\Delta k & \cdots & \pi\Delta x & -\pi/\Delta x+\Delta k & \cdots & -\Delta k\\ \vdots & \vdots & \vdots & \ddots & \vdots & \vdots & \ddots & \vdots\\ 0 & \Delta k & 2\Delta k & \cdots & \pi\Delta x & -\pi/\Delta x+\Delta k & \cdots & -\Delta k\end{pmatrix} \tag{8.18}$$

$$K_y=\begin{pmatrix}0 & 0 & \cdots & 0\\ \Delta k & \Delta k & \cdots & \Delta k\\ \vdots & \vdots & \ddots & \vdots\\ -\Delta k & -\Delta k & \cdots & -\Delta k\end{pmatrix} \tag{8.19}$$

where $\Delta k=2\pi/(N\Delta x)$. In all our simulations $\Delta x=\Delta y$. The 1D equations from above look like this in 2D: $k^2=K_x^2+K_y^2$ and L_k becomes

$$L_k=-(K_x^2+K_y^2)\cdot(-\epsilon+(1-(K_x^2+K_y^2))^2) \tag{8.20}$$

With these changes the remaining equations are the same.